



UNIVERSITY OF LEEDS

Interaction of surface acoustic waves and magnetic thin films



Jintao Shuai

School of Physics and Astronomy

University of Leeds

Submitted in accordance with the requirements for the degree of

Doctor of Philosophy

September 2023

To my parents

Intellectual property statement

The candidate confirms that the work submitted is his own, except where work which has formed part of jointly authored publications has been included. The contribution of the candidate and the other authors to this work has been explicitly indicated below. The candidate confirms that appropriate credit has been given within the thesis where reference has been made to the work of others.

This copy has been supplied on the understanding that it is copyright material and that no quotation from the thesis may be published without proper acknowledgement.

The right of Jintao Shuai to be identified as Author of this work has been asserted by him in accordance with the Copyright, Designs and Patents Act 1988.

© 2023 The University of Leeds and Jintao Shuai.

This thesis incorporates work from the jointly authored publications:

Chapter 4

Jintao Shuai, Mannan Ali, Luis Lopez-Diaz, John E. Cunningham, and Thomas A. Moore. Local anisotropy control of Pt/Co/Ir thin film with perpendicular magnetic anisotropy by surface acoustic waves. *Applied Physics Letters*, 120, 252402 (2022).

Contributions by candidate: Design of experiments. Execution of experiments. Design of numerical simulations. Execution of numerical simulations. Data analysis. Manuscript preparation.

Contributions by Others: Mannan Ali: Methodology insights. Manuscript editing. Luis Lopez-Diaz: Design of numerical simulations. Computational resources. Results discussion. Manuscript editing. John E. Cunningham and Thomas A. Moore: Supervision. Design of experiments. Methodology insights. Results discussion. Manuscript editing.

Chapter 5

Jintao Shuai, Robbie G. Hunt, Thomas A. Moore, and John E. Cunningham. Separation of heating and magnetoelastic coupling effects in surface-acoustic-wave-enhanced creep of

Intellectual property statement

magnetic domain walls. *Physical Review Applied*, 20, 014002 (2023).

Contributions by candidate: Design of experiments. Execution of experiments. Data analysis. Manuscript preparation.

Contributions by Others: Robbie G. Hunt: Methodology insights. Manuscript editing. Thomas A. Moore and John E. Cunningham: Supervision. Design of experiments. Methodology insights. Results discussion. Manuscript editing.

Chapter 6

Jintao Shuai, Luis Lopez-Diaz, John E. Cunningham, and Thomas A. Moore. Surface acoustic wave effect on magnetic domain wall dynamics, *Physical Review B*, 108, 104420 (2023).

Contributions by candidate: Design of numerical simulations. Execution of numerical simulations. Data analysis. Manuscript preparation.

Contributions by Others: Luis Lopez-Diaz: Design of numerical simulations. Computational resources. Results discussion. Manuscript editing. Thomas A. Moore and John E. Cunningham: Supervision. Design of numerical simulations. Methodology insights. Results discussion. Manuscript editing.

Chapter 7

Jintao Shuai, Luis Lopez-Diaz, John E. Cunningham, and Thomas A. Moore. Precise transport of skyrmions by surface acoustic waves. *arXiv:2305.16006* (2023).

Contributions by candidate: Design of numerical simulations. Execution of numerical simulations. Data analysis. Manuscript preparation.

Contributions by Others: Luis Lopez-Diaz: Design of numerical simulations. Computational resources. Results discussion. Manuscript editing. John E. Cunningham and Thomas A. Moore: Supervision. Design of numerical simulations. Methodology insights. Results discussion. Manuscript editing.

Acknowledgements

First and foremost, my heartfelt gratitude goes to my supervisors, Dr Thomas Moore and Prof John Cunningham. Their consistent guidance, coupled with their deep expertise, played a pivotal role in shaping my research. Their constructive feedback, encouragement, and patience have been instrumental, ensuring I navigated challenges effectively. I truly valued our in-depth discussions and the broad spectrum of knowledge they imparted during our time together.

I am deeply thankful to Prof Luis Lopez-Diaz, Prof Rudolf Schäfer, Dr Ivan Soldatov, Prof Bert Koopmans, Dr Reinoud Lavrijen, Mouad, Rocío, Felipe, Pingzhi, and Adrien for their support during my secondments in Salamanca, Dresden, and Eindhoven. Dr Liza Herrera Diez, Clare Desplats and PIs from MagnEFi deserve special mention for their incredible guidance, management of the project, and for uniting everyone. My journey was further enriched by my fellow ESRs from MagnEFi: Golam, Rohit, Adithya, Giovanni, Mandy, Gyan, Cristina, Sreeveni, Beatrice, Adriano, and Subhajit. My deepest appreciation goes to the respected academics in our group. Their insights and encouragement were invaluable throughout my research journey. Further, I want to express my heartfelt thanks to Mannan, Philippa, Matt, Nathan, and Craig for their invaluable training and support. I extremely appreciate Mark and Li for their foundational cleanroom training and technical assistance, with additional thanks to Li for his assistance for the cleanroom fabrication during the Covid lockdown.

Cheers to the “Lunch Club” – Chris, Dan, and Robbie. Your company transformed our daily meals into delightful gatherings; lunches just weren not the same without you. My thanks also go out to Ahmet, Robert, Emily, Lin, Sean, Ioannis, Callum, Thomas, Servet, Hari, and Eloi for the shared moments and memories. My years at Royal Park Flat were made memorable by friends such as Ayhan, Ayo, Nidhin, Srinath, Smruthi, Chrissy, Drea, Manmeet, Prateek, Manan, Xiao, Harry, David, Oscar, and Dylan.

A special acknowledgement for Rutvij – thank you for being an incredible pillar of support. My time in York was made unforgettable thanks to Ding, Vincenzo, Shashaank,

Acknowledgements

Alistair, Cordelia, Jenny, Beth, Peiyun, Jack, Jade, Hamid, Ambroise, Simen, Ayan, Shefali, Nekhel, and Anjali. To Weng Wei, Chen Wen, Chenyang, Zhou Jia, Beibei, and Ruru – your presence was a comforting reminder of home in a foreign land.

Above all, my deepest appreciation goes out to my parents and family. Their boundless love, unwavering support, and sacrifices have been the driving force behind my achievements. This accomplishment is as much theirs as it is mine.

I am grateful to the European Union's Horizon 2020 research and innovation programme for their support through the Marie Skłodowska-Curie grant agreement No. 860060 "[Magnetism and the effect of Electric Field](#)" (MagnEFi). This funding not only facilitated my research but also elevated my entire PhD journey to a unique and enriching experience.

Finally, I would like to thank Dr Satoshi Sasaki and Dr Tom Hayward for their comprehensive examination of this thesis.

Abstract

Surface acoustic waves (SAWs) have emerged as innovative and energy-efficient means to manipulate domain walls (DWs) and skyrmions in thin films with perpendicular magnetic anisotropy (PMA) owing to the magnetoelastic coupling effect. This thesis focuses on the complex interplay between SAWs and magnetic thin films with PMA through both experimental and micromagnetic studies. The effects of the standing SAWs on the magnetisation dynamics in a Ta(5.0 nm)/Pt(2.5 nm)/Co(1.1 nm)/Ir(1.5 nm)/Ta(5.0 nm) thin film with PMA were first investigated. SAWs with frequency of 93.35 MHz significantly reduced the coercivity of the thin film by 21% and enhanced the magnetisation reversal speed by 11-fold. Standing SAWs introduce a dynamic energy landscape with a unique spatial distribution, forming striped domain patterns in the thin film. The use of radio-frequency signals for generating SAWs inevitably causes a heating effect in the device. This heating effect was carefully examined *in situ* in a SAW device featuring a Ta(5.0 nm)/Pt(2.5 nm)/Co(0.9 nm)/Ta(5.0 nm) thin film with PMA using an on-chip platinum thermometer. It was shown that the temperature increased by 10 K in the presence of SAWs at centre frequency of 48 MHz. The DW velocity was significantly enhanced in the presence of the standing SAWs by a factor of 4 compared to that with temperature change alone owing to the magnetoelastic coupling effect. To understand the SAW-enhanced DW motion, comprehensive micromagnetic simulations were performed on thin films in the presence of travelling SAWs with frequencies from 50 to 200 MHz. The findings highlighted that SAW-induced vertical Bloch lines within DWs can simultaneously boost DW depinning and dissipate energy at the DW via spin rotation. The SAW-induced strain gradient can be exploited to control skyrmion motion in a current-free manner. Micromagnetic simulations revealed that the use of orthogonal SAWs, combining horizontal travelling and vertical standing waves, offered a promising approach to direct skyrmion motion along desired trajectories, avoiding undesirable Hall-like motion. In conclusion, this thesis offers a significant contribution to the understanding of how SAWs influence magnetisation dynamics.

Abstract

CONTENTS

1	Introduction	1
1.1	Background	2
1.2	Magnetisation dynamics control	2
1.2.1	By magnetic field	2
1.2.2	Via electric current	3
1.2.3	With static strain	6
1.2.4	Through dynamic strain	8
1.3	Thesis overview	13
2	Theoretical background	17
2.1	Introduction	18
2.2	Magnetisation dynamics	18
2.3	Free energy and effective field	21
2.3.1	Exchange	21
2.3.2	Magnetic Anisotropy	23
2.3.3	Interfacial Dzyaloshinskii–Moriya interaction	26
2.3.4	Zeeman energy	27
2.4	Magnetisation reversal	28
2.4.1	Domain and domain wall	29
2.4.2	Domain wall motion	31

CONTENTS

2.4.3	Skyrmions	33
2.5	Surface acoustic waves	34
2.5.1	Piezoelectric effect	34
2.5.2	SAW excitation and propagation	35
2.6	Summary	40
3	Methods	41
3.1	Introduction	42
3.2	Magnetic thin film fabrication	43
3.2.1	Substrate and cleaning process	43
3.2.2	Thin film deposition	44
3.3	Magnetic thin film characterisation	47
3.3.1	Deposition rate calibration	47
3.3.2	Hysteresis loop and domain image	48
3.4	Surface acoustic wave device	51
3.4.1	Device design	51
3.4.2	Device fabrication	53
3.4.3	Device characterisation	59
3.5	Micromagnetic simulations	61
3.6	Summary	64
4	Local magnetic anisotropy control	67
4.1	Introduction	68
4.2	Experimental details	69
4.2.1	Magnetic thin film and SAW device	69
4.2.2	SAW circuit and S-parameters	69
4.2.3	Determination of magnetisation reversal speed	71
4.2.4	Computational details	74

4.3	Results and discussion	75
4.3.1	Reduced coercivity	75
4.3.2	Enhanced magnetisation reversal speed	77
4.3.3	Standing SAW-induced stripe domain patterns	78
4.3.4	Magnetisation dynamics under standing SAWs	81
4.4	Summary	83
5	Separation of heating and strain effects	85
5.1	Introduction	86
5.2	Methods	87
5.2.1	Magnetic thin film and SAW device	87
5.2.2	SAW circuit and S-parameters	89
5.2.3	Determination of temperature change	91
5.2.4	Determination of domain wall velocity	91
5.3	Results and discussion	94
5.3.1	Temperature change in device	94
5.3.2	Heating dynamics model	96
5.3.3	Source of heating	99
5.3.4	Heating and strain effects on domain wall velocity	102
5.4	Summary	106
6	SAW effect on domain wall dynamics	109
6.1	Introduction	110
6.2	Model and computational details	111
6.2.1	Proposed device and simulation configuration	111
6.2.2	Incorporating disorder and SAW in simulations	113
6.2.3	Determination of domain wall velocity	114
6.3	Results and discussion	114

CONTENTS

6.3.1	Enhanced domain wall velocity	114
6.3.2	Domain wall depinning	118
6.3.3	Formation of vertical Bloch lines	120
6.4	Summary	128
7	SAW effect on skyrmion dynamics	129
7.1	Introduction	130
7.2	Model and computational details	131
7.3	Results and discussions	133
7.3.1	Impact of standing SAWs on skyrmion motion	133
7.3.2	Impact of travelling SAWs on skyrmion motion	135
7.3.3	Impact of orthogonal SAWs on skyrmion motion	135
7.3.4	Multichannel skyrmion racetrack	138
7.4	Summary	140
8	Conclusions and outlook	143
8.1	Conclusions	144
8.2	Outlook	146
	References	170

LIST OF FIGURES

1.1	Diagram of domain wall motion induced by spin–transfer torque. . . .	4
1.2	Diagram of domain wall motion induced by spin–orbit torque.	5
1.3	Methods of introducing static strain into magnetic thin films.	7
1.4	Applications of surface acoustic wave-controlled magnetism.	9
1.5	Thesis overview.	14
2.1	Magnetic moment precesses around the effective field.	19
2.2	Magnetic moments at the nearest neighbours i and j	22
2.3	Schematic diagram illustrating the interfacial Dzyaloshinskii–Moriya interaction at the interface between a magnetic film and a heavy metal.	27
2.4	Typical hysteresis loops of a ferromagnetic material and a thin film with perpendicular magnetic anisotropy.	29
2.5	Domain and domain wall motion with an applied out-of-plane field in a thin film with perpendicular magnetic anisotropy.	30
2.6	Diagram of the domain wall structures.	30
2.7	Domain wall velocity regimes in relation to driving force.	31
2.8	Domain wall velocity as a function of the magnetic field in thin films with disorder.	33
2.9	Magnetic texture of skyrmions.	34

LIST OF FIGURES

2.10	Schematic of a piezoelectric unit cell and a piezoelectric unit cell with force or electric field applied.	35
2.11	Excitation of surface acoustic waves.	37
2.12	Interdigitated transducer response as a function of the detuning parameter.	39
3.1	Schematic representation of the 128° Y-cut lithium niobate.	43
3.2	Diagram of the direct current magnetron sputtering.	45
3.3	Diagram of the distribution of the magnetic and electric fields in the direct current magnetron sputtering, alongside the particle motion influenced by these fields.	46
3.4	Diagram of X-ray reflectometry principle and X-ray reflectometry patterns.	47
3.5	Diagram of the wide-field Kerr microscope.	50
3.6	Example of the interdigitated transducer geometry used to generate surface acoustic waves.	52
3.7	Layout of a surface acoustic wave device.	53
3.8	Illustration of the photolithography process.	55
3.9	Diagram of the thermal evaporator.	58
3.10	Layout and schematic diagram of the co-planar waveguide used in this thesis.	60
3.11	Schematic representation of the scattering parameters in a two-port system.	61
3.12	Schematic of the radio-frequency circuit used to characterise scattering parameters.	62
3.13	Example of standing and travelling surface acoustic waves implemented using Mumax3.	64

LIST OF FIGURES

4.1	Thin film structure and schematic of experimental arrangement. . . .	70
4.2	Scattering parameters of the interdigitated transducers.	71
4.3	Schematic of the radio-frequency circuit for generating standing surface acoustic waves.	72
4.4	Determining magnetisation reversal speed using Kerr microscopy. . .	73
4.5	Configuration of the micromagnetic simulations.	74
4.6	Hysteresis loops of the Ta/Pt/Co/Ir/Ta thin film.	76
4.7	Coercivity of the Ta/Pt/Co/Ir/Ta thin film.	76
4.8	Magnetisation reversal speed of the Ta/Pt/Co/Ir/Ta thin film. . . .	78
4.9	Domain patterns in the Ta/Pt/Co/Ir/Ta thin film.	79
4.10	Analysis of the strip domain pattern in the Ta/Pt/Co/Ir/Ta thin film upon application of standing surface acoustic waves.	80
4.11	Simulation of magnetisation reversal process.	82
5.1	Schematic diagram of the surface acoustic wave device, electrical transport measurement, and thin film structures.	88
5.2	Schematic diagram of radio-frequency circuits used to generate standing and travelling surface acoustic waves.	90
5.3	Pt resistance against temperature and against time at room temperature.	92
5.4	Determination of the domain wall velocity in the Ta/Pt/Co/Ta thin film.	93
5.5	Temperature changes of the Pt within the surface acoustic wave beam path.	95
5.6	Temperature progression sequence: from radio-frequency power-off state, through power-on state where temperature stabilises at equilibrium, back to power-off.	97
5.7	Analysis on the origin of the heating.	101

LIST OF FIGURES

5.8	Domain wall velocity in the Ta/Pt/Co/Ta thin film as a function of applied magnetic field.	103
5.9	Domain wall profile in the Ta/Pt/Co/Ta thin film under different experimental conditions imaged using a Kerr microscope	105
6.1	Configuration for domain wall dynamics simulations.	112
6.2	Domain wall velocity as a function of the applied external magnetic field without surface acoustic waves.	116
6.3	Domain wall velocity as a function of the applied external magnetic field with and without surface acoustic waves.	117
6.4	Time evolution of domain wall motion in thin films with anisotropy disorder.	119
6.5	Snapshots of the magnetisation configuration without surface acoustic waves and in the presence of surface acoustic waves.	121
6.6	Domain wall motion and vertical Bloch lines plotted against simulation time, and snapshots of the magnetisation configuration both without surface acoustic waves and in the presence of surface acoustic waves at 0 and 300 K.	124
6.7	Diagram of spin dynamics under different conditions.	126
7.1	Diagram of the proposed device and its initial magnetisation, strain spatial profile of the surface acoustic wave.	132
7.2	Skyrmion motion under the standing surface acoustic waves.	134
7.3	Skyrmion motion under the travelling surface acoustic waves.	136
7.4	Skyrmion motion under the orthogonal surface acoustic waves.	137
7.5	Illustration of forces acting on a skyrmion induced by orthogonal surface acoustic waves, and skyrmion motion under orthogonal surface acoustic waves with different properties.	139

LIST OF FIGURES

7.6 Skyrmion trajectories in a multichannel racetrack with orthogonal surface acoustic waves.	140
---	-----

LIST OF FIGURES

LIST OF TABLES

- 3.1 Deposition current and deposition rate of materials used in this thesis. 48
- 5.1 Device temperature changes in the presence of surface acoustic waves. 96

LIST OF TABLES

LIST OF ABBREVIATIONS

- CMOS** complementary metal-oxide-semiconductor. 11
- CPW** co-planar waveguide. 42, 59–61
- dc** direct current. 7, 89
- dcMS** direct current magnetron sputtering. 42, 44–46, 54, 55, 57, 64, 69, 87, 88
- DMD** digital micro-mirror device. 56
- DMI** Dzyaloshinskii–Moriya interaction. 5, 7, 18, 20, 26, 27, 34, 40, 86, 130, 133
- DW** domain wall. 2–8, 10, 13, 15, 18, 29–33, 40, 68, 71, 75, 77, 81, 86, 89, 91, 93, 94, 101–106, 110–120, 122–128, 144–146
- FMR** ferromagnetic resonance. 6, 9, 10, 42
- IDT** interdigitated transducer. 8, 11, 36–40, 42, 51–55, 57–62, 64, 65, 69–71, 87–89, 94–96, 99–101, 111, 112, 131, 132, 146
- LED** light-emitting diode. 48
- LLG** Landau–Lifshitz–Gilbert. 20, 61, 74, 111, 133
- MLA** maskless aligner. 54, 56, 57, 69

LIST OF ABBREVIATIONS

MOKE magneto-optic Kerr effect. 48, 49

PCB prototype circuit board. 42, 59

PMA perpendicular magnetic anisotropy. 2, 3, 6–8, 12, 13, 18, 25, 28–30, 40, 42, 48, 68, 69, 75, 83, 86, 87, 111, 112, 130–132, 144–146

rf radio-frequency. 8, 9, 13, 15, 36, 37, 59, 61, 62, 70, 72, 75–78, 86, 89, 90, 94–97, 99–104, 106, 107, 131, 144–146

S-parameter scattering parameter. 42, 60–62, 65, 69, 71, 72, 88–90, 96, 102

SAW surface acoustic wave. 2, 8–15, 18, 35–38, 40, 42, 43, 51–53, 59–61, 63–65, 68–75, 77–83, 86–97, 99–107, 110–128, 130–141, 144–147

SMA SubMiniature version A. 59–61, 100

SOC spin–orbit coupling. 4, 5, 25, 33, 130

SOT spin–orbit torque. 4–6, 10, 130

STT spin–transfer torque. 3–6, 130

UV ultraviolet. 54, 55

VBL vertical Bloch line. 32, 110, 121–127

VNA vector network analyser. 42, 60, 61, 65, 69–72, 90

XRR X-ray reflectometry. 42, 47, 48, 64

LIST OF PUBLICATIONS

Journal Publications

- **J. Shuai**, L. Lopez-Diaz, J. E. Cunningham, T. A. Moore, Influence of surface acoustic wave frequency on domain wall dynamics, *Physical Review B*, 108, 104420 (2023).
- **J. Shuai**, R. G. Hunt, T. A. Moore, J. E. Cunningham, Separation of heating and magneto-elastic coupling effects in surface acoustic wave-enhanced magnetic domain wall creep motion, *Physical Review Applied*, 20, 014002 (2023).
- **J. Shuai**, M. Ali, L. Lopez-Diaz, J. E. Cunningham, T. A. Moore, Local anisotropy control of Pt/Co/Ir thin film with perpendicular magnetic anisotropy by surface acoustic waves, *Applied Physics Letters*, 120, 252402 (2022).
- **J. Shuai**, L. Lopez-Diaz, J. E. Cunningham, T. A. Moore, Precise transport of skyrmions by surface acoustic waves, *arXiv:2305.16006* (2023).

Conference presentations

Note: “●” denotes oral presentation and “▪” denotes poster presentation.

- Surface acoustic wave effect on magnetic domain wall dynamics. Spin Electronics and Nanomagnetism Colloquium 2023, Nancy, France, August 2023.
- Surface acoustic wave effect on magnetisation dynamics in thin films. Royce Student Summit 2023, Leeds, United Kingdom, July 2023.
- Interaction of surface acoustic waves and magnetic thin films. IOP Condensed Matter and Quantum Materials, Birmingham, United Kingdom, June 2023.
- Precise transport of skyrmions by surface acoustic waves. IEEE Intermag, Sendai, Japan, May 2023.

LIST OF PUBLICATIONS

- Separation of heating and magneto-elastic coupling effects in surface acoustic wave-enhanced magnetic domain wall creep motion. IOP Magnetism, Manchester, United Kingdom, April 2023.
- Precise transport of skyrmions by surface acoustic waves. IOP Magnetism, Manchester, United Kingdom, April 2023.
- Surface acoustic waves effect on domain wall motion. IEEE MMM 2022, online, November 2022.
- Precise trajectory control of skyrmion motion by surface acoustic waves. IEEE MMM 2022, online, November 2022.
- Enhanced domain wall motion by surface acoustic waves. IEEE AtC-AtG 2022, online, August 2022.
- Interaction of surface acoustic waves and magnetic thin films. Home workshop, Universidad de Salamanca, Salamanca, Spain, July 2022.
- Interaction of surface acoustic waves and magnetic thin films. Joint meeting of the BeMAGIC and MagnEFi ITN networks, Aalto University, Espoo, Finland, June 2022.
- Local anisotropy control of Pt/Co/Ir thin films with perpendicular magnetic anisotropy by surface acoustic waves. Bragg PhD Colloquium 2022, University of Leeds, Leeds, United Kingdom, June 2022.
- Local anisotropy control of Pt/Co/Ir thin films with perpendicular magnetic anisotropy by surface acoustic waves. IOP Magnetism 2022, University of York, York, United Kingdom, March 2022.

LIST OF PUBLICATIONS

- Coercivity control of thin films with perpendicular magnetic anisotropy by surface acoustic waves. Bragg Exchange Conference, University of Leeds, Leeds, United Kingdom, January 2022.
- Coercivity control of thin films with perpendicular magnetic anisotropy by surface acoustic waves. 2022 Joint MMM-INTERMAG, online, January 2022.

LIST OF PUBLICATIONS

CHAPTER 1

Introduction

1.1 Background

Spintronic devices have drawn wide attention for their significant potential in the next generation of data storage and logic processing applications [1–3]. A promising strategy is to encode information using magnetic spin structures, such as domain walls (DWs) and skyrmions [4, 5]. Thin films with perpendicular magnetic anisotropy (PMA) are useful in this context because the PMA guarantees stability of the stored information as well as a high storage density [6]. One of the challenges in thin magnetic films with PMA is to move DWs and skyrmions efficiently. Surface acoustic waves (SAWs), which are elastic waves travelling on the surface of piezoelectric materials, offer a potential solution to this. SAWs can introduce dynamic strain waves into magnetic thin films [7]. Through the magnetoelastic coupling effect, these dynamic strain waves generate a dynamic energy landscape, thereby triggering magnetisation precession [8–10], facilitating magnetisation switching [11, 12], and enhancing the DW and skyrmion motion [13–19].

1.2 Magnetisation dynamics control

1.2.1 By magnetic field

Magnetic DWs are transitional regions separating adjacent magnetic domains with opposing magnetisation directions [20]. When an external magnetic field is applied to a magnetic material, its intrinsic magnetic moments tend to align with this field, in order to reduce the overall energy of the system. Consequently, this magnetic field can favour the expansion of these domains, which in turn drives the DW motion [21]. At low fields, domains expand due to a slightly distorted wall structure associated with internal torque, which leads to creep regime. Above a critical field, which is called the Walker breakdown, the DWs motion decreases with the field. When the magnetic field

1.2 Magnetisation dynamics control

is sufficient higher than the Walker breakdown, DW enters the flow regime in which the magnetisation within the DW precesses. Notably, Metaxas *et al.* studied the DW velocity in Pt/Co/Pt thin films with PMA over a large range of applied magnetic fields showing a complete velocity-field characteristics with motion regimes predicted from general theories for driven elastic interfaces in weakly disordered media [22].

Limitations

While the motion of DWs driven by magnetic fields has been extensively studied and is readily attainable in laboratory settings, challenges arise when aiming for high-speed DW motion. Achieving such rapid motion usually necessitates the application of a substantial external magnetic field, thereby limiting practical device applications [23]. Furthermore, achieving local control over individual domains through a magnetic field poses challenges, since it inevitably affects neighbouring domains.

1.2.2 Via electric current

Spin-transfer torque

An electric current can lead to DW motion in thin films with PMA via spin-transfer torque (STT) [24, 25]. STT describes the transfer of angular momentum from spin-polarised electrons to a magnetic material, subsequently exerting a torque on magnetic moments of the magnetic material [26]. Figure 1.1 shows the schematic diagram of STT-induced DW motion. When conduction electrons (injected from left of the magnetic layer in Figure 1.1), whose spins are not aligned with the magnetisation of the ferromagnetic layer, flow through a magnetic layer, the local magnetisation attempts to align these electron spins by exerting a torque on them (see Figure 1.1b). Owing to the conservation of spin angular momentum, these conduction electrons also exert an equal and opposite torque on the local magnetisation (see Figure 1.1c).

1 Introduction

This reciprocal action can be used to switch magnetisation or drive DW motion (as shown in Figure 1.1d) [27–29].

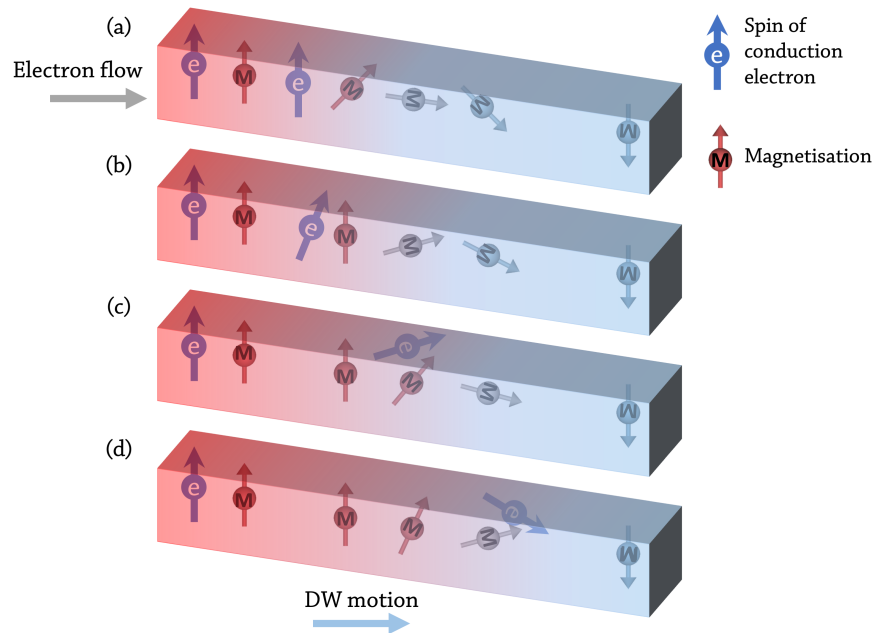


Figure 1.1: Diagram of STT-induced DW motion. (a) Conduction electrons are injected from one side of the thin film containing a DW. The local magnetisation attempts to align the spins of these conduction electrons. (b–c) Aligned spins exert an equal and opposite torque on the local magnetisation, leading to its rotation. (d) This reciprocal action can switch the magnetisation or induce the motion of the DW. The figure has been reproduced from [27].

Spin–orbital torque

Electric currents can induce spin–orbit torque (SOT), a phenomenon also capable of driving DW motion. This torque arises from the pronounced spin–orbit coupling (SOC). As shown in Figure 1.2, in heavy metal/ferromagnetic heterostructures, the

1.2 Magnetisation dynamics control

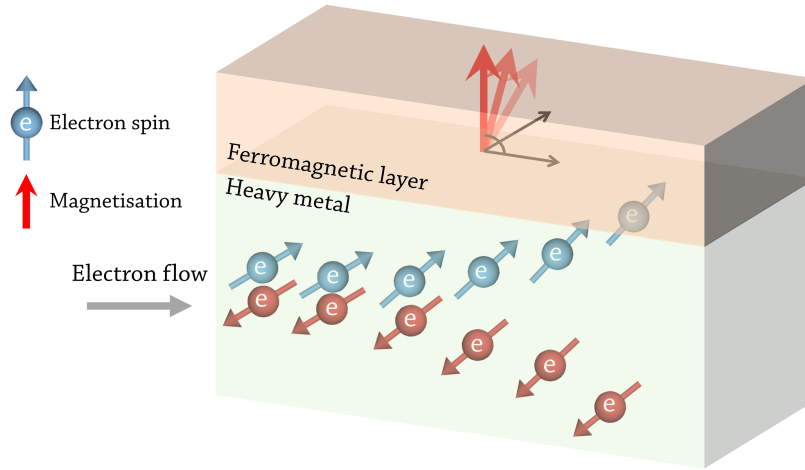


Figure 1.2: Diagram of SOT-induced DW motion. In heavy metal/ferromagnetic heterostructures, the pronounced SOC within the heavy metal converts the charge current into a spin current when an electric current passes through. This spin current is injected into the adjacent ferromagnetic layer, exerting a torque on the magnetisation. This torque results in the magnetisation switching and DW motion. The figure has been reproduced from [38].

pronounced SOC within the heavy metal converts the charge current into a spin current when an electric current passes through. Subsequently, this spin current is injected into the adjacent ferromagnetic layer, exerting a torque on the magnetisation. The presence of this torque induces the rotation of magnetisation. Depending on the polarity of the interfacial Dzyaloshinskii–Moriya interaction (DMI) (arises between the heavy metal and ferromagnetic layer) strength, the motion of the DW is either parallel or anti-parallel to the direction of electron flow (indicated by the grey arrow in Figure 1.2) [30]. SOT can facilitate magnetisation switching [31–33] and prompt rapid DW motion within these heavy metal/ferromagnet systems [34–37].

SOT-driven DW motion is more energy-efficient than that driven by STT [39]. STT achieves charge-to-spin conversion through spin filtering in a ferromagnetic layer, cap-

1 Introduction

ping efficiency at one. In contrast, SOT uses multiple spin-orbit scatterings in a heavy metal layer, allowing for greater spin angular momentum transfer from each electron, with additional contributions from the atomic lattice of the heavy metal. Therefore, there is no fundamental limit to the charge-to-spin conversion efficiency [38].

Limitations

Material with strong PMA have a high energy barrier for reorientation of the magnetisation. Therefore, a large current is required to reverse the magnetisation or to move DWs in order to write or transfer data for both STT and SOT. This high current can lead to energy wastage and Joule heating, imposing limitations on the packing density of practical devices [40–42]. For example, Miron *et al.* demonstrated DW motion reaching velocities of approximately 400 m/s in a Pt/Co/AlO_x nano-wire when a current with a density of around 3.2×10^{12} A/m² was applied [40]. Therefore, there is much interest in manipulating spin structures without external magnetic field or electric current, for example, using strain.

1.2.3 With static strain

Owing to the magnetoelastic coupling effect, strain also serves as a method of manipulating to control thin film magnetism. Both theoretical insights and experimental findings underscore that strain-driven DW motion is more energy-efficient than that driven by electric current [39, 43]. Various approaches can introduce static strain into magnetic thin films. One approach is by depositing the magnetic thin films onto a piezoelectric substrate or onto a piezoelectric thin film, and applying of voltage to the piezoelectric substrate or film facilitates strain generation (as shown in Figure 1.3a and b) [44–47]. Another approach is mechanical bending, such as three-point bending as shown in Figure 1.3c [48, 49].

Strain-induced modifications in magnetisation, magnetic anisotropy, and ferromag-

1.2 Magnetisation dynamics control

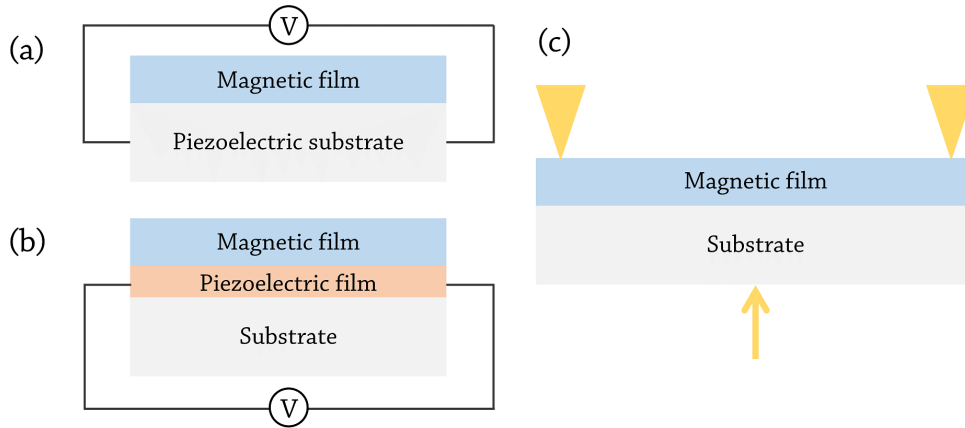


Figure 1.3: Methods of introducing static strain into magnetic thin films: (a) Deposition of thin films onto a piezoelectric substrate followed by voltage application to the substrate. (b) Deposition of thin films onto a piezoelectric film and subsequent voltage application to the piezoelectric layer. (c) Application of mechanical strain via bending.

netic resonance (FMR) have been the focus of a wide range of studies spanning various magnetic systems [44, 50–53]. To illustrate, Shepley *et al.* modified Pt/Co/Pt thin films with PMA by applying static strain using direct current (dc) voltage applied to a piezoelectric transducer. The static strain reduced the coercivity, and increased the DW creep velocity by up to 100% [53]. De Ranieri *et al.* utilised a piezoelectric stressor to induce a 5% reduction in anisotropy in a perpendicularly magnetised GaMnAsP/GaAs ferromagnetic semiconductor, yielding a 500% fluctuation in DW mobility [54]. Gopman *et al.* achieved over a 30% reduction in the coercivity of Co/Ni multilayers by inducing a 0.1% expansion in $\text{Pb}(\text{Zr}_{0.52}\text{Ti}_{0.48})\text{O}_3$ [55].

Skyrmions are chiral magnetic spin structures, which can be found in thin films with PMA that lack spatial inversion symmetry. Skyrmions can be stabilised by a competition between PMA and the DMI. Thus, the modification of PMA can create

1 Introduction

or annihilate skyrmions. For example, Ba *et al.* demonstrated skyrmion creation, deformation and annihilation by modifying PMA via strain [44]. Feng *et al.* modified the anisotropy in Pt/Co/Ta multilayers to manipulate domain patterns [56]. By utilising the shape memory effect of a TiNiNb substrate, they successfully achieved strain-induced, field-free skyrmion nucleation and annihilation.

Significant advancements have been achieved in understanding the magnetoelastic coupling mechanism in the case of static strain-controlled magnetism. However, dynamic strain-controlled magnetism remains intricate and comparatively understudied.

1.2.4 Through dynamic strain

SAWs are dynamic strain waves that travel along the surface of piezoelectric materials and are typically generated through the application of radio-frequency (rf) signals to interdigitated transducers (IDTs) that convert these signals to mechanical waves on a piezoelectric surface. Although the application of this technology is extensive in areas that include wireless communications [57], microfluidics [58], sensing [59–61] and television [62], the utilisation of SAWs to introduce dynamic strain into magnetic thin films and thus to manipulate magnetism remains a relatively new and under-explored field [7]. SAWs demonstrate promise in efficiently controlling magnetism, offering a broad spectrum of applications. These encompass magnetisation dynamics, as well as the manipulation of DWs and skyrmions (as shown in Figure 1.4). For example, Davis *et al.* showcased SAW-induced magnetisation dynamics in 10-nm Co bars. Their findings aligned with the magnetoelastic free energy introduced by strain [63]. Their research provided a proof-of-concept that magnetisation rotation triggered by dynamic strain from SAWs can substantially alter the magnetisation direction. Li *et al.* presented experimental evidence for SAW-assisted magnetic recording (as shown in Figure 1.4 “Switching” section). They utilised standing and focused SAWs to reduce the coercivity in specific regions of 57-nm FeGa thin films [12, 64].

1.2 Magnetisation dynamics control

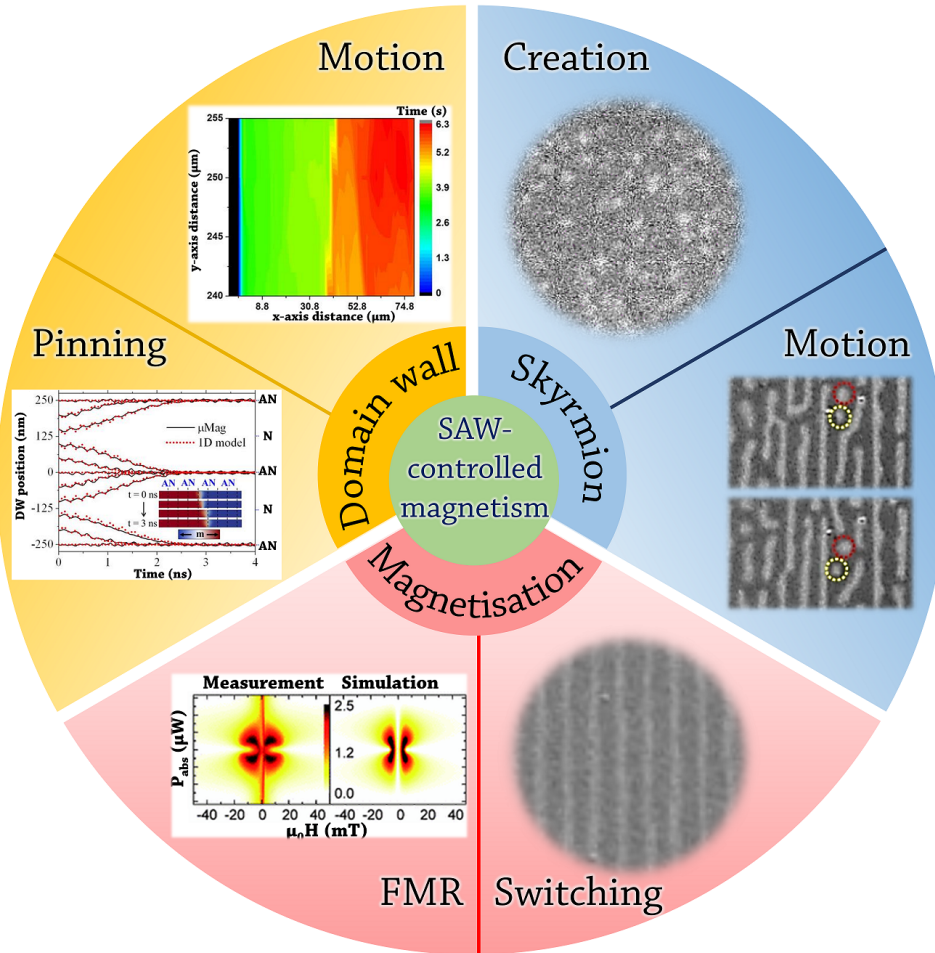


Figure 1.4: Applications of SAW-controlled magnetism. Figures have been reproduced from [13, 14, 64–67].

The periodic strain in both time and space introduced by SAWs can change the anisotropy, which in turn exerts a torque on the magnetisation, triggering FMR. For example, Weiler and Dreher with their colleagues demonstrated both experimentally and numerically that FMR can be purely driven by SAWs without an external rf magnetic field being applied to a nickel thin film (see Figure 1.4 “FMR” section) [67, 68]. Thevenard *et al.* reported numerical prediction and experimental observation of

1 Introduction

SAW-driven FMR in (Ga,Mn)(As,P) epilayers between a temperature range of 5 to 85 K [8, 9, 69]. They also observed a strong coercivity reduction in these thin films [70].

SAW-induced anisotropy changes also contribute to DW motion [15]. For instance, Dean *et al.* presented theoretical evidence that standing SAWs can solely drive DW motion and create pinning sites remotely due to the SAW-induced strain gradient (as shown in Figure 1.4 “Pinning” section). They demonstrated that, by adjusting the SAW frequency, multiple DWs can be synchronised and moved simultaneously [13]. Edrington *et al.* conducted experimental investigations showing that standing SAWs effectively drive DW motion from the creep regime to the flow regime in Co/Pt multilayers (see Figure 1.4 “Domain wall motion” section) [14]. Adhikari *et al.* explored the impact of SAWs on enhancing DW motion within the creep regime by the SAW-induced effective field and increasing the likelihood of DW depinning [71, 72]. Cao *et al.* utilised SAWs to assist SOT magnetisation switching in a Pt/Co/Ta thin films resulting in a reduced critical current density and a higher DW velocity [17].

Owing to the magnetoelastic coupling effect, SAWs can also be used to create or annihilate skyrmions. Yokouchi *et al.* experimentally observed the creation of skyrmions by SAWs in a Pt/Co/Ir thin film owing to the inhomogeneous effective torque arising from both SAWs and thermal fluctuations via magnetoelastic coupling (as shown in Figure 1.4 “Skyrmion creation” section) [65]. However, due to the high pinning energy of the thin film used in their study, SAWs could not move skyrmions. Nepal *et al.* theoretically studied the dynamical pinning of skyrmion bubbles at the anti-nodes of standing SAWs in a FePt nano-wire, revealing the mechanism of the SAW-driven skyrmion motion [19]. Chen *et al.* experimentally presented the ordered generation of magnetic skyrmions [66]. With the application of both electric current and SAWs, they demonstrate the skyrmions motion with negligible skyrmion Hall-like motion (as shown in Figure 1.4 “Skyrmion motion” section). Using a similar concept, Chen *et al.* theoretically demonstrated the suppression of skyrmion Hall-like motion

1.2 Magnetisation dynamics control

via standing SAWs [73]. Using the energy potential created by two standing SAWs, Miyazaki *et al.* theoretically demonstrated the precise trapping of skyrmions. They showed the possibility to move skyrmions in a straight line by tuning the frequencies of the standing SAWs [74].

Advantages

Utilising SAWs to manipulate thin film magnetism brings distinct advantages compared to using magnetic field, electric current and static strain:

- Technological maturity: SAW technology is well-established and can be easily integrated with complementary metal-oxide-semiconductor (CMOS) systems. IDT design and fabrication are relatively straightforward.
- Energy efficiency: Generating SAWs on specific powerful piezoelectric materials using transducers is efficient. These waves can propagate a few centimetres with minimal energy dissipation.
- Design simplification and precision: One pair of IDTs can remotely establish pinning site arrays. This enables the precise positioning of numerous magnetic spin structures simultaneously within the SAW beam path.
- Enhanced magnetisation dynamics: The dynamic strain introduced by SAWs alters the magnetisation dynamics, offering a novel approach to control the magnetisation behaviour.

Limitations

However, controlling thin film magnetism with SAWs also presents certain limitations, including:

1 Introduction

- Cost and processing complexity: Although SAW technology itself is mature, the piezoelectric substrates needed for the most efficient SAW generation and propagation – like lithium niobate and lithium tantalate – are more expensive and can require more complex processing than silicon substrates.
- Weak magnetoelastic coupling: While SAWs can propagate over large areas with minimal attenuation, this implies that the energy transfer between the SAW and the magnetic film is not particularly strong. Effective manipulation of magnetism with SAWs requires the magnetic film to be sensitive to the relatively small strains produced by the SAWs, which limited the choice of the magnetic materials. This weak coupling means that it is possible to control many devices simultaneously, the control over each might not be very strong or efficient.
- Long wavelength: Typical SAW frequencies range from tens of MHz to a few GHz, resulting in SAW wavelengths ranging from hundreds of microns to hundreds of nanometres. Consequently, SAWs are not suitable for controlling devices at the nanometres scale.
- Limited material choices: The need for strong piezoelectric materials limits the choice of substrates for SAW devices. Not all piezoelectric materials are equally effective, and some of the most efficient ones are not compatible with standard semiconductor processing, limiting their integration with other electronics.

Open questions

Moreover, there are still scientific and engineering questions need to be addressed:

- Magnetisation dynamics: The interplay between SAWs and magnetisation dynamics, particularly in thin films with PMA, needs further explanation. Specifically, the contributions of nodes and anti-nodes within standing SAWs during the magnetisation reversal process needs a deeper understanding.

- SAW properties and magnetisation correlation: There exists an unclear correlation between the SAW characteristics – namely frequency, wavelength, and amplitude – and the consequent influence on the magnetisation from these parameters needs to be elucidated.
- SAW and DW dynamics: Knowledge of the precise nature of the interaction between SAWs and DWs is incomplete. The potential perturbations introduced by intrinsic defects and disorders in thin films on SAW-assisted DW motion remains under-investigated for example. The influence of SAW frequency on DW dynamics, especially across films with different levels of disorder, also needs further investigation.
- Thermal impact from rf power: Potential thermal implications on devices pose another layer of complexity. The introduction of rf power may increase internal device temperatures, thereby affecting their operational efficacy. Thus, quantifying thermal effects and understanding their influence on device performance are essential for ensuring robust and efficient device applications, and to ensure that the correct mechanism for interaction is confirmed.

1.3 Thesis overview

In this thesis, a comprehensive exploration of the interplay between SAWs and magnetic thin films with PMA is presented, encompassing both experimental and theoretical perspectives. A schematic outline of the thesis structure is shown in Figure 1.5, along with the interactions between its constituent chapters.

- Chapter 1 sets the stage by introducing the background and motivations behind this project.

1 Introduction

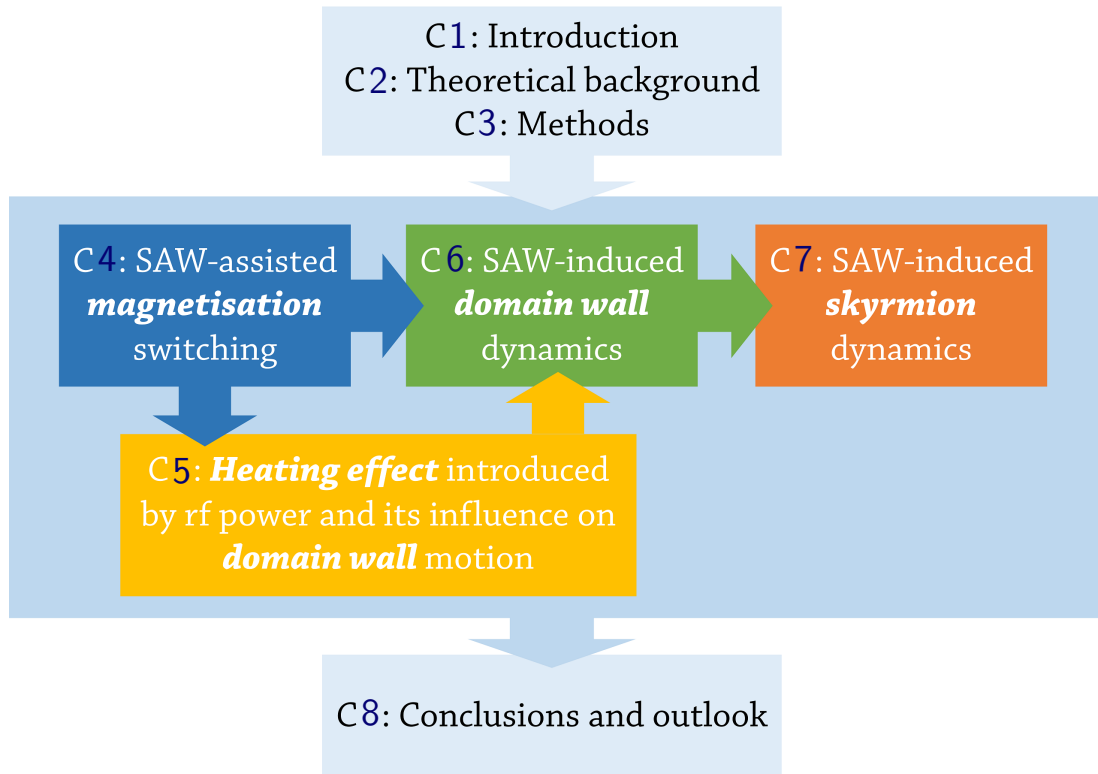


Figure 1.5: Thesis overview.

- Chapter 2 elucidates the foundational theoretical frameworks underpinning this study.
- Chapter 3 explains the experimental methodologies and computational method employed.
- Chapter 4 describes local magnetic anisotropy modification in Ta/Pt/Co/Ir/Ta thin films via standing SAWs through both experiments and micromagnetic simulations.
- Chapter 5 provides the experimental findings on the thermal implications due to

rf power, revealing its origin and influence on magnetic properties.

- Chapter 6 shows a detailed numerical investigation of SAW frequency impact on DW motion, particularly within thin films with varied anisotropy disorder using micromagnetic simulations.
- Chapter 7 introduces an innovative approach for the precise transport of skyrmions along predefined trajectories via orthogonal SAWs using micromagnetic simulations.
- Chapter 8 provides concluding remarks and offers ideas for the potential extension of this work.

1 Introduction

CHAPTER 2

Theoretical background

2.1 Introduction

This chapter focuses on the basic physical concepts that provide the theoretical foundations for this thesis, drawing inspiration from various textbooks and papers [75–80]. It provides a detailed discussion on the underlying theories and principles essential to understand the results presented in subsequent chapters. We firstly discuss magnetisation dynamics in terms of free energy and the effective field in thin films with PMA. We introduce the external magnetic field, the exchange interaction, the anisotropy, and the DMI all of which are key contributors to the behaviour of magnetisation in this project. Two spin structures, namely DWs and skyrmions, are then discussed in detail. DWs are the boundaries that separate two uniformly magnetised magnetic domains, while skyrmions are topologically protected particle-like spin structures that emerge in materials lacking inversion symmetry. Finally, the excitation and propagation of SAWs are described. SAWs are strain waves that travel along the surface of a piezoelectric material, with an amplitude typically decaying exponentially into the substrate. SAWs can induce dynamic strain in magnetic thin films, resulting in the magnetoelastic coupling effect that influences magnetisation dynamics. These concepts of magnetisation dynamics, spin structures, and SAWs form the foundational pillars of this project, providing the necessary theoretical framework to comprehend and interpret the research findings.

In this study, we use a concise notation for representing vectors and their magnitudes. Bold fonts, such as \mathbf{V} , indicate vectors. For the magnitude of vector \mathbf{V} , we employ V as opposed to the conventional $|\mathbf{V}|$. This approach is particularly useful when graphing figures in relation to the magnitude of magnetic fields.

2.2 Magnetisation dynamics

Magnetisation, \mathbf{M} , in ferromagnetic materials are inclined to align with a local field

2.2 Magnetisation dynamics

to minimise the energy of the system. This local field, known as the effective field \mathbf{H}_{eff} , governs the dynamics of the magnetic moments at any position $\mathbf{r}(x, y, z)$. The magnetisation dynamics can be described by

$$\frac{d\mathbf{M}(\mathbf{r})}{dt} = -\gamma\mathbf{M}(\mathbf{r}) \times \mathbf{H}_{\text{eff}}(\mathbf{r}), \quad (2.1)$$

where γ represents the gyromagnetic ratio. As a result, the magnetic moments undergo perpetual precession at a constant angle around the effective field (as shown in Figure 2.1a).

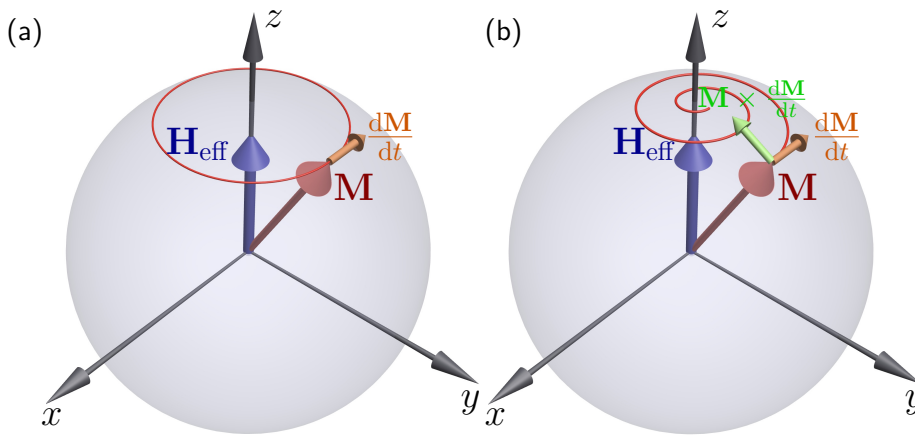


Figure 2.1: Magnetic moment precesses around the effective field \mathbf{H}_{eff} : (a) with a constant polar angle, and (b) with a spiral trajectory due to the damping.

However, experimental observations demonstrate that in the presence of an external magnetic field, the magnetisation tends to align predominantly parallel to the direction of that external field. To reconcile this discrepancy, a phenomenological dissipative term is introduced into the \mathbf{H}_{eff} in Equation 2.1. This dissipative term is given by

$$-\frac{\alpha}{\gamma M_s} \frac{d\mathbf{M}}{dt}, \quad (2.2)$$

2 Theoretical background

where α represents the Gilbert damping constant, and M_s is the saturation magnetisation. We have dropped the explicit dependence of the vector \mathbf{r} from $\mathbf{M}(\mathbf{r})$ to keep the notation more compact. We will use this shorthand throughout the thesis. By incorporating this dissipative term (Equation 2.2) to \mathbf{H}_{eff} in Equation 2.1, we obtain the well-known Landau–Lifshitz–Gilbert (LLG) equation

$$\frac{d\mathbf{M}}{dt} = -\gamma\mathbf{M} \times \mathbf{H}_{\text{eff}} + \frac{\alpha}{M_s}\mathbf{M} \times \frac{d\mathbf{M}}{dt}. \quad (2.3)$$

The LLG equation accounts for the damping effect, causing the magnetic moments to precess in a spiral path towards their equilibrium position, as shown in Figure 2.1b. This phenomenological adjustment delivers a more precise depiction of the magnetisation dynamics, aligning better with experimental observations.

The LLG equation describes the dynamics of magnetic moments in a ferromagnetic material. We define reduced moment by $\mathbf{m} = \mathbf{M}/M_s$, which follows the direction of the spin. The effective field (\mathbf{H}_{eff}) can be expressed as the first derivative of the total energy density with respect to the magnetisation, given by

$$\mathbf{H}_{\text{eff}} = -\frac{1}{\mu_0 M_s} \frac{\delta E_{\text{total}}}{\delta \mathbf{m}}, \quad (2.4)$$

where μ_0 is the permeability of vacuum and E_{total} represents the total internal free energy density of the system. This free energy density, E_{total} , encompasses different energy contributions, depending on the material properties, magnetisation configurations, and external conditions. In most systems, E_{total} can be obtained by

$$E_{\text{total}} = E_{\text{exch}} + E_{\text{ani}} + E_{\text{me}} + E_{\text{DMI}} + E_{\text{Zeeman}}. \quad (2.5)$$

The elements in this equation represent different energy contributions: exchange, anisotropy, magnetoelastic coupling, DMI, and external field. Together, these en-

ergy terms govern the behaviour of the magnetic moments within the ferromagnetic medium. We will examine each of these energy terms in the following sections.

2.3 Free energy and effective field

2.3.1 Exchange

In ferromagnetic materials, both the magnetic moment and spontaneous magnetisation are consequences of the exchange interaction among electrons, which is a quantum mechanical phenomenon. Magnetic moments inherently tend to align with each other, resulting in spin ordering that extends over macroscopic distances.

Consider an infinite lattice composed of spins located at positions $\{\mathbf{r}_i\}_i$. Each site located at \mathbf{r}_i possesses a spin represented by \mathbf{S}_i . Adhering to the Heisenberg model, the interaction Hamiltonian for the site \mathbf{r}_i is given by

$$\hat{\mathcal{H}}_i = -2 \sum_j J_{i,j} \mathbf{S}_i \cdot \mathbf{S}_j, \quad (2.6)$$

where the above sum is over the entire lattice and $J_{i,j}$ is the exchange constant.

While Equation 2.6 represents the most general form of the interaction Hamiltonian, the Heisenberg model introduces two additional key assumptions. Firstly, it is assumed that all lattice points are identical in terms of their physical properties. Secondly, the interactions between spins are considered to be short-ranged. The interactions in the model are, in fact, restricted to only nearest neighbours. Let $\mathcal{N}(i)$ be the set of all the nearest neighbours of the site i , then the assumptions taken lead us to the following form for $J_{i,j}$

$$J_{i,j} = \begin{cases} J & \text{if } j \in \mathcal{N}(i), \\ 0 & \text{otherwise.} \end{cases} \quad (2.7)$$

2 Theoretical background

It is further reasonable to assume that the two spins that are nearest neighbours are almost parallel to each other. Thus, of the the angle ϕ_{ij} between two adjacent spins S_i and S_j can be taken to be small. Incorporating this assumption gives

$$E_i = -2JS^2 \sum_{j \in \mathcal{N}(i)} \cos \phi_{ij} = \text{constant} + JS^2 \sum_{j \in \mathcal{N}(i)} \phi_{ij}^2, \quad (2.8)$$

where the last equality in holds using $\cos \phi_{ij} \approx 1 - \phi_{ij}^2/2$ for $\phi_{ij} \ll 1$.

The value of $|\phi_{ij}|$ can be approximated in terms of the reduced moments \mathbf{m}_i and \mathbf{m}_j (see Figure 2.2) as

$$|\mathbf{m}_i - \mathbf{m}_j| \approx \left| \left((\mathbf{r}_i - \mathbf{r}_j) \cdot \nabla \right) \mathbf{m}(\mathbf{r}_i) \right|, \quad (2.9)$$

thus the energy can be rewritten as

$$E_i = \text{constant} + JS^2 \sum_{j \in \mathcal{N}(i)} \left(\left((\mathbf{r}_i - \mathbf{r}_j) \cdot \nabla \right) \mathbf{m}(\mathbf{r}_i) \right)^2. \quad (2.10)$$

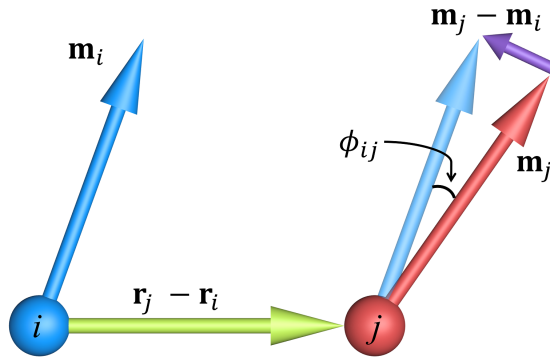


Figure 2.2: Magnetic moments at the nearest neighbours i and j represented by the reduced moments \mathbf{m}_i and \mathbf{m}_j . The angle between the two moments is ϕ_{ij} . The figure has been reproduced from [76].

2.3 Free energy and effective field

At the scales we are working with, the discrete lattice is can be effectively treated as a continuum. Taking this continuum approximation, we can write the exchange energy of the system (upto an constant term, which represents the energy of the system when all the spins in the material are fully aligned) as

$$E_{\text{exch}} = A_{\text{exch}} \int_V \left((\nabla m_x)^2 + (\nabla m_y)^2 + (\nabla m_z)^2 \right) d^3r, \quad (2.11)$$

where A_{exch} is the exchange stiffness constant given by

$$A_{\text{exch}} = 2JS^2za_0. \quad (2.12)$$

In this equation, z is the number of sites in the unit cell and a_0 is the distance between two nearest neighbours (lattice parameter). Plug Equation 2.11 into Equation 2.4, the exchange contribution to the effective field thus is

$$\mathbf{H}_{\text{exch}} = \frac{2A_{\text{exch}}}{\mu_0 M_s} \nabla^2 \mathbf{m}. \quad (2.13)$$

2.3.2 Magnetic Anisotropy

Magnetic materials exhibit specific directions known as the “easy” and “hard” directions of magnetisation. The magnetic moments naturally prefer to align in the easy direction, and to maintain a configuration where they do not align in this direction, additional energy is required. This energy variation required to magnetise a material depending on the direction of the applied field is referred to as magnetic anisotropy. The presence of uniaxial magnetic anisotropy gives rise to an extra energy term, which only relies on the angle θ_0 between the magnetic moments and the easy axis $\hat{\mathbf{u}}$. The anisotropy energy density, E_{ani} , up to the leading order in θ_0 can be expressed as follows

$$E_{\text{ani}} = K \sin^2 \theta_0 = K \left(1 - (\mathbf{m} \cdot \hat{\mathbf{u}})^2 \right), \quad (2.14)$$

2 Theoretical background

where K is the first order anisotropy constant, and $\mathbf{m} \cdot \hat{\mathbf{u}} = \cos \theta_0$. The effective field that associates with anisotropy thus can be expressed as

$$\mathbf{H}_{\text{ani}} = \frac{2K}{\mu_0 M_s} (\mathbf{m} \cdot \hat{\mathbf{u}}) \hat{\mathbf{u}}. \quad (2.15)$$

Magnetocrystalline and shape anisotropy

Two primary sources contribute to magnetic anisotropy: spin-orbit interaction and magnetic dipolar coupling. Spin-orbit interaction is characterised by a coupling between the magnetic moment and the orbital momentum, leading to an energy dependence on the orientation of magnetisation relative to the crystal axes. This phenomenon is referred to as magnetocrystalline anisotropy, as it reflects the crystal inherent symmetry. By applying strain to the material, the magnetocrystalline anisotropy can be modified, resulting in what is known as magnetoelastic anisotropy.

The dipolar interaction, or shape anisotropy, is influenced by the shape of the sample because of its long-range character [75]. If the magnetisation is uniformly aligned within a material, magnetic charges will appear at the surfaces, creating dipolar energy. This is especially significant for in-plane magnetisation in thin films. The energy density of shape anisotropy in thin films E_{sh} can be expressed as follows

$$E_{\text{sh}} = \frac{1}{2} \mu_0 M_s^2 \cos^2 \theta_0, \quad (2.16)$$

where recall that θ_0 represents the angle between the magnetic moment and the easy axis. Shape anisotropy is associated with the demagnetising field, which is the magnetic field generated by the magnetic material.

Magnetoelastic anisotropy

When a ferromagnetic material is magnetised, it undergoes a phenomenon known as magnetostriction, where its size experiences a slight change due to crystal deformation. This change in size reduces the anisotropy energy of the material. On the contrary, any deformation occurring in the crystal structure can also impact the anisotropy energy of the material. This connection between magnetic and elastic behaviour is commonly referred to as magnetoelastic coupling. The energy density of the magnetoelastic anisotropy E_{me} associated with this effect can be written as

$$E_{\text{me}} = B_1 \sum_{i=x,y,z} m_i^2 \epsilon_{ii} + B_2 \sum_{i \neq j} m_i m_j \epsilon_{ij}, \quad (2.17)$$

where B_1 and B_2 represent the magnetoelastic coefficients, ϵ_{ij} denotes the strain tensor, m is the normalised magnetisation, i and j are the Cartesian components (x, y, z). The effective field introduced by the magnetoelastic interaction thus can be expressed as

$$\mathbf{H}_{\text{me}}^{(i)} = -\frac{2}{\mu_0 M_s} \left(B_1 m_i \epsilon_{ii} + B_2 \sum_{j:j \neq i} m_j \epsilon_{ij} \right), \quad (2.18)$$

where $\mathbf{H}_{\text{me}}^{(i)}$ is the component of the effective field along the axis labeled by i .

Perpendicular magnetic anisotropy

Perpendicular magnetic anisotropy refers to the magnetic material having an easy axis perpendicular to its surface. The PMA results from the magnetic anisotropy at an interface, which is different from the magnetic anisotropy in the bulk. PMA is typically observed in thin films or multilayers that consist of magnetic materials with specific structural properties and interface conditions. It is commonly found in materials composed of transition metals combined with heavy elements or alloys with strong SOC. The magnetic anisotropy of the thin film K can be described by the

2 Theoretical background

volume and surface contributions K_v and K_s as

$$K = K_v + \frac{2K_s}{d}, \quad (2.19)$$

where d is the thickness of the magnetic layer in a thin film. K_v includes shape anisotropy, magnetocrystalline anisotropy, and magnetoelastic anisotropy contributions, with shape anisotropy being the dominant factor in this contribution.

2.3.3 Interfacial Dzyaloshinskii–Moriya interaction

The interfacial Dzyaloshinskii–Moriya interaction (DMI) arises in magnetic thin films that lack inversion symmetry. The Hamiltonian term acting between two adjacent spins \mathbf{S}_i and \mathbf{S}_j can be expressed as

$$\hat{\mathcal{H}}_{\text{DMI}} = (\mathbf{S}_i \times \mathbf{S}_j) \cdot \mathbf{D}_{ij}, \quad (2.20)$$

where \mathbf{D}_{ij} denotes the Dzyaloshinskii–Moriya vector (as illustrated in Figure 2.3). The Dzyaloshinskii–Moriya vector can be written as

$$\mathbf{D}_{ij} = D_{ij}(\hat{\mathbf{z}}_0 \times \hat{\mathbf{r}}_{ij}), \quad (2.21)$$

where D_{ij} is the interfacial DMI strength, and $\hat{\mathbf{z}}_0$ and $\hat{\mathbf{r}}_{ij}$ are unit vectors perpendicular to the interface and pointing in the plane of the magnetic layer and from site i to site j (i.e., unit vector in the direction of the vector $\mathbf{r}_j - \mathbf{r}_i$), respectively.

The sign of the D_{ij} value determines whether the DMI favours anticlockwise or clockwise rotations from \mathbf{S}_i to \mathbf{S}_j . The rotation direction, in turn, influences whether the DMI lowers or increases the spin energy. A strong DMI induces a spin tilt around the \mathbf{D}_{ij} vector. At the interface between the magnetic material and heavy metal, the Dzyaloshinskii–Moriya vector lies within the film plane as shown in Figure 2.3. The

2.3 Free energy and effective field

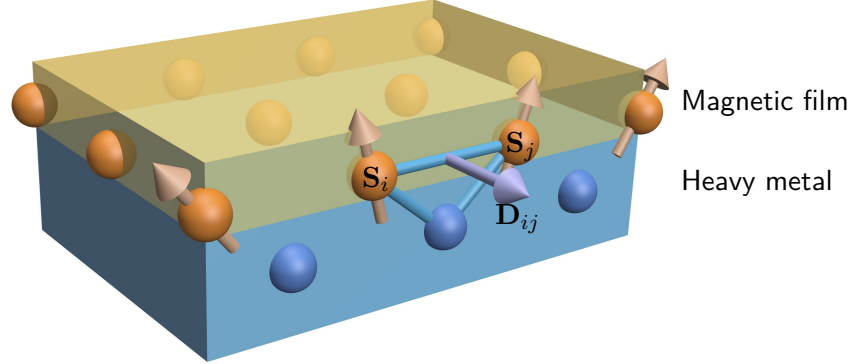


Figure 2.3: Schematic diagram illustrating the interfacial DMI at the interface between a magnetic film and a heavy metal. \mathbf{S}_i and \mathbf{S}_j are the spins of neighbouring atoms, and \mathbf{D}_{ij} is the corresponding Dzyaloshinskii–Moriya vector. The figure has been reproduced from [5].

energy density term due to the presence of DMI is

$$E_{\text{DMI}} = D \left((\mathbf{m} \cdot \nabla) m_z - (\nabla \cdot \mathbf{m}) m_z \right), \quad (2.22)$$

where D is the average DMI strength. The DMI-induced effective field can be expressed by

$$\mathbf{H}_{\text{DMI}} = \frac{2D}{\mu_0 M_s} \left((\nabla \cdot \mathbf{m}) \hat{\mathbf{z}}_0 - \nabla m_z \right). \quad (2.23)$$

2.3.4 Zeeman energy

Ferromagnetic materials respond to an external magnetic field \mathbf{H}_{ext} , defining the magnetisation process and hysteresis loop. The energy associated with the external magnetic field is known as the Zeeman Energy. The Zeeman energy density is given by the equation

$$E_{\text{Zeeman}} = -\mu_0 \mathbf{M} \cdot \mathbf{H}_{\text{ext}}. \quad (2.24)$$

2 Theoretical background

The effective field associated with Zeeman energy is simply $\mathbf{H}_{\text{eff}} = \mathbf{H}_{\text{ext}}$.

2.4 Magnetisation reversal

The process of magnetisation reversal often involves the nucleation and propagation of magnetic domains, where the magnetisation aligns uniformly. The process of magnetisation reversal in thin films exhibits several distinct characteristics. The nucleation field marks the point at which domains nucleate and the magnetisation begins to reverse. Remanence refers to the remaining proportion of the saturation magnetisation when no external field is applied. The coercivity is the strength of the field required for the average magnetisation in the film to reach zero. In the case of thin films with PMA, after the nucleation of domains, a propagation field is necessary to sustain the motion of DWs. This sequential process contributes to the complete magnetisation reversal in the thin film. A hysteresis loop is a graphical representation that illustrates the relationship between the magnetisation in a ferromagnetic material and the magnetic field strength applied to it. Figure 2.4a shows a typical hysteresis loop for a ferromagnetic material. If a material is magnetised to its saturation magnetisation by an external magnetic field, then when the applied field is reduced to zero, the magnetisation of the material reduces to remanence. A magnetic field with the strength of the coercivity is required to switch the magnetisation into the opposite direction. During this process, the magnetisation starts to reduce at a particular field strength, marking the nucleation of domains. In thin films with PMA shown in Figure 2.4b, magnetisation remains constant as the external field is reduced to zero, indicating a remanence that is similar as the saturation magnetisation. The magnetisation retains its value until the magnetic field is decreased further, resulting in a sharp switching at the domain nucleation field, which is comparable in magnitude to the coercivity.

2.4 Magnetisation reversal

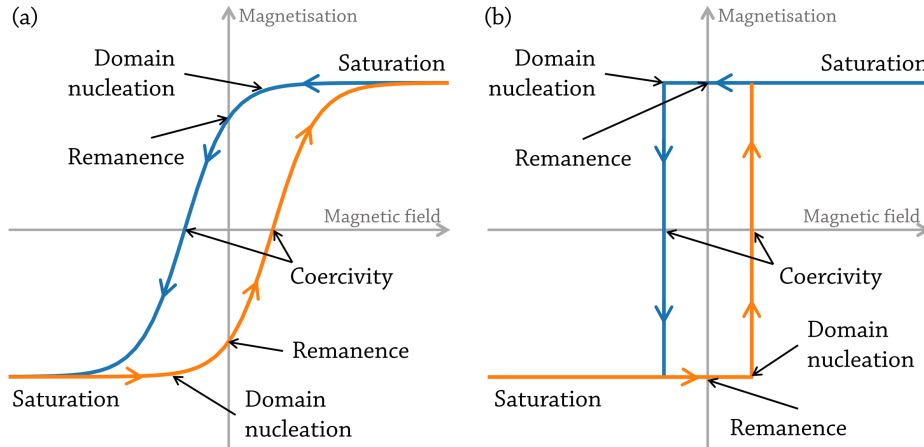


Figure 2.4: (a) Typical hysteresis loop of a ferromagnetic material. (b) Typical hysteresis loop of a thin film with PMA. The direction of the arrows shows the increasing or decreasing trend of the applied magnetic field.

2.4.1 Domain and domain wall

Magnetic domains correspond to regions within a material where the magnetisation is aligned in the same direction [20]. Each magnetic domain acts like a small magnet with its own magnetic field. A domain wall (DW) is a narrow region separating two magnetic domains with different magnetisation directions. DWs can be moved by an external field, as shown in Figure 2.5. Two different types of DWs, Bloch and Néel walls, are demonstrated in Figure 2.6 [45]. In a Bloch wall, magnetisation rotates uniformly in a plane perpendicular to the domain wall, while in a Néel wall, magnetisation rotates within the plane of the wall itself. In thin films with PMA, the magnetisation direction tends to be “up” and “down”. The DWs exist between two domains, gradually and smoothly reorienting the magnetic moments from “up” to “down” or from “down” to “up”.

2 Theoretical background

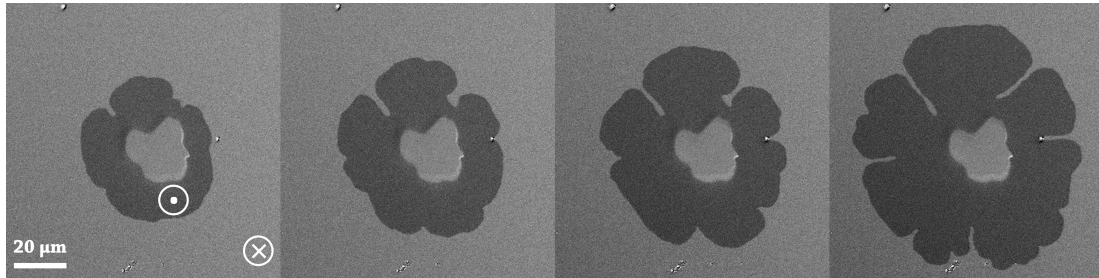


Figure 2.5: Domain and DW motion with an applied out-of-plane field in a Ta(5.0 nm)/Pt(2.5 nm)/Co(0.6 nm)/Pt(2.5 nm)/Ta(5.0 nm) thin film with PMA. The light grey area in the centre is the region where the thin film peeled off. The darker grey ring is magnetisation pointing out of the plane, and the light grey pointing into the plane.

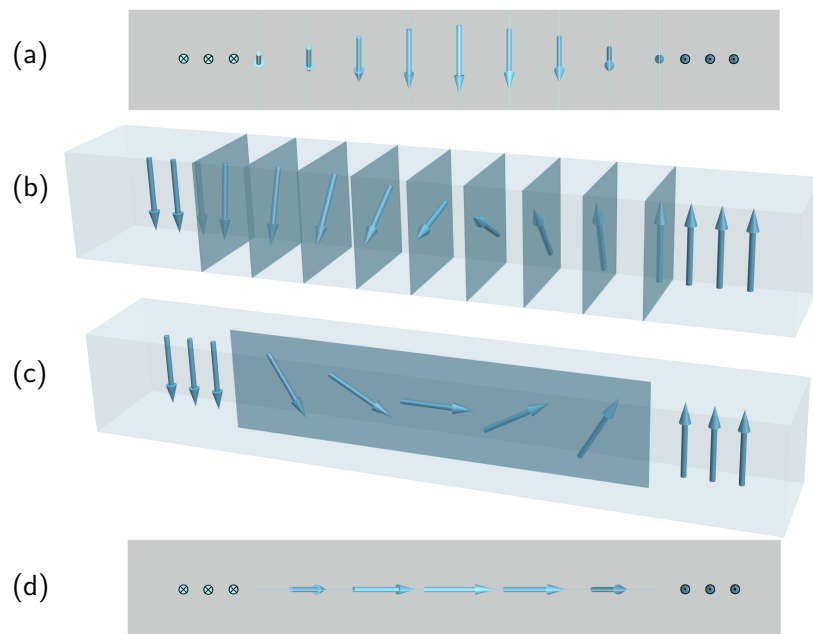


Figure 2.6: Diagram of the DW structures: (a) top view of the Bloch wall, (b) isometric view of Bloch wall, (c) isometric view of the Néel wall, and (d) top view of the Néel wall.

2.4.2 Domain wall motion

DW motion can be induced by an external magnetic field through two distinct mechanisms (Figure 2.7). In an ideal thin film without any defects or disorder, when subjected to low fields, the DW velocity increases with the field strength along with a slight distortion in the wall structure. Above a threshold H_W , DW velocity experiences an abrupt decrease with the field (Figure 2.7b). This phenomenon is widely known as Walker breakdown, which is characterised by an alternating DW structure and the precession of magnetisation inside the DW around the applied field [81].

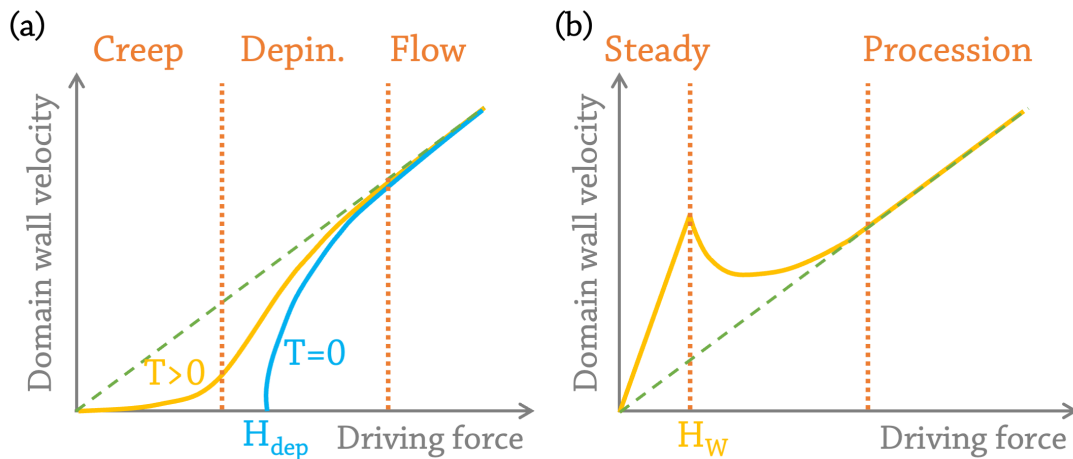


Figure 2.7: DW velocity regimes in relation to driving force. (a) DW motion is within the creep and thermally activated regimes at a low driving force and a finite temperature. DW motion shows less dependent on thermal energy in the depinning regime at a higher driving force and eventually shows a linear dependence on the driving force in the flow regime. (b) Steady and precessional regimes are separated by the Walker breakdown (H_W), where the DW velocity reduces with the driving force increases.

Defects and disorders within thin films significantly influence the DW motion. In a thin film containing such imperfections, at zero temperature, the DW becomes

2 Theoretical background

strongly entangled with the defects and remains pinned for all fields below a critical value known as the depinning field H_{dep} (see Figure 2.7a). The depinning field is defined as the minimum external magnetic field required to surpass the local energy barrier that hinders the DW motion [82, 83]. At finite temperatures T , DW motion can be activated by thermal fluctuations, which initiate localised depinning process. This regime is commonly referred to as the creep regime, where DW velocity increases with the external magnetic field and follows the creep law, which can be expressed as

$$v = v_0 \exp\left(-\frac{U_c}{k_B T} \left(\frac{H_{\text{dep}}}{H_{\text{ext}}}\right)^{\frac{1}{4}}\right), \quad (2.25)$$

where U_c is the pinning energy barrier induced by disordered energy landscape, k_B is the Boltzmann constant, and v_0 is a numerical prefactor [22, 84]. This behaviour holds even when the H_{ext} is smaller than the H_{dep} .

For fields exceeding H_{dep} at both temperature conditions (zero and finite temperatures), the DW velocity increases with the field until it enters the viscous regime where the DW velocity exhibits a wide plateau [85–88] instead of a Walker breakdown (as shown in Figure 2.8 [87]). This DW velocity saturation effect can be attributed to an enhanced energy dissipation at defects in the thin film [87], as well as the blocking [89] and annihilation [90] of vertical Bloch lines (VBLs). VBLs are curling magnetic structures that appear inside DWs and introduce complexity to the static and dynamic properties of the DWs [91, 92]. Defects within the thin films give rise to variations in the energy landscape along the DW, which in turn affect the wall structure and the local mobility of the DW as it traverses its path. The DW structure thus directly influences the local mobility. As a result, the nucleation, propagation, and annihilation of VBLs have a significant impact on the overall DW dynamics.

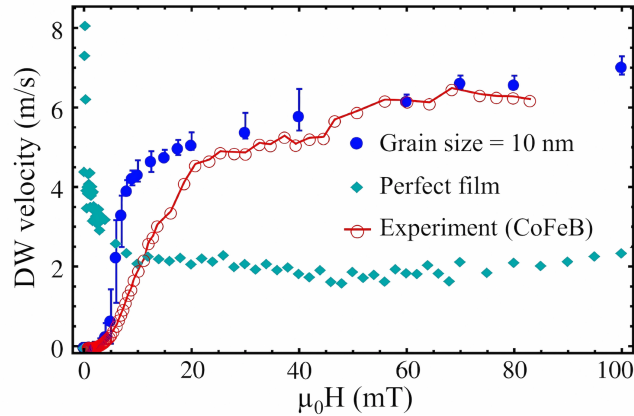


Figure 2.8: DW velocity as a function of the magnetic field in thin films with disorder. Simulated data for a grain size of 10 nm with 5% anisotropy dispersion shows a velocity plateau indicating incoherent precession. Experimental result from a Ta/CoFeB/MgO film is without the Walker breakdown. A perfect film response includes the Walker breakdown. The figure has been reproduced from [87].

2.4.3 Skyrmions

Magnetic skyrmions are topologically protected particle-like magnetic spin structures. Within a skyrmion, the spins undergo a gradual rotation with a consistent chirality, transitioning from an upward direction at one edge, through the center, and finally to a downward direction at the other edge. The symmetry of the system plays a crucial role in determining the energetically preferred spin configuration of the formed skyrmions.

As shown in Figure 2.9, there are two typical types of magnetic skyrmions according to the spin configuration: Néel [93, 94] and Bloch skyrmions [95, 96]. The distinct spin configuration arises from the inherent symmetries in the spin interactions, which can be influenced by factors such as the crystal lattice or interface properties. For instance, Bloch skyrmions are typically observed in bulk materials, facilitated by the absence of crystal inversion symmetry and the presence of high SOC atoms, as seen

2 Theoretical background

in certain ferromagnetic alloys like B20 materials [97]. In contrast, Néel skyrmions are commonly associated with interfacial DMI in multilayer thin films [98].

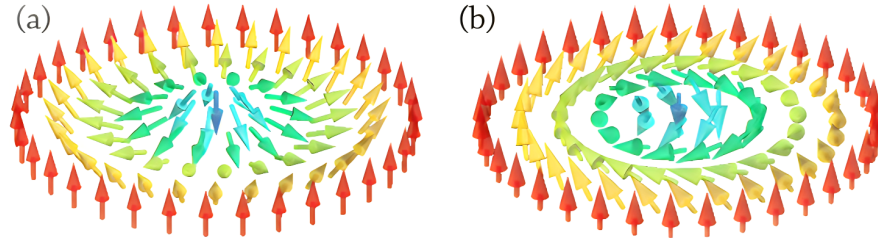


Figure 2.9: Magnetic texture of skyrmions: (a) Néel skyrmion and (b) Bloch skyrmion. Figures have been reproduced from [5].

The spin direction at a given spatial position $\mathbf{r} = (x, y)$ can be represented by $\mathbf{m}(\mathbf{r})$. The spin configuration of a skyrmion is characterised by its topological skyrmion number (N_{sk}), defined as

$$N_{\text{sk}} = \frac{1}{4\pi} \int \mathbf{m} \cdot (\partial_x \mathbf{m} \times \partial_y \mathbf{m}) dx dy = 1. \quad (2.26)$$

Similarly, a spin configuration with a skyrmion number of -1 is known as an anti-skyrmion, which can be observed in magnets exhibiting D_{2d} symmetry [99, 100]. The finite size of skyrmions enables them to exhibit particle-like behaviour, allowing for movement, interaction, and excitation at specific dynamic modes.

2.5 Surface acoustic waves

2.5.1 Piezoelectric effect

The piezoelectric effect refers to the ability of certain materials to generate an electric charge when subjected to mechanical strain, known as the direct piezoelectric effect. This effect is reversible, meaning that materials exhibiting piezoelectricity can also

generate mechanical strain in response to an electric field, known as the converse piezoelectric effect [101]. The origin of the piezoelectric effect lies in the linear electromechanical interaction between the mechanical and electrical states in crystalline materials lacking inversion symmetry [80]. When a stress is applied to such a crystal, an imbalance of charge occurs due to the movement of charges within the crystal, as depicted in Figure 2.10. This charge movement leads to a change in surface charge density and the creation of an electric field between the faces of the crystal. The strength of the electric field increases with the magnitude of the applied stress. On the contrary, by applying an electric voltage, a (compressive/tensile) strain can be induced in the material. The magnitude of the strain is proportional to the applied voltage.

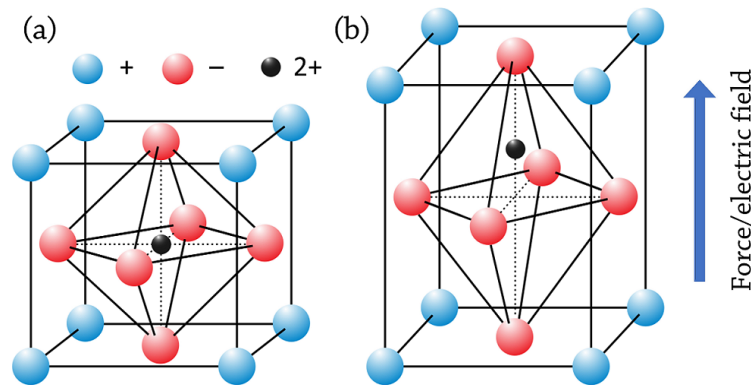


Figure 2.10: Schematic of (a) a piezoelectric unit cell and (b) a piezoelectric unit cell with force or electric field applied. Charges of molecules are arbitrary and for illustration only. Figures have been reproduced from [102].

2.5.2 SAW excitation and propagation

Based on their wave motion characteristics, several types of SAWs exist, including Rayleigh waves and Love waves. Rayleigh waves propagate along the free surface

2 Theoretical background

of a solid material, and they are characterised by elliptical particle motion. This motion includes both vertical and horizontal components, leading to an overall elliptical trajectory. Love waves exhibit purely horizontal particle motion that occurs in a horizontal plane parallel to the surface. This motion is restricted to the plane of the wavefront. In this thesis, Rayleigh waves were chosen because Rayleigh waves can easily form both travelling waves and standing waves, allowing us to explore different types of waves on the magnetisation dynamics. However, when the Rayleigh waves encounter the thin films, due to the different mechanical properties between the piezoelectric substrate and the thin film, Love wave may occur in the thin film. SAWs are commonly generated on a piezoelectric material using IDTs consisting of interleaved electrodes (as shown in Figure 2.11b). By applying an alternating signal delivering rf power to either IDTs (IDT1 in Figure 2.11b), a periodic strain field is induced on the surface of the piezoelectric material, resulting in the formation of a standing SAW (see Figure 2.11a). This standing SAW propagates in both directions (left and right in Figure 2.11b) away from the IDTs. The IDTs exhibit optimal rf power to mechanical wave efficiency when the SAW wavelength λ_{SAW} matches the periodicity of the electrode structure d_{IDT} . The relationship between the centre frequency f_0 and the wavelength λ_{SAW} of the SAWs then can be expressed as

$$f_0 = \frac{v_{\text{SAW}}}{\lambda_{\text{SAW}}}, \quad (2.27)$$

where v_{SAW} represents the speed of the SAW. Therefore, by adjusting the pitch of the IDTs, the centre frequency of the SAWs can be modified accordingly.

The propagation of a mechanical wave in a piezoelectric material gives rise to an associated electrostatic wave potential, denoted as ϕ (as depicted in Figure 2.11a). The wave potential of an electrode subjected to a continuous wave voltage V_1 can be described as

$$\phi^{\pm} = \mu_s V_1, \quad (2.28)$$

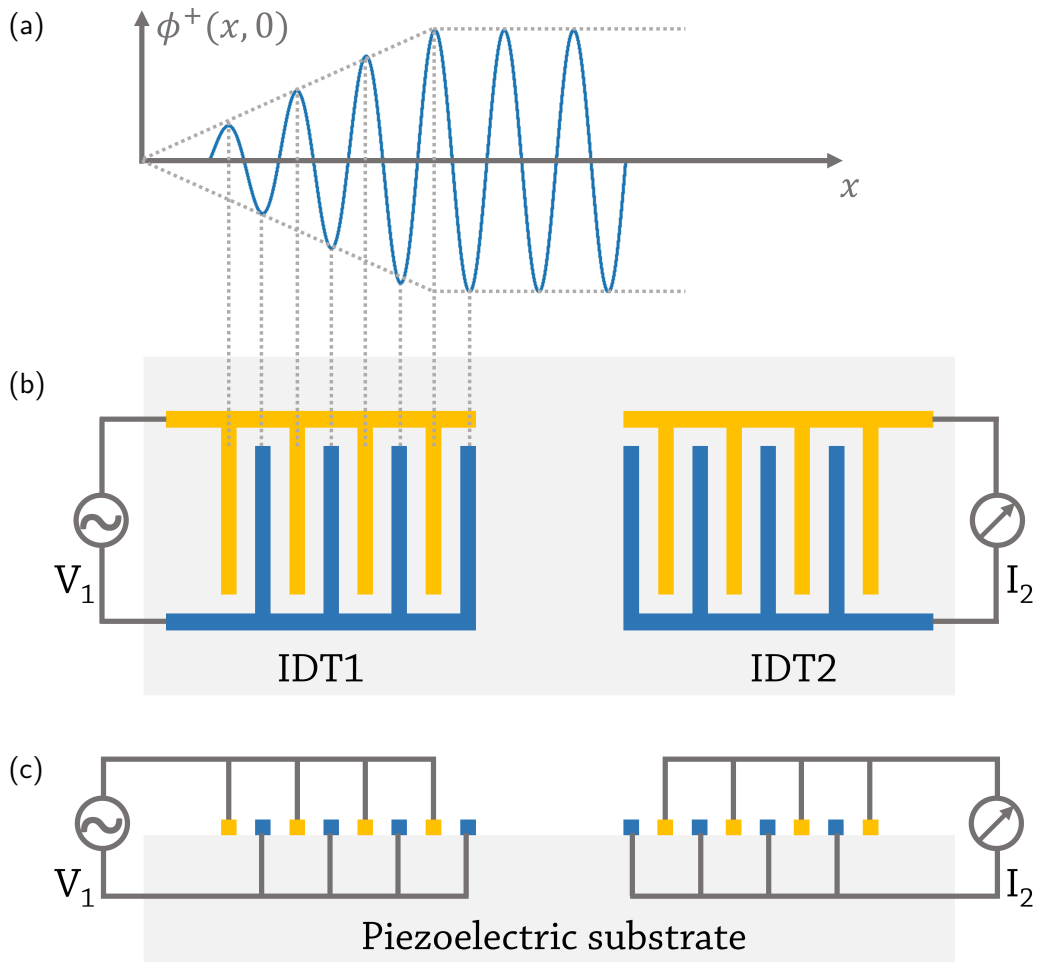


Figure 2.11: Excitation of SAWs. (a) Wave potential as a function of distance. SAW electrical potential can be formed by applying alternating voltage to the IDTs that are patterned onto a piezoelectric material. (b) and (c) are the top and side view of the SAW device, respectively. The rf power is applied to the IDT1, generating SAWs that move towards IDT2, where they are subsequently detected. Figures have been reproduced from [79].

2 Theoretical background

where ϕ^+ and ϕ^- correspond to the wave propagating towards the right and left directions, respectively, while μ_s represents a substrate-dependent constant that is unaffected by the frequency of the applied voltages.

Each electrode within the IDT can be considered as a discrete source for the generation of SAWs. When IDTs with electrodes spaced periodically with a period of d_{IDT} are excited by alternating voltages $V_n = (-1)^n V_0$ with a frequency of f , the resulting wave potential for the rightward propagating wave ϕ^+ can be calculated as the vector sum of contributions from each electrode. It can be represented as

$$\phi^+(0) = \mu_s V_0 \sum_{n=0}^{N_f-1} (-1)^n \exp\left(\frac{inkd_{\text{IDT}}}{2}\right), \quad (2.29)$$

where n represents the n^{th} electrode, N_f is the total number of electrodes, and $i^2 = -1$. The wavenumber $k = \omega/v$, where the angular frequency $\omega = 2\pi f$. This wave potential is a geometric series, where the elements become unity and add constructively when $kd_{\text{IDT}}/2 = m\pi$ with m being an odd integer. As a result, the wave potential reaches its maximum value when $d_{\text{IDT}} = m\lambda_{\text{SAW}}$ for some odd integer m .

As the frequency moves away from the centre frequency (f_0), the addition of components from individual electrodes becomes incoherent, resulting in a wave potential given by

$$|\phi^+(f)| = \left| \frac{\sin X}{X} \right|, \quad (2.30)$$

where X is the detuning parameter defined as

$$X = \frac{N_p \pi (f - f_0)}{f_0}. \quad (2.31)$$

In this equation, N_p corresponds to the number of IDT periods ($N_p = N_f/2$). The variation of the wave potential with respect to the detuning parameter X is illustrated

in Figure 2.12.

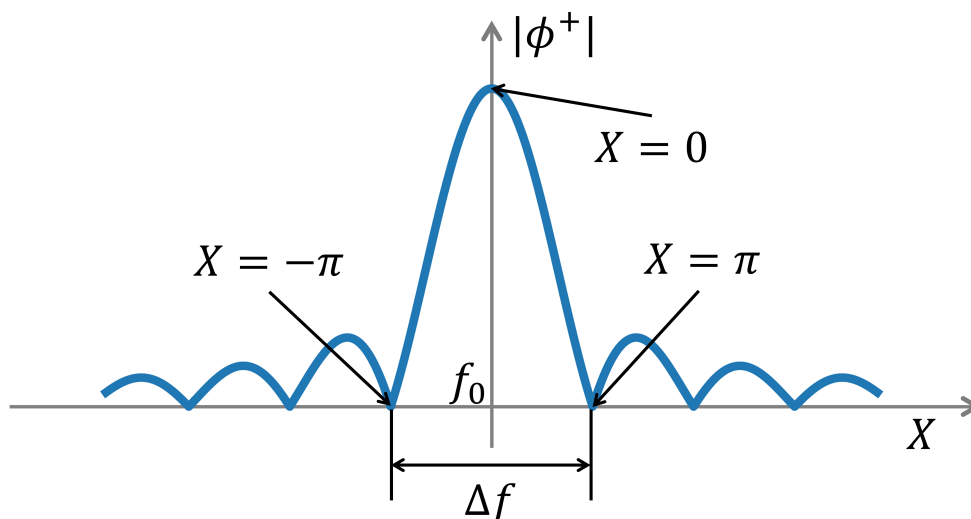


Figure 2.12: IDT response ($|\sin(X)/X|$) as a function of the detuning parameter X . The figure has been reproduced from [79].

The wave potential ϕ^+ becomes zero when X in Equation 2.31 is an integer multiple of π . This phenomenon occurs due to the complete cancellation between electrode contributions. The frequency interval Δf between the first nulls on either side of the centre frequency (see Figure 2.12), therefore, can be written as

$$\Delta f = \frac{2}{N_p} f_0. \quad (2.32)$$

Thus, the bandwidth of the IDT B defined as $\Delta f/f_0$ is given by

$$B = \frac{2}{N_p}. \quad (2.33)$$

When the acoustic wave reaches the receiving electrodes, the wave potential induced by the incident wave leads to a flow of current in the receiving interdigitated loaded

2 Theoretical background

transducer (IDT2 in Figure 2.11b). This current flow can be detected by an external detection circuit. Similar to the transmitting IDT, the receiving IDT also exhibits optimal performance when the periodicity of the transducer matches the wavelength of the acoustic wave.

2.6 Summary

This chapter laid the essential theoretical groundwork necessary for interpreting the experimental results presented in the subsequent chapters. The dynamics of magnetisation were analysed in detail, with a specific emphasis on the roles of free energy and the effective field within thin films with PMA. The discussion focused on the various energy terms contributing to magnetisation dynamics, including exchange interaction, anisotropy, DMI, and Zeeman energy. Two primary spin structures that form the subject of this thesis, DWs and skyrmions, were introduced in detail. The chapter provided insights into the generation and propagation of SAWs. It emphasised the dynamic strain that SAWs induce in magnetic thin films, leading to a magnetoelastic coupling effect that, in turn, influences magnetisation dynamics. In summary, this chapter laid the groundwork for the project, with critical insights into magnetisation dynamics, spin structures, and SAWs serving as its cornerstone.

CHAPTER 3

Methods

3.1 Introduction

This chapter provides an overview of the methods and equipment used for the fabrication and characterisation of the thin films and SAW devices investigated in this study. The fabrication of magnetic thin films was achieved using direct current magnetron sputtering (dcMS). Layer thickness measurements, determination of PMA, and observation of the magnetic domains were carried out using X-ray reflectometry (XRR) and wide-field Kerr microscopy. The IDTs were prepared in a class 100 cleanroom facility using a maskless photolithography technique. Scattering parameters (S-parameters) of the IDTs were characterised using a vector network analyser (VNA). Micromagnetic simulations were also performed to study the effect of SAWs on magnetisation dynamics using Mumax3. Ta/Pt/Co/Ir/Ta and Ta/Pt/Co/Ta thin films with PMA were chosen for investigation in Chapter 4 and Chapter 5, respectively.

Ta was chosen to be the buffer layer since it tends to form a (111) face-centred-cubic layer and introduce an atomically smooth interface between the Pt/Co layers. This can promote the formation of the smooth and (111) preferred orientation Pt layer and improve the PMA. To determine the basic magnetic properties such as thickness and PMA, thin films were deposited on silicon wafers. Lithium niobate (LiNbO_3) wafers were also used as substrates to support the propagation of SAWs. The IDT geometry was designed to excite SAWs with frequencies of ~ 100 MHz and ~ 50 MHz for Chapter 4 and Chapter 5, respectively. Note that the chosen SAW frequencies are well-below the FMR frequency of the thin films. The SAW device was mounted in a co-planar waveguide (CPW) made of the copper-covered prototype circuit board (PCB) and then was connected to a VNA.

3.2 Magnetic thin film fabrication

3.2.1 Substrate and cleaning process

Substrate

One-side polished 128° Y-cut LiNbO_3 (PI-KEM) substrates with a thickness of 0.5 mm were chosen in this study. This material is known for its strong piezoelectric coupling efficiency. The substrate is 128° rotated from the $+Y$ axis through the $+Z$ axis about the X axis (see Figure 3.1a). The SAW propagating velocities in X axis and the direction perpendicular to X axis (see Figure 3.1b) are 3982 m/s and 3640 m/s, respectively [103]. For this study, SAW propagation along the X direction was preferred. By applying an electric voltage to the piezoelectric material, the piezoelectric effect induces deformation in the substrates. The chosen LiNbO_3 substrates provided the necessary piezoelectric properties for efficient SAW generation and propagation.

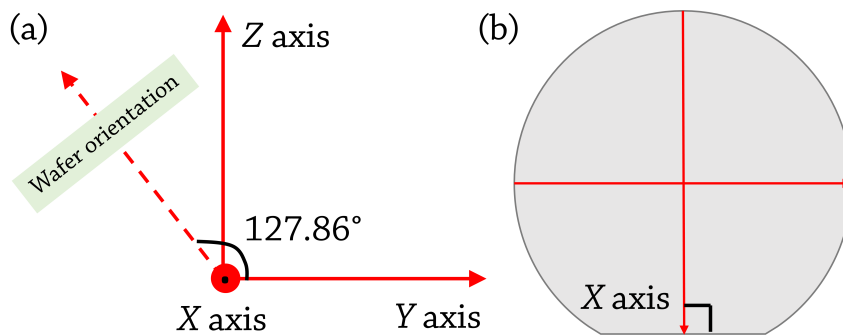


Figure 3.1: Schematic representation of the 128° Y-cut LiNbO_3 . (a) Wafer orientation is normal to the X direction, and with rotation of this crystal axis by 128° from the Y direction. (b) X axis and the direction perpendicular to X axis of the LiNbO_3 . Figures have been reproduced from [101].

3 Methods

Cleaning process

In order to achieve high-quality thin films with low defects and strong adhesion, the substrates underwent a thorough cleaning process. The cleaning procedure involved ultrasonic cleaning using acetone for 5 minutes to remove any dirt and organic residues present on the substrate surface. Subsequently, the substrates were subjected to another 5 minutes of ultrasonic cleaning using isopropanol. After the cleaning process, the substrates were carefully dried using compressed air before being loaded into the deposition chamber. This cleaning process ensured that the substrates were free from contaminants and ready for the deposition of thin films.

3.2.2 Thin film deposition

The magnetic thin films used in this thesis were fabricated by direct current magnetron sputtering (dcMS). This deposition technique is widely utilised in research and industry due to its advantages such as high deposition rate and cost-effectiveness, and precise control over thin film structure and thickness, even down to sub-nanometre.

The dcMS system used in this work was equipped with eight targets, two of which were specially designed for depositing magnetic materials. The base pressure of the chamber can reach 3.0×10^{-6} Pa with the application of cryo-pump and liquid nitrogen. During the deposition process, an Argon (Ar) atmosphere was maintained at a pressure of $\sim 3.3 \times 10^{-4}$ Pa. A schematic of a magnetron gun, which is a key component in the dcMS system, is shown in Figure 3.2. The electric and magnetic fields are shown in Figure 3.3a. In the deposition process, Ar gas is ionised into plasma by an electric field applied between the target and gun shield [104]. The magnetic field generated by the permanent magnets is arranged in such a way that it traps electrons near the target surface. This increases the efficiency of ionisation and confines the plasma close to the target. The motion of the electrons and Ar ions is in

3.2 Magnetic thin film fabrication

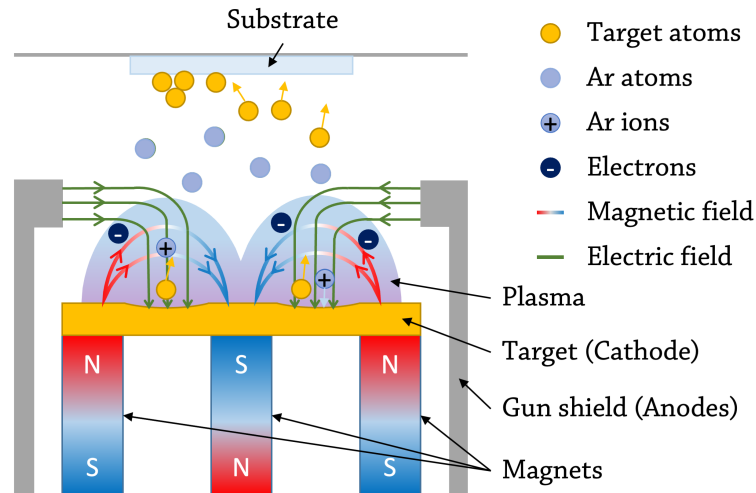


Figure 3.2: Diagram of the dcMS. An electric field is applied between the target (cathode) and gun shield (anode) to ionise Ar. The plasma shape is controlled by permanent magnets behind the target. Material is removed from the target by the Ar ions that repeatedly hit the target. The target material is then impinged onto the substrate surface. The figure has been reproduced from [45].

cyclotron motion with a drift motion in the presence the magnetic field \mathbf{B} and electric field \mathbf{H} (as shown in Figure 3.3b). The trajectory of the positively charged Ar ions is lower than that of the electrons as the target is negatively charged due to the electric field. When these Ar ions collide with the target, target atoms are ejected from the target material (see Figure 3.3b). These target atoms then collide with the plasma, eventually reaching the substrate and forming the thin film. The cyclotron with drift motion of the electrons and ions is the most significant at the region where $\mathbf{E} \cdot \mathbf{B} = 0$. Therefore, target material removal occurs at these regions forming a ring shape on the target (as shown in Figure 3.3). Subsequent collisions between electrons and Ar atoms generate additional Ar ions and electrons, significantly boosting deposition efficiency. The substrates were fixed on a rotatable wheel, allowing them to be

3 Methods

positioned in front of different target materials. Magnetic thin films with desired structures can be obtained by moving substrates among different materials. The thickness of the deposited thin films was controlled by the deposition rate of the material and deposition time.

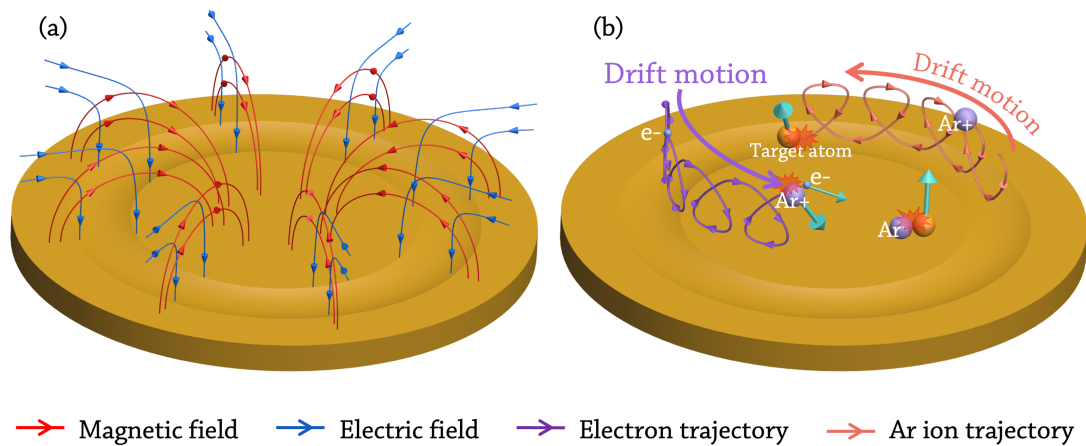


Figure 3.3: (a) Diagram of the distribution of the magnetic and electric fields in dcMS. (b) Diagram of the motion of the particles in dcMS. In the presence of the electric and magnetic fields, electrons and Ar ions exhibit cyclotron motion with drift motion within zones where $\mathbf{E} \cdot \mathbf{B} = 0$. The collision of Ar ions with the target material can cause the ejection of target atoms. These target atoms then collide with the plasma, eventually reaching the substrate and forming the thin film. Further collisions between electrons and Ar atoms generate additional Ar ions and electrons, significantly boosting deposition efficiency. The cyclotron motion radii of Ar ions and electrons are similar, with the electron trajectory typically positioned above that of Argon ions (due to the target is negative charged), resulting in partial overlap of their paths.

3.3 Magnetic thin film characterisation

3.3.1 Deposition rate calibration

X-ray reflectometry (XRR) is a surface-sensitive analytical technique employed to determine the thickness and roughness of thin films. In this work, XRR was utilised to calibrate the deposition rate of the thin films. For our measurements, we detected the intensity of X-rays reflected from a flat surface at low angles ranging from 0.5° to 8° .

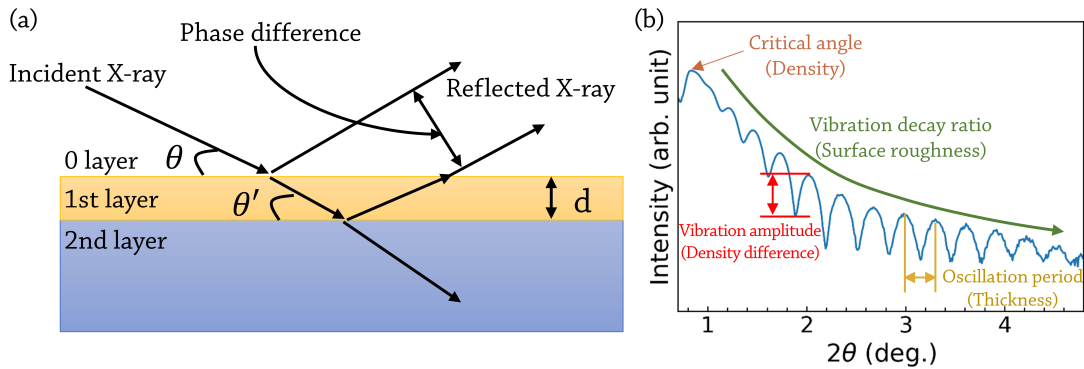


Figure 3.4: (a) Diagram of XRR principle and (b) XRR patterns for the Co thin film deposited onto a Si substrate.

The basic principle of XRR is to detect the intensity of a beam of reflected X-ray from a flat surface [105], as illustrated in Figure 3.4a. If the interface is not perfectly sharp or smooth, the intensity of the reflected X-ray deviates from the prediction based on the law of Fresnel reflectivity. To obtain the thickness, roughness, and density of each thin film layer, the measured XRR data was fitted with a simulated curve using the recursive Parratt formalism combined with the rough interface formula [106]. The relation of the fringes and the film thickness can be expressed by a modified Bragg equation as

$$n\lambda_X = 2d\sqrt{\sin^2 a_i - \sin^2 a_c}, \quad (3.1)$$

3 Methods

where the n is integer number of fringes, λ_X is the wavelength of the X-ray, d is the thickness of the film, a_i is the angle of the fringes, and the a_c is the critical angle. GenX 3 software was used to fit the XRR data [107]. Figure 3.4b shows an example XRR pattern for a Co thin film deposited on a Si substrate. The deposition rates of the materials used in this work, obtained at specific applied currents, are summarised in Table 3.1.

Table 3.1: Deposition current and deposition rate of materials used in this thesis.

Material	Current (mA)	Deposition rate ($\text{\AA}/\text{s}$)
Ta	50	1.43 ± 0.03
Pt	25	1.72 ± 0.03
Ir	25	0.91 ± 0.02
Co	50	0.89 ± 0.02

3.3.2 Hysteresis loop and domain image

A wide-field Kerr microscope was used to measure hysteresis loops and image magnetic domains. The magneto-optic Kerr effect (MOKE) refers to when light reflects from a magnetised surface and may change its polarisation and reflected intensity [20]. The MOKE measurement is a highly sensitive technique for detecting changes in magnetisation within a region of a sample. It serves as a rapid and reliable method for determining the presence of PMA in magnetic thin films.

The magnet coils of the Kerr-microscope were powered by a Kepco power supply and cooled by water. Figure 3.5a shows the light path from the light-emitting diode (LED) through the optics to the surface of the samples and then reflected to the camera [108]. MOKE can be further classified into four categories based on the direction of the magnetisation vector relative to the reflecting surface and the plane

3.3 Magnetic thin film characterisation

of incidence: polar MOKE, longitudinal MOKE, transversal MOKE, and quadratic MOKE. In this study, only polar MOKE was employed to characterise the thin films. For polar MOKE, a slit was used to select the centre of the polarisation cross, ensuring that the reflection magnetisation vector was perpendicular to the reflection surface and parallel to the plane of incidence.

Figure 3.5b–e depict the primary magneto-optical effects observed in a Kerr microscope, focusing on the polar and longitudinal Kerr effects. For light incident perpendicularly to the sample, in-plane magnetised domains exhibit no contrast, as no reflected light aligns with the in-plane direction. On the other hand, out-of-plane domains display the most potent vectorial components, yielding maximum contrast. To obtain a contrast for in-plane domains, one can adjust the light incidence to an oblique angle. Figure 3.5c presents a scenario where light is directed onto the sample from the rear of the figure. This setup produces contrast between domains with magnetisation components parallel to the incidence plane. Yet, transverse domains lack contrast, as their magnetisation component does not align with the reflected light. This phenomenon is evident in Figure 3.5d, where such domains display maximum contrast when light is incident from the left, while vertical in-plane domains remain without contrast. Figure 3.5e illustrates the effects when the direction of light incidence is inverted along the same axis as Figure 3.5d. Here, while transverse domains retain their lack of contrast, the longitudinal domains exhibit a contrast reversal compared to Figure 3.5d. In all cases of oblique incidence, the polar Kerr effect is apparent because the vectorial components of polar domains consistently align with the reflected light beam. The orientation of the incident and reflected beams does not influence the polar Kerr effect.

3 Methods

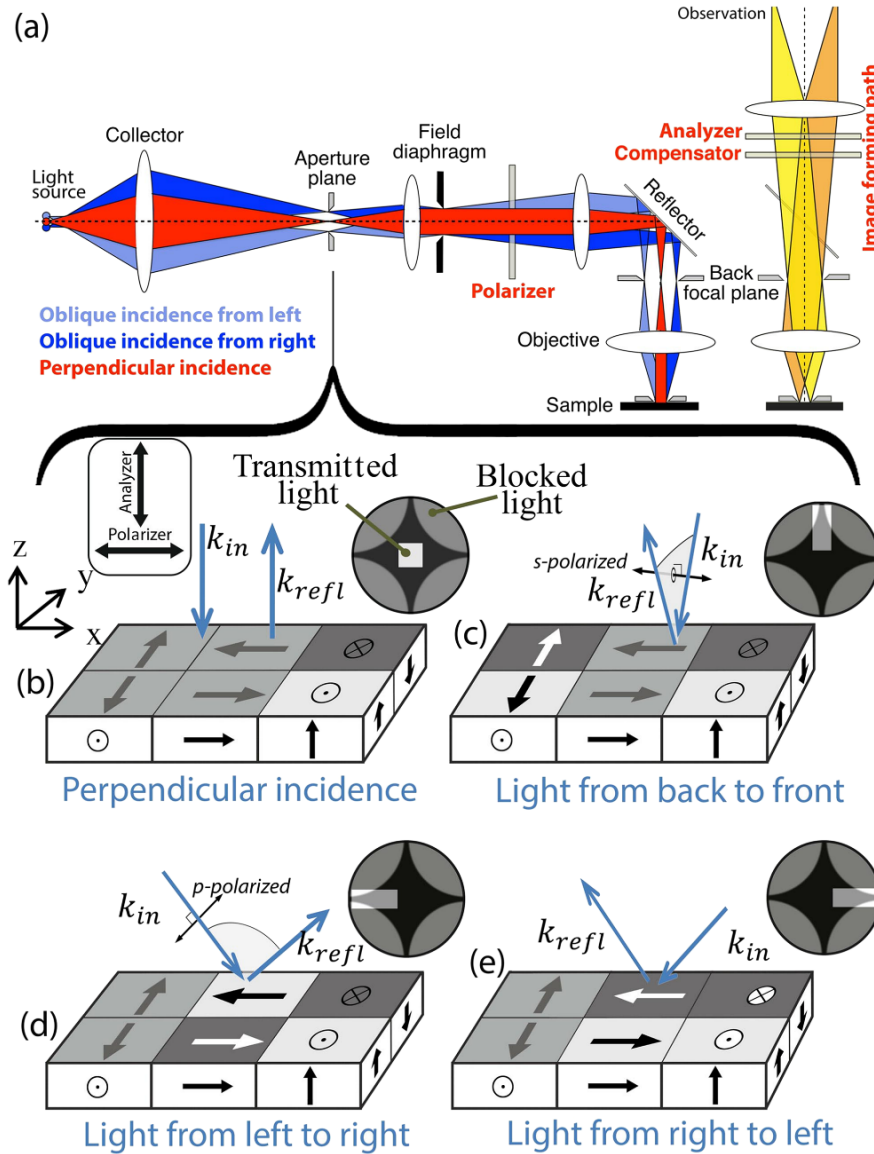


Figure 3.5: Diagram of the wide-field Kerr microscope. (a) The light paths for illumination and the image formation. The movable slit can be used to adjust the sensitive directions: (b) polar contrast, (c) longitudinal with s-polarised light, and (d) and (e) the longitudinal in transverse direction with p-polarised light with direct and inverted contrast, respectively [108].

3.4 Surface acoustic wave device

3.4.1 Device design

Interdigitated transducer geometry

SAW devices with various centre frequencies were designed and fabricated for this study. An example of the design of IDTs that generate SAWs with a centre frequency of approximately 50 MHz is illustrated in Figure 3.6. In all the IDTs fabricated in this thesis, the ratio of electrode width to spacing was maintained at 1:1 to maximise the SAW power. The acoustic aperture (defined by the length between the overlapped region of IDT electrodes in the direction perpendicular to the SAW propagation direction) was designed to be 500 μm for convenient observation under an optical microscope and to maximise the interaction with our patterned magnetic films.

The widths of the electrodes and the separation between them play a crucial role in determining the centre frequency of the SAW device. Taking into account the SAW propagating velocity of ~ 4000 m/s, to generate SAWs with frequencies of approximately 50 MHz and 100 MHz (devices used in Chapter 4 and Chapter 5, respectively), the widths of the electrodes were set as 20 μm and 10 μm , respectively, with the same separations as the widths. The dimensions of the contact pads used for wire bonding were 200×200 μm^2 to allow several attempts to bond a device, should the first fail. These design parameters were selected to achieve the desired SAW frequencies and ensure the proper functioning of the SAW devices in the experimental setup.

The bandwidth of the SAW device can be determined using Equation 2.33. By decreasing the number of electrodes, the bandwidth can be increased, while adding more electrodes results in a reduced bandwidth. However, it is important to note that reducing the number of IDT electrodes also leads to a decrease in the wave amplitude. Therefore, a trade-off needs to be considered between SAW amplitude and bandwidth.

3 Methods

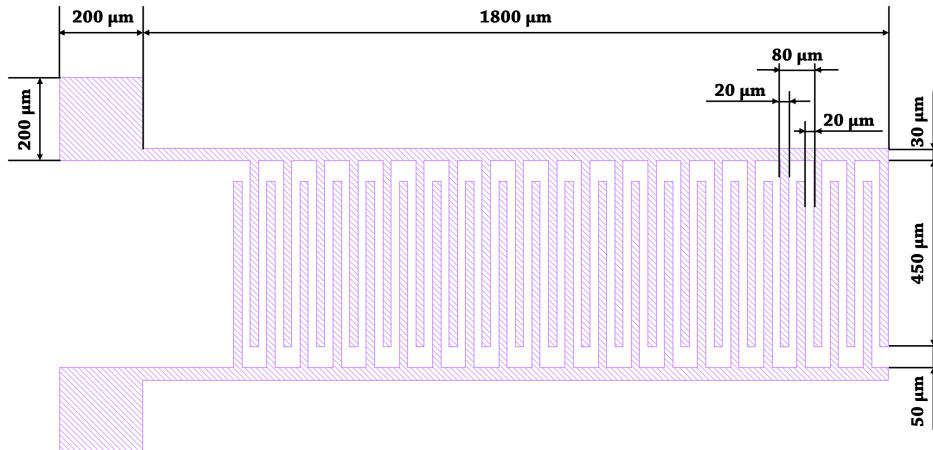


Figure 3.6: Example of the IDT geometry used to generate SAWs with a frequency of ~ 50 MHz. The centre frequency of the SAW depends on the widths of the electrodes, spacing between neighbouring electrodes, and the SAW propagating velocity. With electrode widths and spacing set to $20 \mu\text{m}$, the resulting SAW centre frequency is ~ 50 MHz. The IDTs feature an aperture of $500 \mu\text{m}$, contact pad sizes of $200 \times 200 \mu\text{m}^2$, and a total of 20 electrodes.

In this study, a configuration with 20 electrodes was chosen, achieving a bandwidth of 10% of the centre frequency, ensuring a balance between amplitude of the SAWs obtained and a sufficiently wide bandwidth.

Device layout

The devices described in Chapter 4 and Chapter 5 share a common design layout, as shown in Figure 3.7. Both devices feature two IDTs positioned opposing each other. This design was chosen because it allows for the investigation of the effects of travelling and standing SAWs on the magnetic properties of thin films. Specifically,

3.4 Surface acoustic wave device

travelling SAWs can be generated by one set of IDTs and subsequently detected by the opposite set. Moreover, the design permits the concurrent excitation of SAWs from both IDTs, leading to the formation of standing SAWs within the delay line. In this configuration, the gap between the two IDTs, which forms the delay line, was designed to be 3 mm. This spacing was chosen to accommodate the deposition of a 2-mm-wide magnetic thin film in between the IDTs. Further specifics about the device layout and the experimental setup are provided in the relevant chapters.

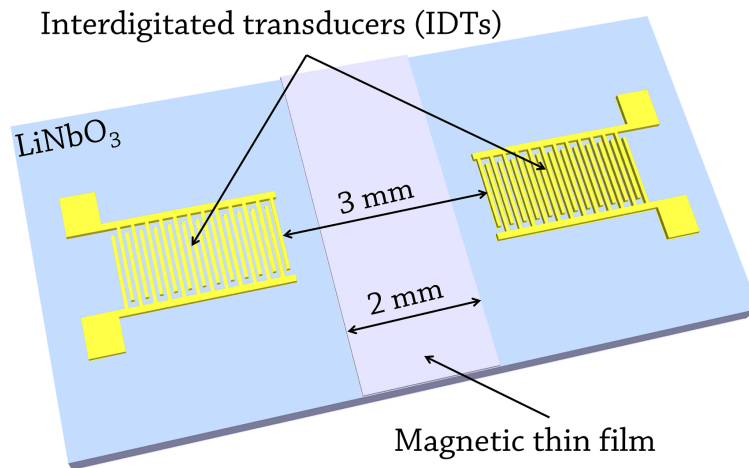


Figure 3.7: Layout of a SAW device (not to scale). A 2-mm wide magnetic thin film is deposited onto a LiNbO_3 substrate. One pair of IDTs is fabricated on both ends of the thin film with a spacing of 3 mm.

3.4.2 Device fabrication

High-quality electrodes for the SAW devices were fabricated using standard cleanroom maskless photolithography techniques. Traditionally, photolithography involves defining a photoresist pattern on a substrate by exposing the photoresist to high-intensity

3 Methods

ultraviolet (UV) light through an optical mask with the desired pattern, followed by developing away the exposed photoresist. In this work, a maskless aligner (MLA) was employed, allowing patterns to be directly written onto the photoresist without the use of an optical mask. This approach eliminates the need for a physical mask while providing more flexibility in pattern design. The general procedure used is as follows:

- i. Design of the patterns for the magnetic thin film and IDTs to the required pattern using commercial KLayout software [109].
- ii. Perform photolithography to transfer the designed patterns onto the substrate prior to the deposition of magnetic thin films using dcMS.
- iii. Deposition of the magnetic thin films.
- iv. Use a lift-off process to remove the excess undesired metal on top of the photoresist layers.
- v. Repeat the photolithography process to define the patterns for the electrical connections and IDTs.
- vi. Pattern the electrical connections and IDTs using thermal evaporation technique, followed by the metal lift-off process to remove the excess metal.

The workflow of the photolithography process is illustrated in Figure 3.8. Further details of the process are discussed in the following section.

Sample preparation

The LiNbO_3 wafer was firstly diced into the desired sizes using a wafer saw. The diced substrates were then subjected to agitation in acetone and isopropanol for 5 minutes each, followed by rinsing in deionised water to clean them. After rinsing, the samples were dried using a stream of nitrogen gas. Next, a layer of MicroChem

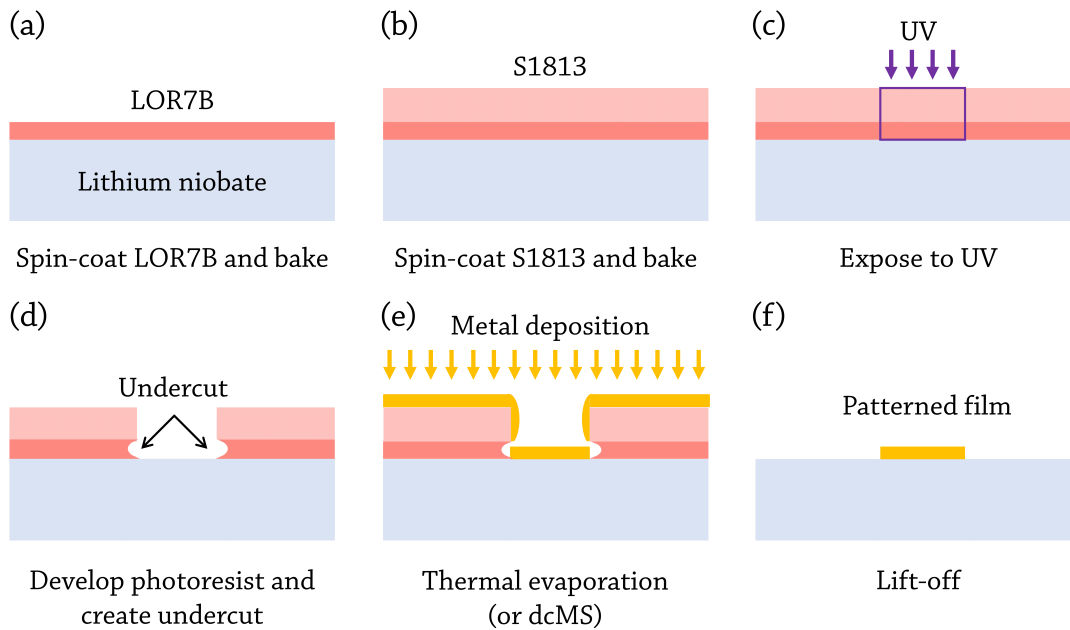


Figure 3.8: Illustration of the photolithography process. (a) A layer of LOR7B is spin-coated and baked onto the LiNbO_3 substrate. (b) Another layer of S1813 is spin-coated and baked on top of the LOR7B layer. (c) The sample is exposed to UV light, forming the desired patterns. (d) The sample is immersed in a developer solution, removing the exposed photoresist and creating an undercut (LOR7B develops isotropically). (e) Magnetic thin films are deposited using dcMS, or electrical connections and IDTs are deposited using the thermal evaporation technique. (f) The bi-layer photoresist and the metal layer above are lifted off by immersion in acetone, which removes all the resist and the metal layer on top of unexposed regions, leaving only the film patterned with the desired geometry in the region of interest.

3 Methods

LOR7B was spin-coated onto the substrate at a spin speed of 6000 rpm for 45 seconds. The coated sample was then baked at 165°C for 3 minutes, as shown in Figure 3.8a. Subsequently, another layer of Microposit S1813 positive photoresist was spin-coated onto the baked sample at a spin speed of 4000 rpm for 45 seconds. This was followed by a 2-minute baking at 110°C, as depicted in Figure 3.8b. The resulting thicknesses of the LOR7B layer and S1813 layer were approximately 0.5 µm and 1.4 µm, respectively. This bilayer process was used to improve undercut of the resist and subsequent lift-off of excess metal outside the patterned region.

Forming patterns on photoresist

The maskless aligner (Heidelberg MLA150) is a lithography tool that allows direct writing of pattern onto a substrate without requiring a traditional optical mask. It utilises a technology based on the digital micro-mirror device (DMD) to project the patterns on to the photoresist layer. The workflow of the MLA is as follows:

- i. Import desired pattern that created by Klayout into MLA software.
- ii. The MLA is equipped with DMD chip, whose mirrors each correspond to one pixel on the pattern. These mirrors can be individually controlled to either reflect or block light.
- iii. Load samples into MLA.
- iv. The DMD precisely controls the exposure of specific areas on the photoresist, forming the desired patterns.
- v. Unload samples for further development and processing.

The samples were then immersed in Microposit 351 developer (in a ratio of 3 parts H₂O to 1 part Microposit 351) for 40 seconds, followed by rinsing in deionised water.

The bi-layer photoresist was used to create an undercut, resulting in thin films with smooth and uniform edges (Figure 3.8d).

Deposition of electrical connections and IDTs

After the defining patterns using the MLA, the LOR7B and S1813 photoresists together formed a mask on the substrate. Metal deposition then took place on the surface of the substrate through the mask. The metal was deposited over the entire substrate by thermal evaporation for IDTs and electrical contacts, or by dcMS for magnetic thin films (see Section 3.2.2). Gold electrodes (Au, thickness of ~ 90 nm), which are suitable for forming electrical connections, were used to pattern the IDTs and electrical contacts. A ~ 10 nm layer of titanium (Ti) was deposited prior to the Au layer to enhance the adhesion between the Au electrodes and the substrate.

In this work, a thermal evaporator (Edwards Auto 306) was used to deposit Ti/Au for the fabrication of IDTs and electrical connections. Figure 3.9 illustrates the diagram of the thermal evaporator. The substrates were mounted on a sample holder, which was positioned facing downwards towards the target materials (Ti and Au). The chamber was initially pumped down to achieve a base pressure of 1×10^{-6} Pa. The target materials, Ti and Au, were placed in separate tungsten boats within the evaporator chamber. To induce vaporisation, an electric current was passed through the tungsten boat, resulting in the heating of the target material. The required current ranges from 20 A to 30 A for Ti and 30 A to 40 A for Au. As the target material was heated, it evaporated and formed a vapor flux consisting of both individual atoms and clusters of atoms [110]. This vapor flux travelled towards the substrate and condenses on its surface. The deposition process was controlled by a shutter located between the target material and the substrate, which regulated the exposure of the substrates to the vapor flux [110]. The thickness of the deposited materials was monitored by measuring the frequency shift of a quartz crystal located near the substrates.

3 Methods

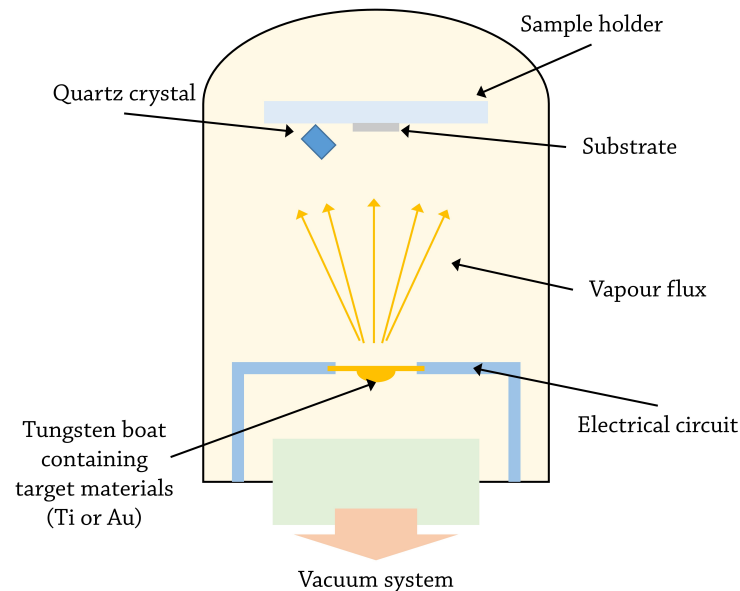


Figure 3.9: Diagram of the thermal evaporator. The substrates are mounted on a sample holder that is fixed at the upper part of the chamber. The base pressure of the chamber is pumped down to 1×10^{-6} Pa before performing the thermal evaporation. Electrical current is applied to the tungsten boat containing target material (Ti or Au) to generate vapour flux consisting of atoms and clusters of atoms. The vapour flux condenses on the surface of the substrates. A quartz crystal is used to monitor the thickness of the deposited metal. The figure has been reproduced from [110].

Lift-off

To form the IDTs and electrical connections, a technique called “lift-off” was employed after the metal deposition process. This technique involved the removal of undesired metal and the underlying photoresist (LOR7B and S1813) to leave behind the desired patterned metal structures. The lift-off process began by immersing the samples into acetone for 10 minutes, followed by immersion in developer for 2 minutes. In

some cases, if the metal and photoresist were not easily removable after the acetone immersion, the samples were gently agitated for 3 minutes to aid in the removal process. After the lift-off process, the samples were rinsed in isopropanol and deionised water, respectively, to eliminate any residual traces of solvent or impurities. Finally, the samples were dried using a nitrogen gas stream to ensure a clean and dry surface for further processing or characterisation.

3.4.3 Device characterisation

Design of the co-planar waveguide

A co-planar waveguide (CPW) is a transmission line configuration commonly used for guiding and propagating electromagnetic waves. It offers advantages over other waveguides including wider bandwidth, lower signal attenuation, and better isolation between the signal line and the ground planes [111]. The design of the CPW used in this study is illustrated in Figure 3.10. The SAW device was mounted in the centre of the CPW using double-sided tapes. Gold pads were fixed on the CPW using silver paint to ensure a reliable connection between the IDTs and the CPW. Wire bonding was employed to connect the IDTs to the ground and conducting planes of the CPW. SubMiniature version A (SMA) connectors were used to establish the connection between the CPW and the rf power source. The CPW was fabricated from a $2 \times 4 \text{ mm}^2$ Cu-epoxy PCB. The width of the conducting line was set to 2 mm, and the CPW designed using an rf circuit calculator to have an impedance of 50Ω , which indicated that the gap between the signal ground and the signal conductor needed to be 0.46 mm to obtain this value.

3 Methods

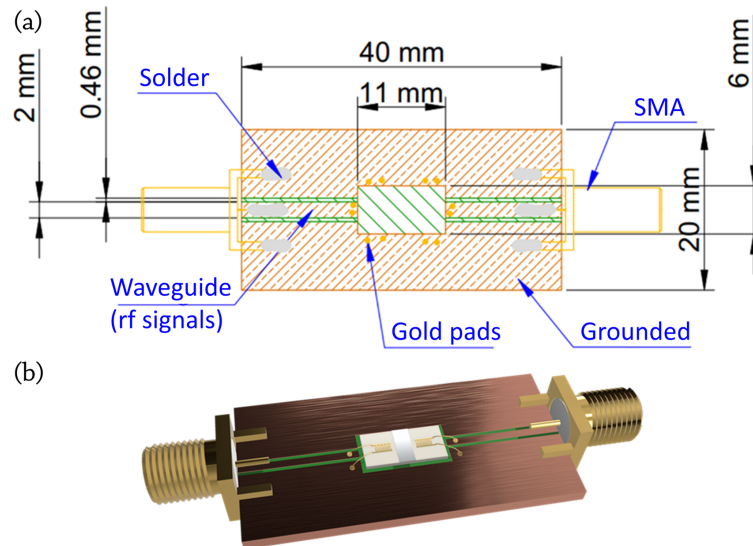


Figure 3.10: (a) Layout and (b) schematic diagram of the CPW used in this thesis. The CPW was designed with an impedance of 50Ω and features two SMA connectors for connections to the VNA to be made. The SAW device was fixed on the CPW using a double-sided tape. Gold pads were positioned on the CPW using silver paint to establish reliable connections. A wedge wire-bonder was employed to establish connections between the IDTs and the gold pads.

Scattering parameter measurements

Scattering parameters (S-parameters) were used to characterise the electrical behaviour of linear networks when stimulated by electrical signals [79]. In this study, the frequency response of the IDT was measured using S-parameters obtained from a VNA. A two-IDT system, as shown in Figure 3.11, allows the measurement of four S-parameters: S_{11} , S_{22} , S_{21} , and S_{12} . S_{11} ($S_{11} = b_1/a_1$) and S_{22} ($S_{22} = b_2/a_2$) represent the power reflected at port 1 and port 2, respectively, and are commonly referred to as reflection coefficients. The transmission coefficients, S_{21} ($S_{21} = b_2/a_1$) and S_{12} ($S_{12} = b_1/a_2$), measure the power transmitted from port 1 to port 2 and

from port 2 to port 1, respectively. S-parameters are typically expressed in decibels (dB), given by the equation:

$$A_{ij} = 20 \log(S_{ij}), \quad (3.2)$$

where i and j can be either 1 or 2.

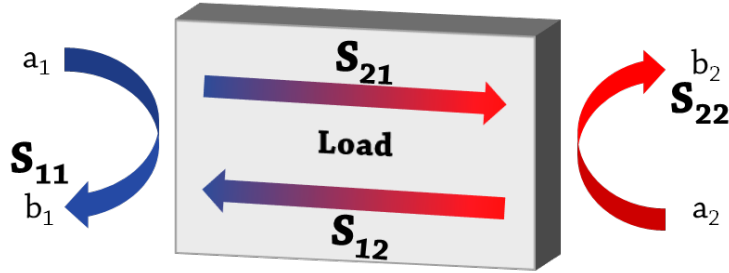


Figure 3.11: Schematic representation of the S-parameters in a two-port system.

Circuit for S-parameter measurements

Figure 3.12 illustrates the circuit setup employed to measure the S-parameters of the IDTs. Two IDTs were connected to the ports of a VNA (Agilent E5062A) via a CPW using SMA connectors. One port of the VNA was used to apply rf signals, while the other port was used to detect the transmitted signals. The inset graph in Figure 3.12 presents an example of the S-parameters obtained from the IDTs in this study. The centre frequency is determined as the frequency at which the transmission coefficient is maximal and the reflection coefficient is at minimal.

3.5 Micromagnetic simulations

Micromagnetic simulations were conducted using Mumax3 throughout this thesis to investigate how SAWs influence magnetisation dynamics of the thin films [112]. Mumax3 integrates numerically the LLG equation (Equation 2.3). By modelling the in-

3 Methods

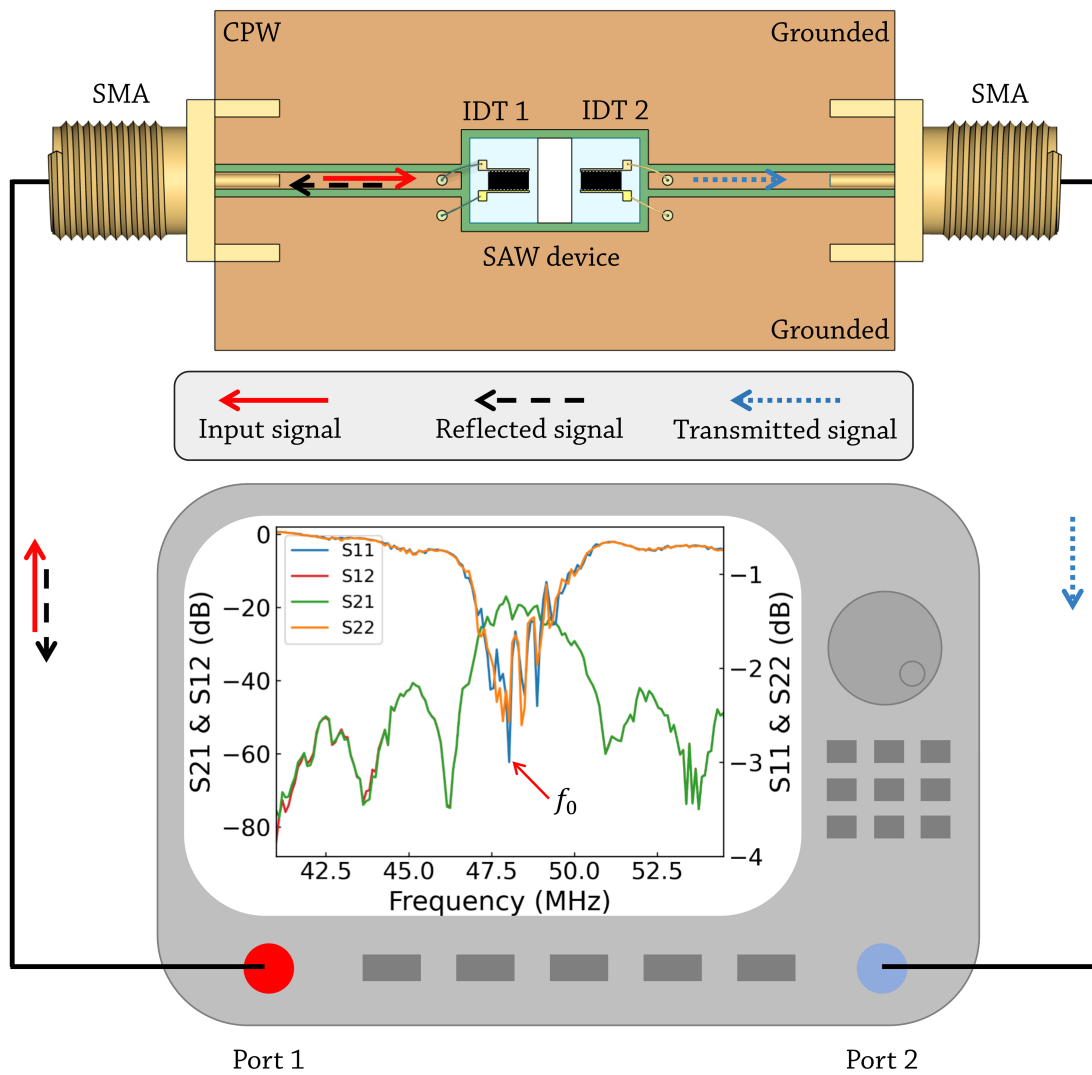


Figure 3.12: Schematic of the rf circuit used to characterise S-parameters. The inset graph shows an example of the typical S-parameters of the IDTs used in this study.

3.5 Micromagnetic simulations

interactions between the SAWs and the magnetic thin films at the microscopic level, the simulations offer insights into the underlying physical mechanisms and help elucidate the observed experimental phenomena. This combined experimental and theoretical approach enhances our overall understanding of the SAW-induced magnetisation dynamics and thus contributes to a more comprehensive understanding of the system.

SAWs were implemented by the Mumax3 built-in strain tensor using spatial and time profiles [113]. It should be noted that the film is considered acoustically thin, meaning that it is sufficiently thin and rigid for the chosen SAW frequency in this study. The entire film moves synchronously with the substrate surface, where the in-plane gradients are predominant compared to those normal to the surface, leading to a consistent displacement throughout the film thickness [79, 114]. Therefore, only in-plane strain (ϵ_{xx}) was taken into consideration, and B_2 in Equation 2.17 was set to zero in this thesis.

Figure 3.13 depicts a typical example of the spatial profile of strain for both standing and travelling SAWs. The blue and red stripes in the figure indicate the anti-nodes of the SAWs, representing regions with maximum (compressive) and minimum (tensile) strain, respectively. The white regions between the blue and red stripes signify the nodes, where the strain is minimal.

The ϵ_{xx} of standing SAWs was implemented as follows

$$\epsilon_{xx} = \sin(kx) \cos(\omega t), \quad (3.3)$$

where k and ω are the wavenumber, angular frequency of the standing SAW, respectively, and t is time.

Similarly, the ϵ_{xx} of travelling SAW was implemented as follows

$$\epsilon_{xx} = \sin(\omega t) \cos(kx) - \cos(\omega t) \sin(kx), \quad (3.4)$$

3 Methods

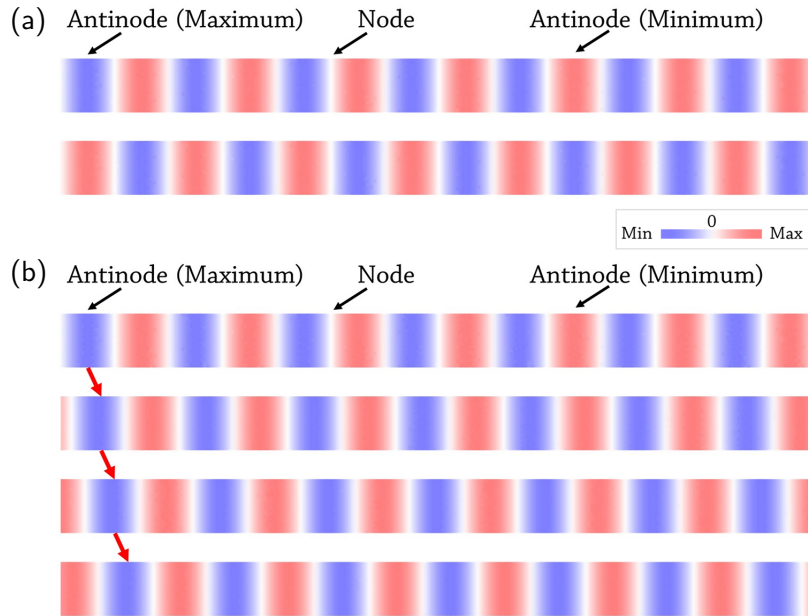


Figure 3.13: Example of (a) standing and (b) travelling (b) SAWs implemented using Mumax3.

where k and ω are the wavenumber, angular frequency of the travelling SAW, respectively, and t is time. Detailed information regarding the material parameters used and the simulation procedures can be found in the respective chapters.

3.6 Summary

This chapter presented an overview of the methods and techniques employed for the design, fabrication, and characterisation of magnetic thin films and SAW devices. The magnetic thin films were deposited using dcMS, and their deposition rates calibrated using XRR. The magnetic properties of the thin films, such as hysteresis loops and domain patterns, were examined using Kerr microscopy, which allows for the visualisation and analysis of magnetisation behaviour. SAW devices, which consisted of IDTs

and magnetic thin films, were designed, fabricated, and characterised to investigate the influence of SAWs on the magnetic properties. The IDTs were prepared through standard photolithography techniques, and their S-parameters were measured using a VNA, which provided valuable information about the electrical behaviour and performance of the IDTs. To gain further insights into the magnetisation dynamics induced by SAWs, micromagnetic simulations were performed using the Mumax3 software. These simulations enabled a detailed investigation of the SAW effects on the magnetisation dynamics of the thin films, providing valuable theoretical predictions that completing the experimental measurements. The subsequent chapters of this thesis detail specific aspects of these experimental measurements and simulations, together providing an improved understanding of the SAW-induced magnetisation dynamics in the magnetic thin films.

3 Methods

CHAPTER 4

Local magnetic anisotropy control

4.1 Introduction

Materials with strong PMA are promising candidates for future generations of data storage and processing devices owing to their stable magnetisation states and narrow DWs [4, 30, 115, 116]. These features confer the stability of the stored information while providing a high storage density [6]. However, unfortunately materials with strong PMA typically also require a large current to reverse the magnetisation or to move DWs in order to write or transfer data. This high current can lead to energy wastage and Joule heating, imposing limitations on the packing density of practical devices [40, 41]. There is thus much interest in reducing the energy required to manipulate DWs.

SAW-induced coercivity modification and DW motion show significant potential for energy-efficient information storage and data processing devices, since the magnetisation switching is driven by voltage instead of current. However, the SAW-induced magnetisation switching mechanism of thin films with PMA remains unclear, and especially the role of the nodes and anti-nodes of the standing SAW in the magnetisation reversal process. The correlation between the properties of SAWs and magnetisation changes also is uncertain.

In this chapter, we demonstrate local anisotropy control of a Ta/Pt/Co/Ir/Ta thin film with PMA by standing SAWs at a centre frequency of 93.35 MHz. In the presence of SAWs, the coercivity of the thin films decreases significantly, while the magnetisation reversal speed increases. These experimental results along with micromagnetic simulations reveal that the anti-nodes of the standing SAWs locally reduce the anisotropy of the Ta/Pt/Co/Ir/Ta thin film, which lowers the coercivity and favours magnetisation reversal. Existing literature, such as the work by Li *et al.*, has explored the effects of SAWs on magnetisation switching within thin films that exhibit in-plane magnetic anisotropy [64]. In this chapter, we will focus on the impact of the standing SAWs on the magnetic properties of thin films with PMA. The results of

this work were published as “*Local anisotropy control of Pt/Co/Ir thin film with perpendicular magnetic anisotropy by surface acoustic waves*”, *Applied Physics Letters*, 120, 252402 (2022) [11].

4.2 Experimental details

4.2.1 Magnetic thin film and SAW device

Figure 4.1 shows a schematic of the experimental arrangement. The device comprises a 2-mm-wide stripe of Ta(5.0 nm)/Pt(2.5 nm)/Co(1.1 nm)/Ir(1.5 nm)/Ta(5.0 nm) thin film with PMA, which was prepared by dcMS on a 128° Y-cut LiNbO₃ substrate. As shown in Figure 4.1b, one pair of Ti(10 nm)/Au(90 nm) IDTs, each consisting of 20 pairs of electrodes, was patterned using optical lithography (exposure of the resist was achieved using a MLA, with subsequent metal evaporation and lift-off forming the IDTs as mentioned in Section 3.4.2). The aperture of the IDTs and the SAW propagation distance were designed to be 500 μm and 3 mm, respectively. The electrode width and spacing were both set at 10 μm.

4.2.2 SAW circuit and S-parameters

S-parameters of the IDTs were measured using the method mentioned in Section 3.4.3, allowing the peak value of transmission as a function of frequency to be determined, at which point SAWs are generated most strongly (this point typically showing 11 dB transmission loss at 93.35 MHz, as shown in Figure 4.2). The total loss associated three factors: (i) cabling, (ii) transduction at the IDT (expected to be the largest factor given no impedance matching was used) and (iii) SAW propagation to the centre of the device, together introduces $11 \text{ dB}/2 = 5.5 \text{ dB}$ total loss from each port to the centre of the (symmetric) device. The VNA output was then connected to the

4 Local magnetic anisotropy control

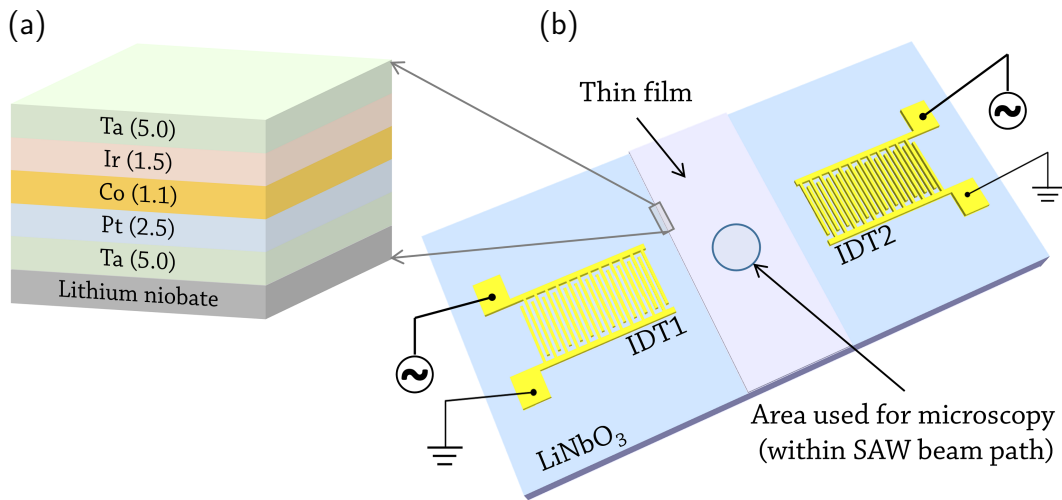


Figure 4.1: (a) Thin film structure: Ta(5.0 nm)/Pt(2.5 nm)/Co(1.1 nm)/Ir(1.5 nm)/Ta(5.0 nm). (b) Schematic of experimental arrangement (not to scale). The 2-mm-wide thin film was deposited onto the LiNbO₃ substrate. IDTs were patterned on each side of the thin film to launch the SAWs.

device as shown in Figure 4.3. An attenuator (10 dB, Mini-Circuit BW-S10W2+) was connected between the signal generator and the amplifier (gain 33 dB, Mini-Circuits ZHL-2-8-S+) to ensure the applied rf power does not exceed specifications of the amplifier.

To generate standing SAWs, a power splitter (Mini-Circuit ZAPD-30-S+) was used to divide the signal from the VNA output port into two, which each of the resulting signals then sent to one IDT. The power from the VNA was varied from 0 to 5 dBm. This power was reduced down to -10 to -5 dBm by an attenuator to ensure the output was kept inside the linear range of the amplifier. The final signal applied rf power was thus amplified to between 23 to 28 dBm before being split using the 3 dB splitter (with each IDT thus receiving ~20 dBm to ~25 dBm). Taking into account the measured losses at peak transmission, the expected total rf power transduced into

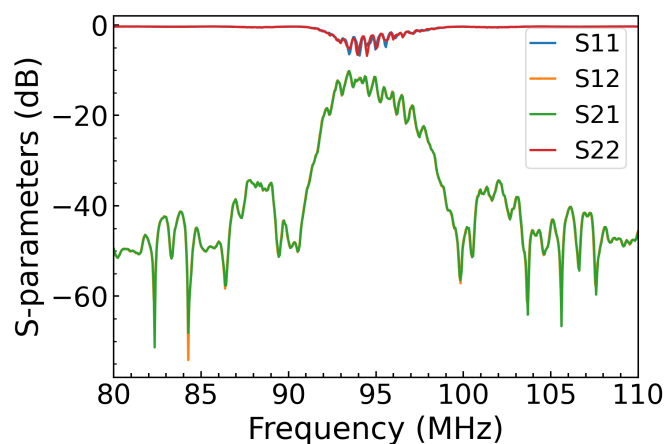


Figure 4.2: S-parameters of the IDTs. The delay line comprising both IDTs and the substrate shows a centre frequency of 93.35 MHz, and 3 dB bandwidth of 9.34 MHz.

the standing SAW mode was in the range ~ 17.5 to ~ 22.5 dBm. Figure 4.2 shows the reflection (S11 and S22) and transmission (S21 and S12) characteristics of the SAW transducers and substrate showing a centre frequency of 93.35 MHz, yielding a wavelength of 42.667 ± 0.004 μm . The VNA used in our study had a frequency accuracy of 5 ppm, and the propagating velocity of the SAW on LiNbO₃ is known to be 3982 m/s [103].

4.2.3 Determination of magnetisation reversal speed

To determine the magnetisation reversal speed, we employed Kerr microscopy using the following procedure:

- i. We first saturated the sample with a 50 mT out-of-plane field. After turning off the field, an initial image was captured to assess background noise, as illustrated in Figure 4.4a.
- ii. We then applied a pulsed field in the opposite direction (ranging from -2 to -3.2 mT). This was done to nucleate domains and promote DW motion, both

4 Local magnetic anisotropy control

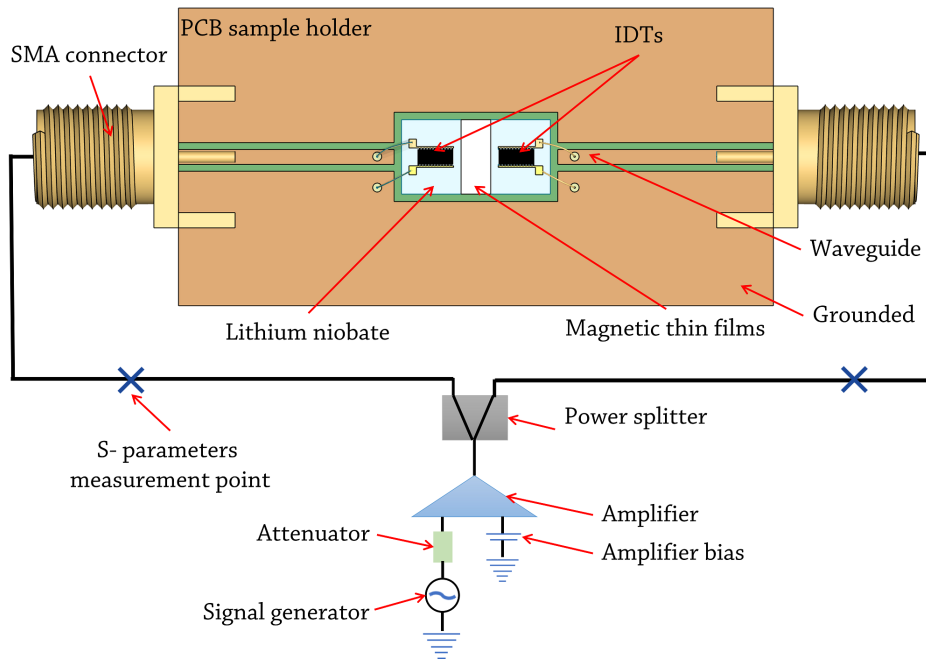


Figure 4.3: Schematic of the rf circuit for generating standing SAWs. For S-parameter measurements, the signal generator, attenuator, amplifier, and power splitter were removed, and a VNA was connected at the “X” points.

with the SAW turned on and SAW off (SAW modal power varied between 17.5 to 22.5 dBm). Subsequently, we captured a second image representing the final state, as seen in Figure 4.4b.

- iii. Both images were converted into binary values, as depicted in Figure 4.4c and d. In these binary representations, magnetisation pointing “up” was denoted by white pixels, while “down” was denoted by black pixels.
- iv. We determined the number of black pixels in the initial and final images as P_0 and P_1 , respectively. The difference between P_0 and P_1 represented reversed magnetisation.

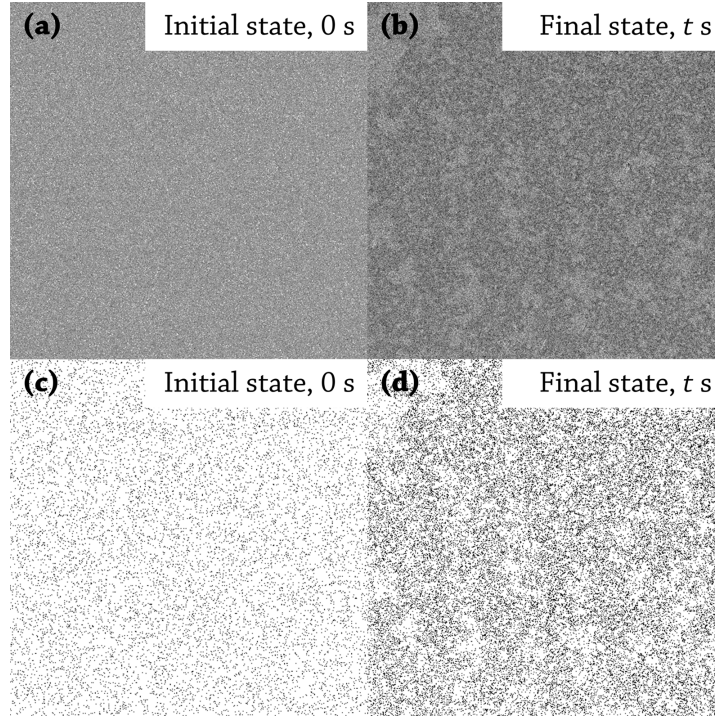


Figure 4.4: Determining magnetisation reversal speed in the Ta/Pt/Co/Ir/Ta thin film using Kerr microscopy: (a) Original image of the initial state (background noise) at 0 mT; (b) Final state after the application of a pulse magnetic field and SAW; (c) Binary representation corresponding to (a); (d) Binary representation corresponding to (b).

Thus, we expressed the magnetisation reversal speed as

$$S_{\text{mag}} = \frac{(P_1 - P_0)\phi_0}{t_p}, \quad (4.1)$$

where ϕ_0 signifies the area per pixel ($0.07 \mu\text{m}^2/\text{pixel}$ for $50\times$ lens), and t_p represents the pulse width of the field, set at 5 s. We used an image size of $500 \times 500 \text{ pixel}^2$ (equivalent to $132 \times 132 \mu\text{m}^2$) to determine the magnetisation reversal speed. It is important to note that since we assessed the background noise on a global scale, our

4 Local magnetic anisotropy control

estimations for the magnetisation reversal speed might be underestimated.

4.2.4 Computational details

Micromagnetic simulations were performed using Mumax3, based on the LLG equation (Equation 2.3) [112]. The magnetoelastic energy density of the system can be described as Equation 2.17. The material parameters were set as follows [65]: saturation magnetisation $M_s = 6.0 \times 10^5$ A/m, exchange constant $A_{\text{exch}} = 1.0 \times 10^{-11}$ J/m, PMA $K_u = 8.0 \times 10^5$ J/m³, and magnetoelastic coupling coefficient $B_1 = 1.0 \times 10^7$ J/m³. This B_1 value is taken from [65], which is closed to the experimental observation as reported in [117] (1.5×10^7 J/m³ to 3.5×10^7 J/m³). A computational region of dimensions $500 \times 200 \times 1$ nm³ with a mesh size of $2 \times 2 \times 1$ nm³ was used (as shown in Figure 4.5).

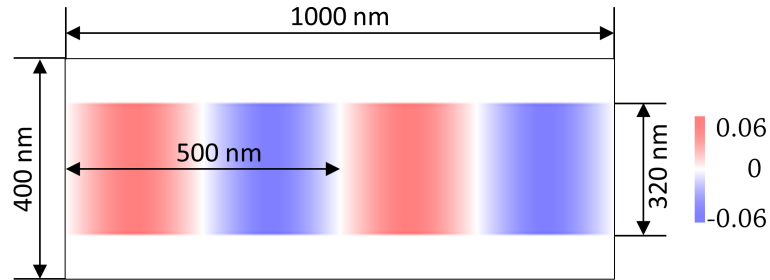


Figure 4.5: Configuration of the micromagnetic simulations. The entire dimension of the simulation is $400 \times 1000 \times 1$ nm³, with a SAW beam path with a width of 320 nm. The chosen wavelength of the SAW is 500 nm. The amplitude (strain) of the SAW is 0.06.

The chosen mesh size is smaller than the exchange length, which defines the scale at which the atomic-level exchange interactions become more prominent than the typical magnetostatic fields. The exchange length, l_{exch} , is given by $l_{\text{exch}} = \sqrt{A_{\text{exch}}/K_u}$, resulting in an exchange length of 3.5 nm in our simulations. The velocity of the

SAW was set to 4000 m/s [103]. For the simulation, the wavelength of the SAW was set as 500 nm owing to the limitations of computing capacity [13, 19, 65]. It should be noted that the material parameters and SAW characteristics differ from those explored in experimental studies, therefore, the findings should be carefully interpreted. Standing SAWs were implemented using Equation 3.3 in the central part of the computational region representing the beam path of the SAW with a width of 320 nm (the total width is 400 nm).

4.3 Results and discussion

4.3.1 Reduced coercivity

Figure 4.6a shows the hysteresis loops of the thin films for different applied rf power from 17.5 to 22.5 dBm (at 93.35 MHz), and also without a SAW. The sharp switching of the magnetisation indicates a strong PMA of the Co layer. The presence of the curved corners is because a higher (than coercivity) field is required to squeeze out the homochiral DWs to saturate the thin film [118].

Significant coercivity reduction is observed in the presence of the standing SAW: The coercivity decreases with increasing applied rf power from 4.46 ± 0.04 mT at 17.5 dBm to 3.80 ± 0.02 mT at 22.5 dBm (Figure 4.6b and c). As shown in Figure 4.7, the coercivity is thus up to $\sim 21\%$ reduced compared to that measured without SAW (4.80 ± 0.03 mT). The coercivity reduction can be explained by the strain-induced changes of the PMA [53]. The SAWs act as time-varying strain waves, which can locally change the energy landscape of the thin films, periodically raising and lowering the anisotropy of the thin film. The magnetisation reverses when the anisotropy is at low values. Owing to the nature of the magnetisation reversal process, the magnetisation is not reversible even when the anisotropy is at the highest value. The anisotropy changes increase with the increasing applied rf powers.

4 Local magnetic anisotropy control

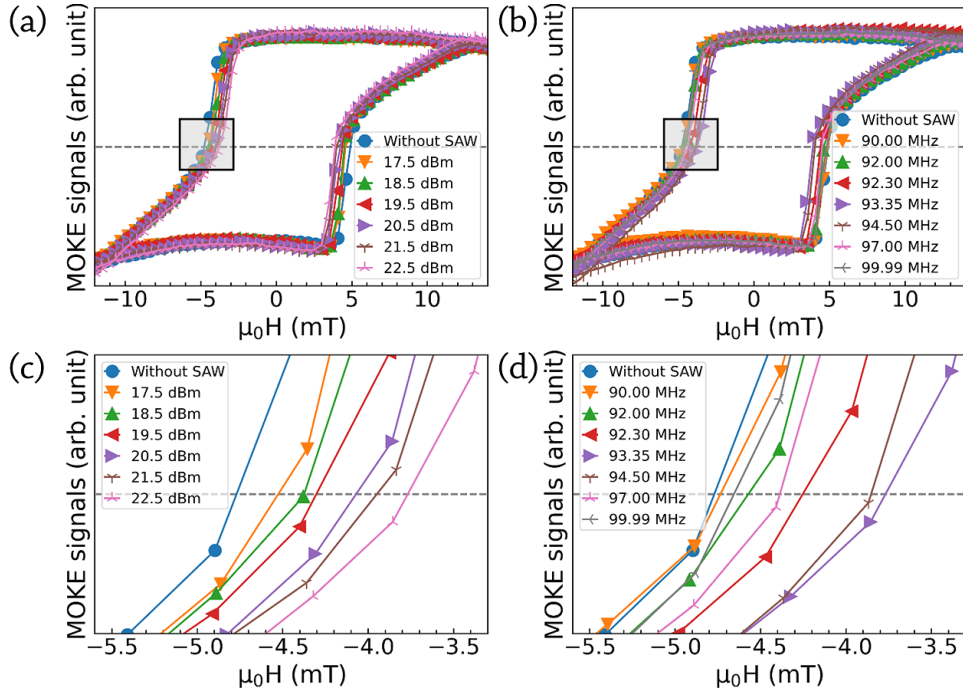


Figure 4.6: Hysteresis loops of the Ta/Pt/Co/Ir/Ta thin film as a function of the (a) applied rf power and (b) frequency. (c) and (d) are the enlarged views of the framed areas in (a) and (b), respectively. Lines are the guide to the eye.

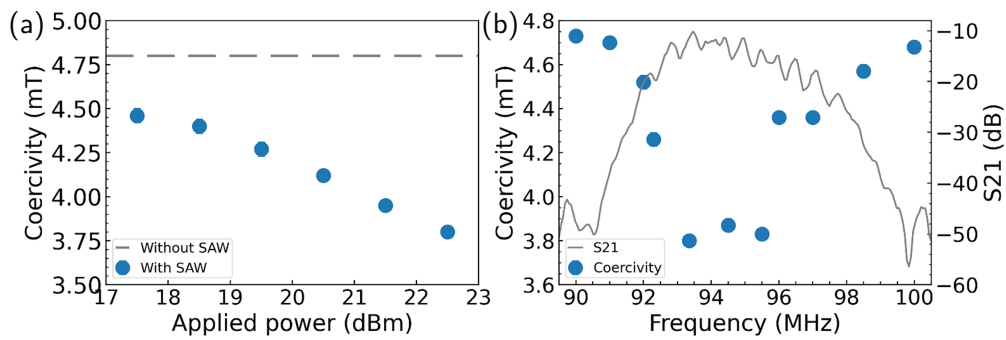


Figure 4.7: Coercivity of the Ta/Pt/Co/Ir/Ta thin film as a function of the (a) applied rf power and (b) frequency. S21 is also displayed in (b). Error bars are smaller than the data points.

4.3.2 Enhanced magnetisation reversal speed

Figure 4.8a to c show the influence of the external field, applied rf power and frequency of the SAW on the magnetisation reversal speed, respectively. As shown in Figure 4.8a, with the external magnetic field increasing from 2.0 to 3.2 mT, the change in the magnetisation reversal speed without SAW is very limited (from $71 \pm 5 \mu\text{m}^2/\text{s}$ to $168 \pm 3 \mu\text{m}^2/\text{s}$), whereas in the presence of the standing SAW, the magnetisation reversal speed increases from $250 \pm 20 \mu\text{m}^2/\text{s}$ at 2.0 mT to $2100 \pm 80 \mu\text{m}^2/\text{s}$ at 3.2 mT, which is a $\sim 740\%$ increase. The magnetisation reversal speed is increased eleven-fold at 3.2 mT in the presence of SAW compared to that with magnetic field only. The implication is that the standing SAW can significantly lower the required switching field and accelerate the magnetisation reversal. At 93.35 MHz, the magnetisation reversal speed gradually increases with the increasing applied rf power from $310 \pm 30 \mu\text{m}^2/\text{s}$ at 17.5 dBm to $2100 \pm 80 \mu\text{m}^2/\text{s}$ at 22.5 dBm with a 3.2 mT field (see Figure 4.8b).

Similar to the effect of frequency on the coercivity reduction, the magnetisation reversal speed increases when the frequency approaches the centre frequency, achieving its maximum value near the centre frequency (as shown in Figure 4.8c). We note the S21 response is asymmetric and biased towards better transduction at lower frequencies, resulting in the biased magnetisation reversal speed responding to the source frequency. The change of the magnetisation reversal speed is caused by two main factors. Firstly, the presence of the standing SAW significantly reduces the domain nucleation field owing to the magnetoelastic coupling effect (see Figure 4.6a). The DW energy density can be expressed as: $\gamma_{\text{DW}} = 4\sqrt{A_{\text{exch}}K_{\text{eff}}}$, where A_{exch} is the exchange stiffness and K_{eff} is the effective anisotropy. Meanwhile, the SAW smooths the energy landscape of the thin film, accelerating the DW velocity. SAWs locally and periodically modifying the anisotropy and the energy potential of the thin film, which benefits the DW nucleation and motion [53].

4 Local magnetic anisotropy control

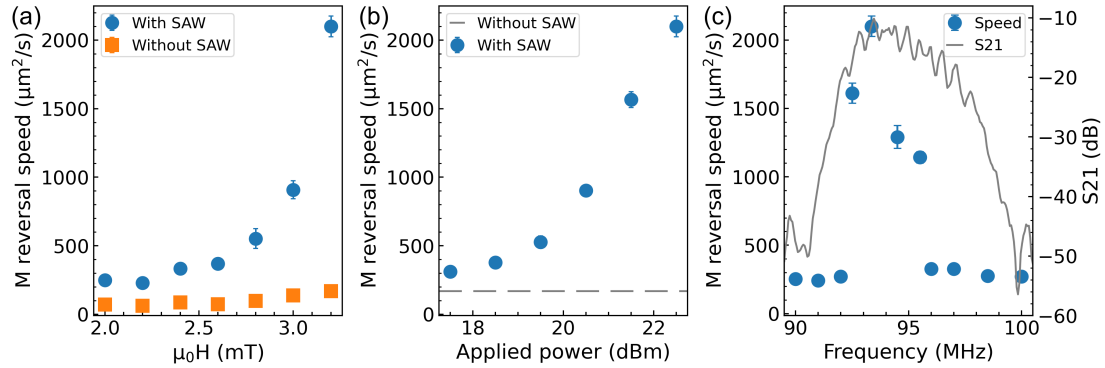


Figure 4.8: Magnetisation reversal speed of the Ta/Pt/Co/Ir/Ta thin film as a function of the (a) external magnetic field, (b) applied rf power and (c) frequency of the standing SAW. The applied rf power and frequency of SAW in (a) are 22.5 dBm and 93.35 MHz, respectively. The external field and frequency of SAW in (b) are 3.2 mT and 93.35 MHz, respectively. The external field and applied rf power of SAW in (c) are 3.2 mT and 22.5 dBm, respectively.

4.3.3 Standing SAW-induced stripe domain patterns

Figure 4.9a and b show domain patterns with both SAW off and SAW on obtained using Kerr microscopy, respectively. A 50 mT out-of-plane magnetic field was first applied to the sample to saturate the magnetisation in the “up” direction. A 4.6 mT field was then applied in the opposite direction. A large number of small branch domains nucleated and propagated randomly in the thin film without the SAW (see Figure 4.9a). With application of standing SAWs, the required domain nucleation field was much lower (around 3.6 mT for an applied rf power of 22.5 dBm at the centre frequency of 93.35 MHz). The domains tended to nucleate in certain parts of the thin film and lined up forming a clear stripe pattern (as shown in Figure 4.9b). The alignment of the domain patterns only occurred within the SAW beam path, with a random distribution of domains observed outside of the beam path (Figure 4.9c).

4.3 Results and discussion

This result itself indicates very strongly that the standing SAWs are responsible for the domain patterns. Figure 4.10e is cropped from Figure 4.9b.

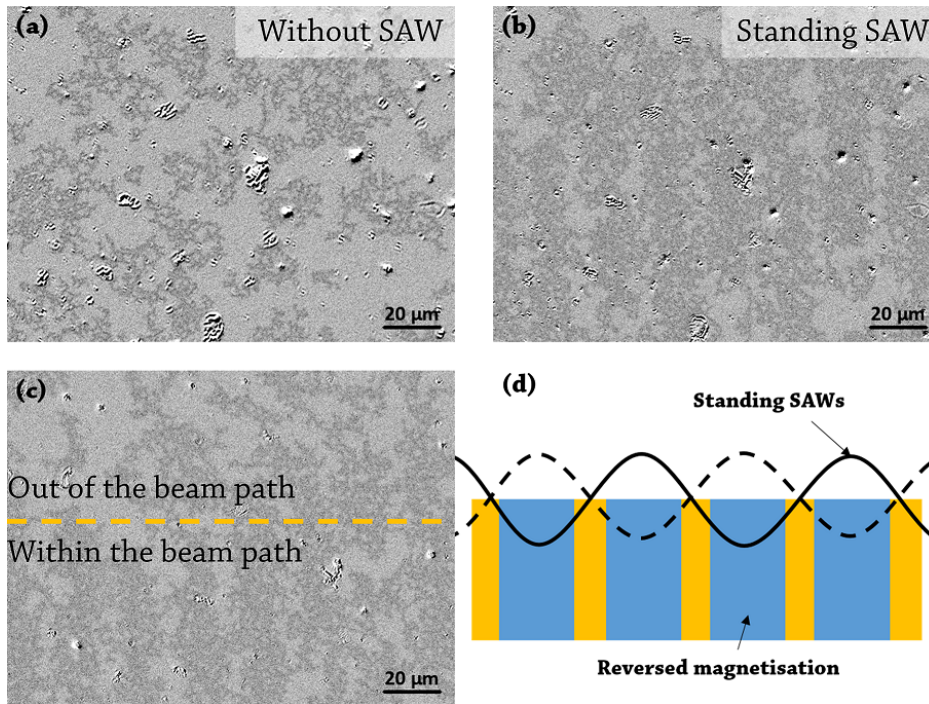


Figure 4.9: Domain patterns in the Ta/Pt/Co/Ir/Ta thin film. (a) Domain patterns randomly distributed obtained with only magnetic field, (b) stripe domain patterns with both magnetic field and standing SAW, (c) domain patterns at the boundary of the beam path, and (d) schematic of the standing SAW-assisted magnetisation reversal.

By converting Figure 4.10a into binary values (Figure 4.10b) and counting the number of the black pixels, we plotted the distribution of the domains (see Figure 4.10c). The experimental data was fitted by a sinusoidal function. The fit shows that the spacing between the lines is $20.88 \pm 0.06 \mu\text{m}$, corresponding well to the nominal half-wavelength ($\sim 21.33 \mu\text{m}$) spacing expected of the standing SAW. This is because the magnetoelastic coupling effect is the strongest at anti-nodes of the standing SAW,

4 Local magnetic anisotropy control

where the surface deflection is largest, and where the local lowering the anisotropy is expected to be the greatest. The effect is expected to be the weakest at the nodes of the standing SAW (as depicted in Figure 4.9d).

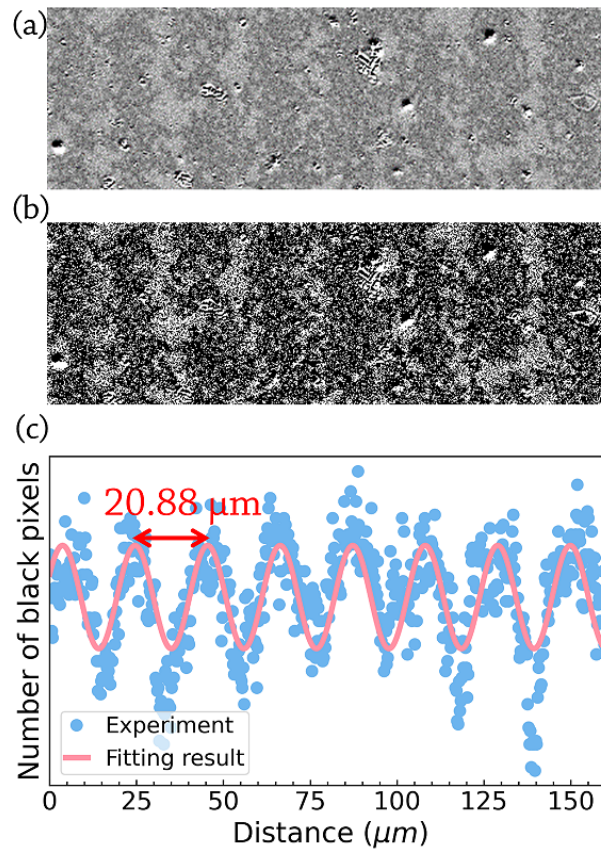


Figure 4.10: Analysis of the strip domain pattern in the Ta/Pt/Co/Ir/Ta thin film upon application of standing SAWs. (a) Cropped image from Figure 4.9b, (b) is (a) in binary value, (c) the number of black pixels in (b) and its sinusoidal fitting. The fitting results show a wavelength of $\sim 20.88 \mu\text{m}$, which is very close to the half-wavelength of the standing SAW ($\sim 21 \mu\text{m}$).

4.3.4 Magnetisation dynamics under standing SAWs

To further understand the effect of the nodes and anti-nodes of the standing SAW on the magnetisation reversal process, we performed micromagnetic simulations using Mumax3 with a built-in strain tensor [112]. As shown in Figure 4.11a, the red, white and blue indicate strains with maximum, zero, and minimum values, respectively. The system is firstly relaxed with magnetisation pointing “down” (see Figure 4.11b). Standing SAWs ($\epsilon_{\max} = 0.06$) together with external magnetic field (300 mT) pointing “up” are then applied. As shown in Figure 4.11c, at 1.5 ns, domains begin nucleating at the anti-nodes of the standing SAW. Then, the domains continue nucleating and propagating from anti-nodes to nodes until the domains merge with each other (Figure 4.11d and e), followed by domain propagation out of the beam path (Figure 4.11f). The simulation results agree qualitatively with our experiments and in particular our assumption that the anti-nodes of the standing SAW favour the nucleation of the domains and the propagation of the DWs. The simulation and magnetisation reversal speed results also reveal that standing SAWs lower the coercivity of the thin films by lowering local domain nucleation field and accelerating DW propagation.

4 Local magnetic anisotropy control

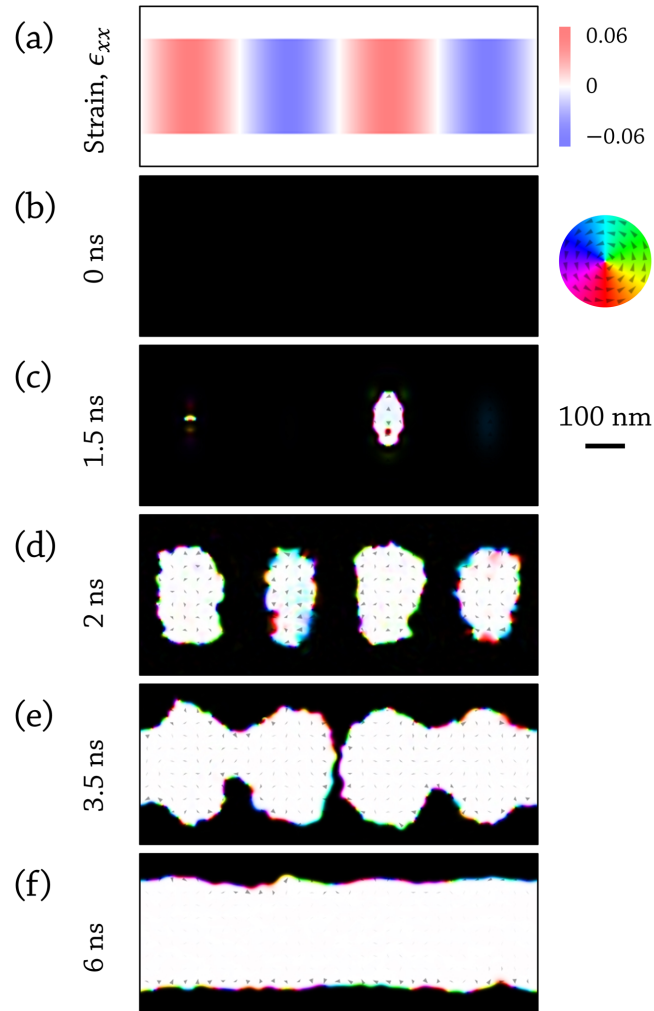


Figure 4.11: Simulation of magnetisation reversal process. (a) Spatial strain profile, (b) to (f) magnetisation at 0, 1.5, 2, 3.5 and 6 ns after applying field and standing SAW. The black and white colours in (b) to (f) represent magnetisation pointing “down” and “up”, respectively. The colour code for the in-plane magnetisation component is shown by a colour wheel.

4.4 Summary

To summarise, in this chapter, a strong coercivity reduction (up to $\sim 21\%$) was observed for the Ta/Pt/Co/Ir/Ta thin film with PMA upon application of 93.35 MHz standing SAWs. Owing to the SAW-induced magnetoelastic coupling effect, the magnetisation reversal speed was significantly enhanced (by a factor of ~ 11). The experiments and Mumax simulations together indicated that, owing to the strain distribution difference, standing SAWs were able to lower the domain nucleation field locally at the anti-nodes of the standing SAW. Domains tended to nucleate and propagate from anti-nodes to nodes of the standing SAW, forming striped domain patterns with spacing the same as the half-wavelength of the standing SAW.

4 Local magnetic anisotropy control

CHAPTER 5

Separation of heating and strain effects

5.1 Introduction

The motion of the magnetic DWs in thin films with PMA shows potential for technological applications in spintronics, mediated by the magnetoelastic coupling effect. The dynamic strain waves that SAWs introduce create a dynamic energy landscape that can trigger the magnetisation precession [8–10], assist the magnetisation switching [11, 12], and enhance the DW motion [14–17, 71]. However, the applied rf power and the propagation of SAWs through a structure can also result in a global or local temperature increase in devices owing to either the dissipation of the rf power or by direct acoustothermal heating from the SAW [119–122]. These temperature increases can also contribute to the DW motion. The acoustothermal heating effect is often-discussed in the context of the interaction of SAWs with microfluidic systems [122–129]. For example, Wang *et al.* investigated SAW as a rapid and controllable acoustothermal microheater for both the sessile droplet and liquid within a polydimethylsiloxane microchamber [128]. On the other hand, Utko *et al.* found that rf heating effect (Joule heating) plays a more important role than SAW itself in a SAW-driven single-electron pumps [120].

Evaluation of the different possible heating mechanisms in SAW-magnetic film systems is therefore crucial in order to distinguish between heating- and SAW-induced effects. In this chapter, we therefore examine heating within a SAW device that comprises of a Ta/Pt/Co/Ta thin film with PMA in the presence of standing or travelling SAWs within a frequency range of 46 to 51 MHz and at a power of 21 dBm. In contrast to the Ta/Pt/Co/Ir/Ta thin films discussed in the previous chapter, the Ta/Pt/Co/Ta thin film used in this chapter demonstrated a smoother DW profile, attributable to the reduced DMI at the Co/Ta interface. This feature enabled more precise measurements of DW velocity under a range of experimental conditions. The heating was measured *in situ* using Pt thin film thermometers placed at several locations on the same chip, including within the SAW beam path. DW velocity was also separately determined

at different temperatures firstly with no SAW applied, and secondly in the presence of standing or travelling SAWs, allowing us to discuss and investigate fully the origin and impact of heating, and to distinguish it from the SAW driven effects. Results obtained in this chapter were published as “*Separation of heating and magnetoelastic coupling effects in surface-acoustic-wave-enhanced creep of magnetic domain walls*”, *Physical Review Applied*, 20, 014002 (2023) [18].

5.2 Methods

5.2.1 Magnetic thin film and SAW device

Figure 5.1a shows a schematic of the SAW device used in this chapter. A 2-mm wide Ta(5.0 nm)/Pt(2.5 nm)/Co(0.9 nm)/Ta(5.0 nm) (see Figure 5.1c) thin film with PMA was prepared at the centre of an 128° Y-cut LiNbO₃ substrate with dimensions of 10 × 12 × 0.5 mm³ by dcMS. One pair of Ti(10 nm)/Au(90 nm) IDTs was patterned at either end of the magnetic thin film using optical lithography, followed by metal evaporation and lift-off. Each IDT consisted of 20 pairs of electrodes. The aperture of the IDTs and the distance between the two IDTs were set at 500 μm and 3 mm, respectively. Both the electrode width and pitch were designed to be 20 μm, resulting in a SAW wavelength (λ) of ~80 μm. A Pt film with dimensions of 200 × 200 × 0.075 μm³ was deposited by dcMS to determine temperature changes. This film was situated between the magnetic thin film and the IDTs within the SAW beam path. The distance from the centre of the thermometer (located within the SAW beam path) to the edge of the magnetic thin film was 250 μm. Figure 5.1b provides a schematic representation of the Pt film. Four-terminal electrical transport measurements were conducted using a combined Keithley 6221-2182A current source (connected to Ports 1 and 2 in Figure 5.1b) and a nano-voltmeter (connected to Ports 3 and 4 in Figure 5.1b).

5 Separation of heating and strain effects

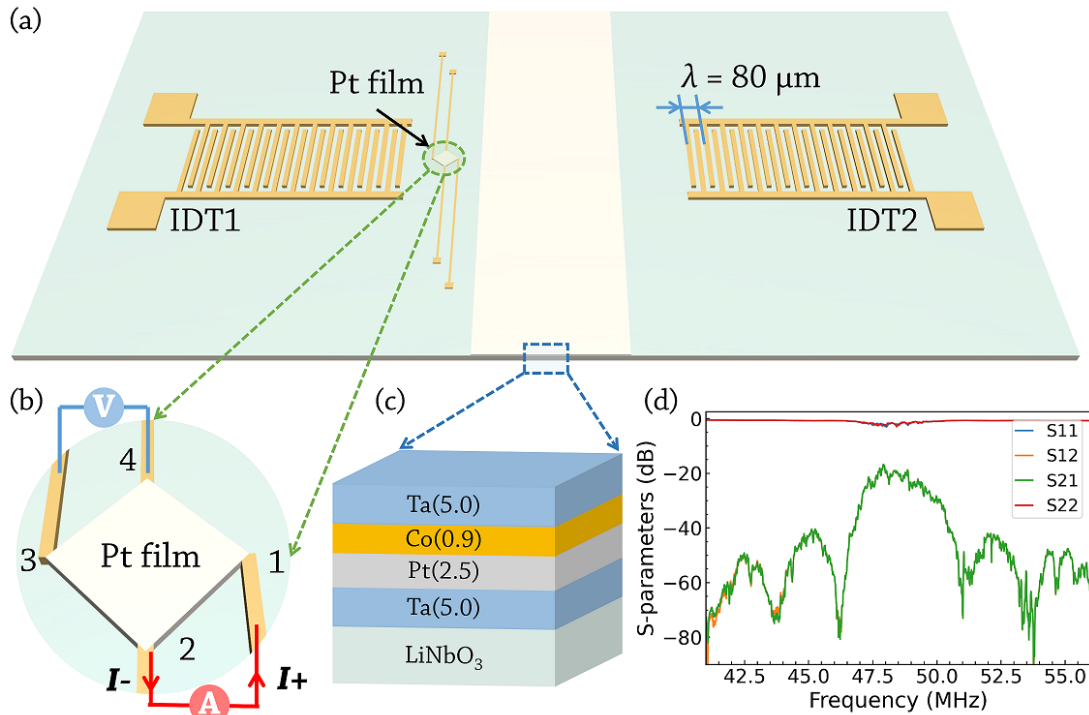


Figure 5.1: (a) Schematic diagram of the SAW device (not to scale). A 2-mm wide magnetic thin film is deposited by dcMS onto a LiNbO_3 substrate. A pair of IDTs, designed to launch SAWs with a wavelength (λ) of $80 \mu\text{m}$, are positioned at the opposite ends of the magnetic thin film. In between the magnetic thin film and the IDTs, and within the path of the SAW beam, a Pt film is patterned. (b) Schematic representation of the electrical transport measurements using the Pt film. Current passes through Ports 1 and 2, while voltage is simultaneously measured at Ports 3 and 4. (c) The structure of the Ta(5.0 nm)/Pt(2.5 nm)/Co(0.9 nm)/Ta(5.0 nm) thin film. (d) S-parameters for the IDTs used to launch SAWs. The delay line, which includes both IDTs and the substrate, exhibits a centre frequency of 48 MHz.

5.2.2 SAW circuit and S-parameters

S-parameters were measured using the method discussed in Section 3.4.3, allowing the determination of the peak value of transmission as a function of frequency, at which point SAWs were generated most strongly (with a 19.67 dB transmission loss at a centre frequency of 48 MHz for the device used in the chapter, see Figure 5.1d). Figure 5.2a and b show schematic diagrams of the rf circuit for launching standing SAWs and travelling SAWs, respectively. For both circuits, the signal generator (Agilent E5062A) sent out rf signals to an attenuator (9.83 dB, Mini-Circuit BW-S10W2+) before being amplified (with a gain of 33.99 dB at 48 MHz at 24 V dc voltage, Mini-Circuits ZHL-2-8-S+) to ensure that the applied power did not exceed the linear regime of the amplifier.

To form standing SAWs, a power splitter (Mini-Circuit ZAPD-30-S+) was used to divide the rf signal into two, with each resulting signal then sent to one IDT (Figure 5.2a). As for the rf circuit for launching travelling SAWs, rf signals were sent directly to either one of the IDTs (Figure 5.2b). The total power loss from the power splitter was 4.39 dB, comprising 3 dB of split power loss and 1.39 dB of insertion loss for each branch. This loss was compensated for by the power from the signal generator (6.40 dBm for standing SAWs and 5.00 dBm for travelling SAWs) to ensure that the power level was the same for both standing SAWs and travelling SAWs. Thus, we can state that the total loss, associated with three factors: (i) cabling, (ii) transduction at the IDT (expected to be the largest factor given no impedance matching was used), and (iii) SAW propagation to the centre of the device, together introduces $19.67 \text{ dB}/2 = 9.84 \text{ dB}$ total loss from each port to the centre of the (symmetric) device. Therefore, the power sent to the IDT for both standing SAWs and travelling SAWs was the same ($\sim 21 \text{ dBm}$), which can qualitatively compare the heating and strain (induced by standing SAWs and travelling SAWs) effects on DW motion. Figure 5.1d shows the reflection (S11 and S22) and transmission (S21 and S12) characteristics

5 Separation of heating and strain effects

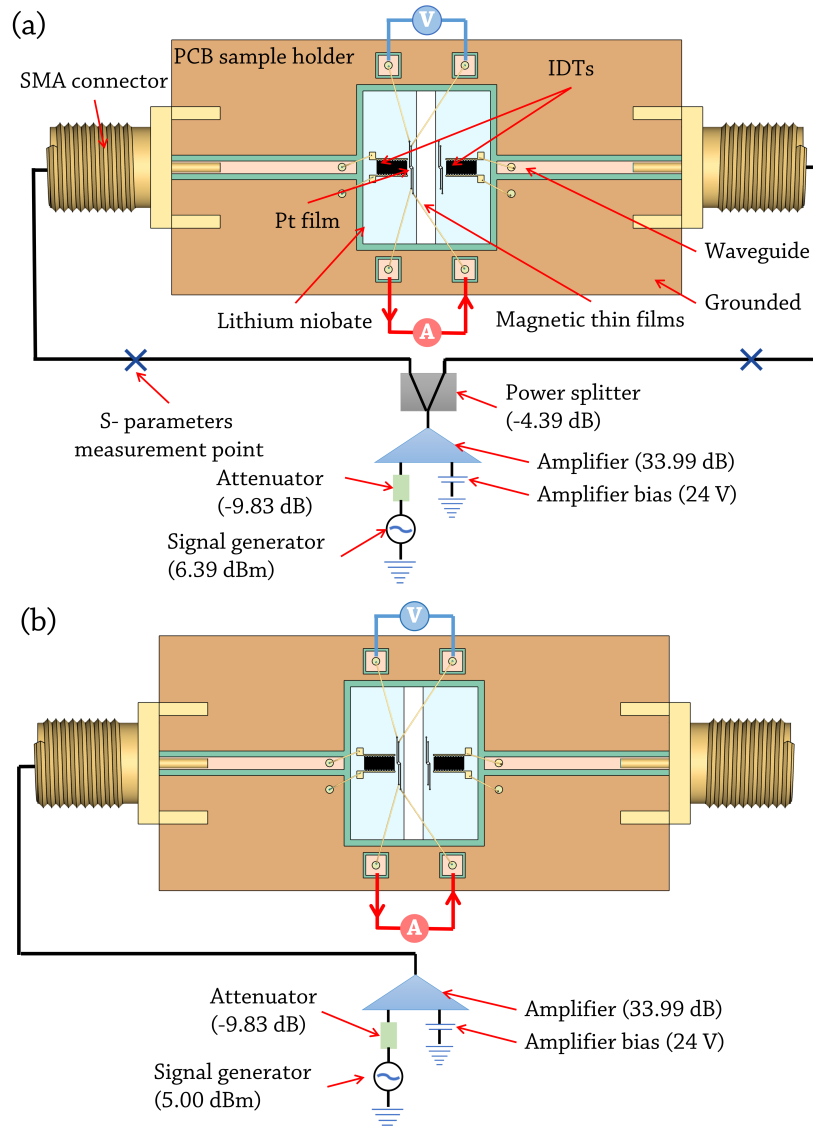


Figure 5.2: Schematic diagram of rf circuits used to generate (a) standing SAWs and (b) travelling SAWs. The signal generator, attenuator, amplifier and power splitter were removed and a VNA was connected between the “X” points for S-parameter measurements. Electrical transport measurements were performed using a conventional four-point-probe measurement to determine the temperature changes while applying SAWs.

of the SAW transducers and substrate, exhibiting a centre frequency of 48 MHz.

5.2.3 Determination of temperature change

The temperature change (ΔT) at the Pt thermometer was obtained using the equation

$$\Delta T = \alpha_0(R - R_{RT}), \quad (5.1)$$

where α_0 is the temperature change of the Pt per unit resistance ($\text{K}/\text{m}\Omega$), R is the measured Pt resistance, and R_{RT} is the Pt resistance at room temperature. The resistance of Pt linearly increases with increasing temperature (see Figure 5.3a), and the value of α_0 is $0.888 \pm 0.004 \text{ K}/\text{m}\Omega$, obtained by finding and averaging the reciprocal of the gradient of the Pt resistance-temperature curve for four different Pt thin films with the same dimensions (Pt 1 to Pt 4 in Figure 5.3a) across a temperature range from 250 to 280 K. The R_{RT} was measured at the beginning and the end of each measurement (Figure 5.3b).

5.2.4 Determination of domain wall velocity

The DW velocity was measured using wide-field Kerr microscopy. Figure 5.4a shows an example image used for determining the DW velocity. The magnetic thin film was first saturated using a large magnetic field of -300 Oe (the coercivity of the thin film is approximately 60 Oe). A short pulse (0.2 s) of a magnetic field with the opposite direction (50 Oe) was applied to nucleate a domain at the edge of the thin film (arrow A in Figure 5.4a). The first image was recorded, followed by the application of another magnetic field pulse to move the DW (arrow B in Figure 5.4a). The second image was then taken, and the difference between the two images (the distance between A and B) was used to extract the distance that the DW travels. The framed area in Figure 5.4a was cropped and converted into binary values, as shown in Figures 5.4b

5 Separation of heating and strain effects

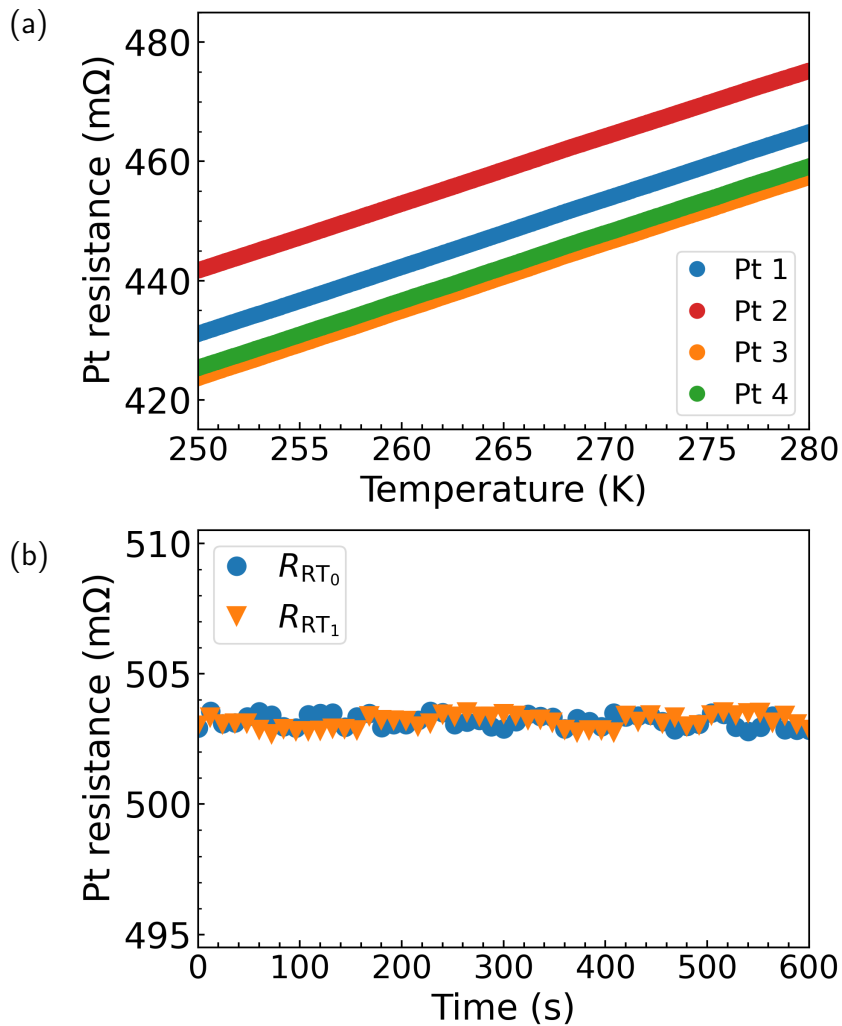


Figure 5.3: (a) Pt resistance against temperature. Four different Pt thin films (Pt 1 to Pt 4) were measured within the temperature range of 250 to 280 K, and the mean of the four measurement was used to determine the resistance changing rate against temperature. (b) Pt resistance against time for continuous 10 minutes at room temperature before (R_{RT_0}) and after (R_{RT_1}) the application of SAWs. The average of the Pt resistance was used as reference resistance at room temperature.

5.2 Methods

and 5.4c, respectively. There were few scratches formed on the substrate during the fabrication process, which created artificial pinning sites affecting the DW motion. The chosen area is free from such scratches. The number of black pixels in Figure 5.4c was plotted against the distance, as shown in Figure 5.4d.

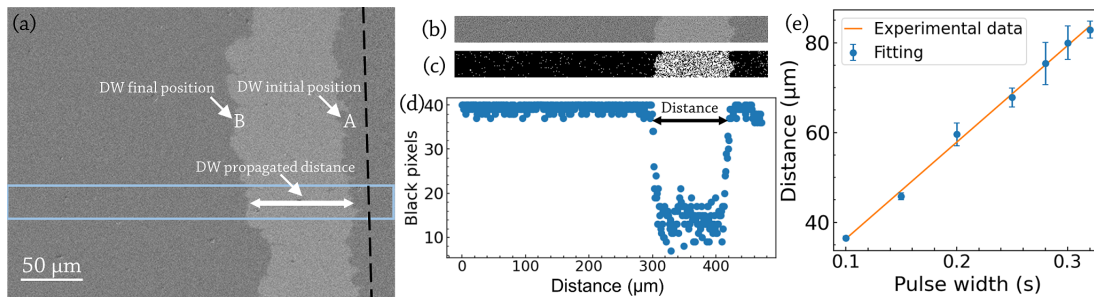


Figure 5.4: Determination of the DW velocity in the Ta/Pt/Pt/Ta thin film. (a) An example image used to determine the DW velocity. The dash line is the boundary of the thin film (left) and substrate (right). Arrow A and B indicate initial and final positions the DW, respectively. The distance between A and B is the DW propagating distance. (b) The cropped image from the framed area in (a). (c) The binary value of the image (b). (d) The averaged number of black pixels in (c) against the distance. (e) The DW propagating distance against pulse widths of the magnetic field. Data points and the straight line in the graph are experimental results and its linear fit, respectively.

A series of pulses was applied to the thin film, and the velocity was then obtained by finding the gradient of the distance against the pulse width (see Figure 5.4e). Seven different pulse widths were applied to the thin film, and each pulse width was repeated three times. Images for all measurements were taken at the same position to ensure that the DW velocity was comparable for all studied cases. DW velocity was firstly measured from 19°C (room temperature, RT) to 49°C ($\Delta T = 30$ K) without SAWs. The sample was heated by the hot side of a Peltier device placed underneath the

5 Separation of heating and strain effects

sample. DW velocity was also measured in the presence of standing SAWs and then travelling SAWs at the frequency of 48 MHz and a power of 21 dBm with no heating applied from the Peltier device.

5.3 Results and discussion

5.3.1 Temperature change in device

Figure 5.5a and b show the temperature changes (ΔT) of the thermometer within the SAW beam path against source frequency with a total rf power of 21 dBm. We focus on the temperature changes within the SAW bandwidth (from 46 MHz to 51 MHz, corresponding to the centre peak in Figure 5.1d). In the presence of standing SAWs, four temperature peaks (~ 47.38 MHz, ~ 48.00 MHz, ~ 48.85 MHz, and ~ 49.75 MHz) can be observed, with the largest ΔT of 10.4 ± 0.5 K being at the centre frequency of 48 MHz (SW in Figure 5.5a). The formation of the four resonant peaks can be explained by the constructive and destructive interference at certain frequencies causing different mechanical reflections at the IDTs.

Upon application of travelling SAWs (TW1 and TW2 in Figure 5.5a), the temperature of the Pt increased as the centre frequency was approached, reaching a maximum temperature near the centre frequency with a few local minimum temperatures due to rf reflections from the IDT and sample edges. This trend generally corresponds to the reflection and transmission coefficients (overlaid on the ΔT in Figure 5.5a) across the bandwidth. TW1 causes a slightly higher temperature increase at lower frequencies compared to TW2. For example, at 47 MHz, the temperature increases are 8.1 ± 0.2 K and 5.5 ± 0.3 K for TW1 and TW2, respectively. This is because this thermometer is closer to IDT1, implying that dissipation of rf power at the transducer or its bonded wire contributes to the observed change in temperature. The highest temperature increases for TW1 and TW2 occur at 47.85 MHz and 47.83 MHz, respectively, with

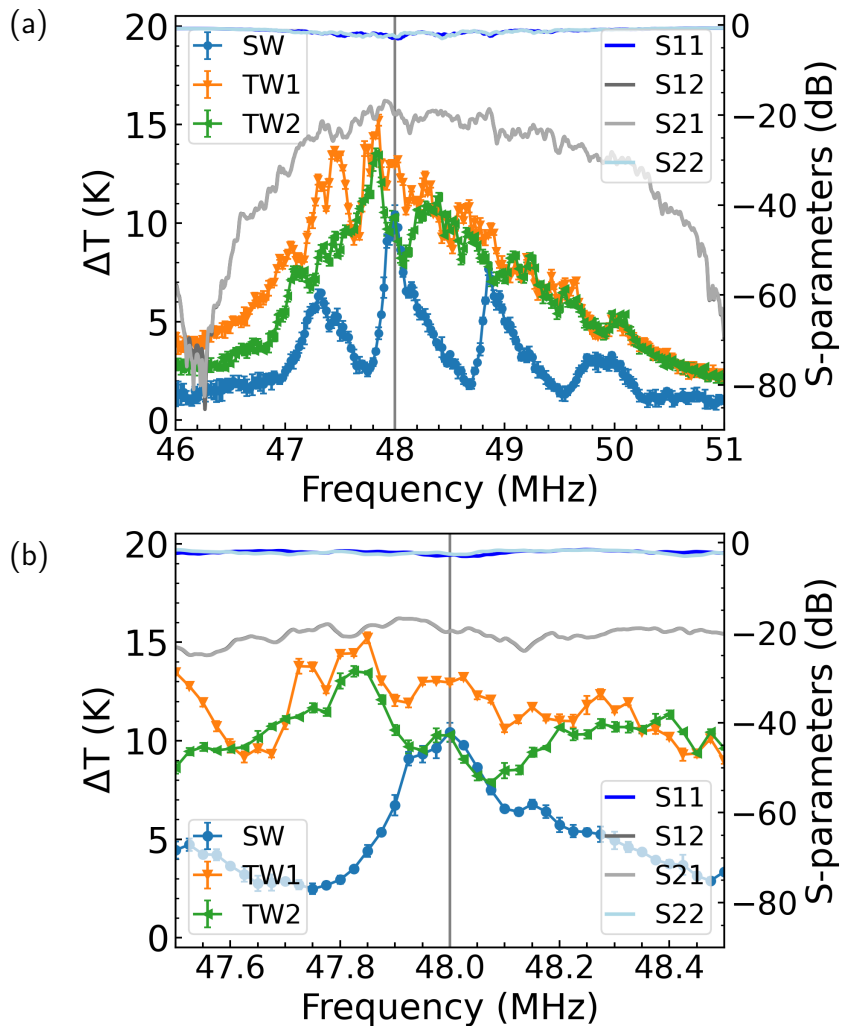


Figure 5.5: (a) Temperature changes (ΔT) of the Pt within the SAW beam path as a function of source frequency from 46 to 51 MHz with rf power of 21 dBm. (b) Zoomed-in temperature changes of the device against SAW frequencies from 47.5 to 48.5 MHz. SW, TW1, and TW2 in the legend denote standing SAWs, travelling SAWs launched from IDT1, and travelling SAWs launched from IDT2, respectively. Lines are the guide to the eye.

5 Separation of heating and strain effects

values of 15.2 ± 0.3 K and 13.5 ± 0.3 K, as listed in Table 5.1. Detailed temperature changes around the centre frequency can be found in Figure 5.5b. Within a specific narrow range, there is a discrepancy between the behavior of temperature and the S-parameter. This difference might be from intricate interference generated by reflections occurring either at the IDTs or within the thin film. At 48 MHz, the temperature increases are 12.9 ± 0.1 K and 10.3 ± 0.3 K for TW1 and TW2, respectively.

Table 5.1: Maximum temperature changes (ΔT_{\max}) of the device and corresponding frequencies, and temperature changes at centre frequency ($\Delta T_{48\text{MHz}}$) in the presence of SAWs.

SAW type	ΔT_{\max} (K)	Corresponding frequency (MHz)	$\Delta T_{48\text{MHz}}$ (K)
SW	10.4 ± 0.5	48.00	10.4 ± 0.5
TW1	15.2 ± 0.3	47.85	12.9 ± 0.1
TW2	13.5 ± 0.3	47.83	10.3 ± 0.3

5.3.2 Heating dynamics model

The source of heating in a SAW-thin film system could be either rf power dissipation due to Joule heating or by an acoustothermal effect introduced by the SAW itself [119, 121]. However, since IDTs operate with the highest efficiency at their resonant frequency, and both rf power dissipation and SAW amplitude depend strongly on the rf frequency, it is not possible to simply apply off-resonant rf signals to distinguish between the two mechanisms. To differentiate between these possible mechanisms, we investigate the detailed thermal behaviour of the collection of thermometers. The temperature of the thermometer rapidly rises after the rf power is applied and reaches a steady state after about 30 s, as shown in Figure 5.6.

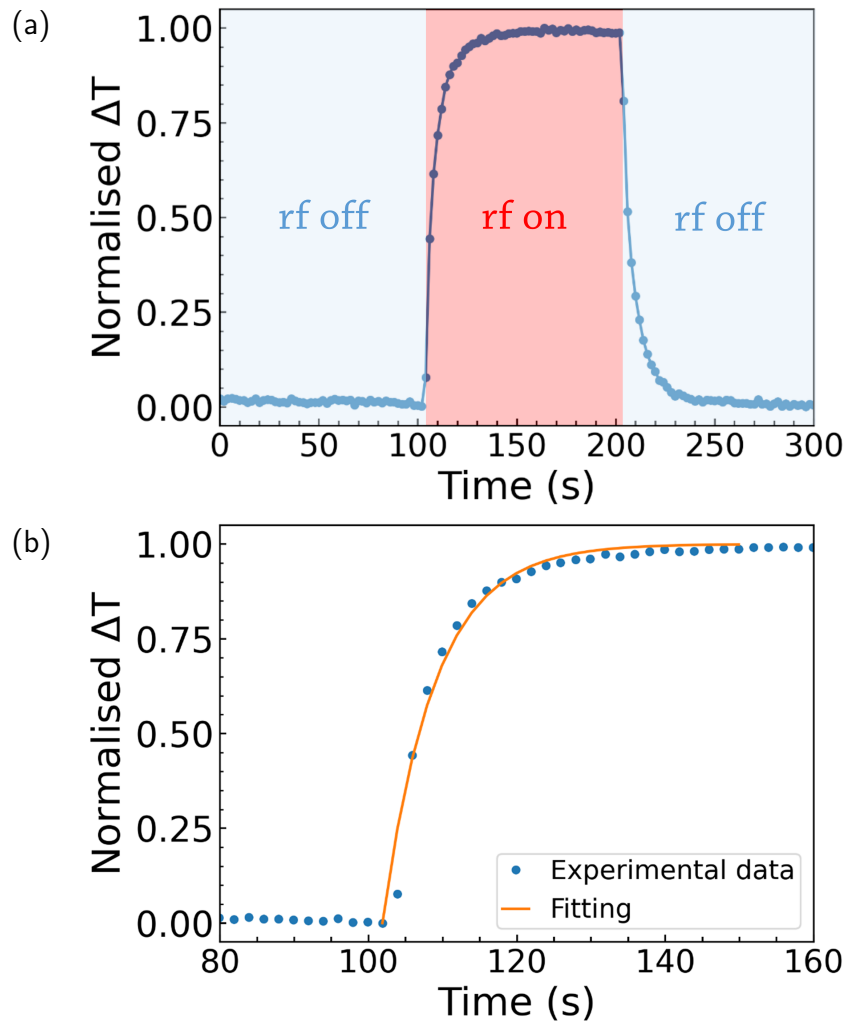


Figure 5.6: (a) Normalised ΔT progression: Temperature is first measured without rf power (0–100 s), followed by measurement with rf power applied (100–200 s), and concludes with a 100 s duration after the rf power is turned off. (b) Normalised temperature variations (ΔT) plotted over time (80–160 s), capturing the rise in thermometer temperature from room conditions to an equilibrium state during SAW presence. The solid line in the primary graph represents the experimental data fitted using Fourier's law.

5 Separation of heating and strain effects

We propose a simple model of the observed heating as follows: Let T_s be the temperature of the source, and T be the temperature of the thermometer. Based on the Fourier's law, the heat influx rate is estimated as

$$\dot{q}_{\text{in}}(t) = \frac{k_0 \mathcal{A}}{r_s} (T - T_s), \quad (5.2)$$

where r_s is the distance from the source of heating, \mathcal{A} is the surface area of heat exchange and k_0 is thermal conductivity of the material. We denote $C_1 = k_0 \mathcal{A} / r_s$ to be the thermal conductance of the material. To account for heat loss, we assume that it occurs via conduction and convection, which can be expressed as

$$\dot{q}_{\text{out}} = C_2 (T - T_{\text{env}}), \quad (5.3)$$

where T_{env} is the temperature of the surroundings and C_2 is the corresponding thermal conductance. The equilibrium temperature T_{eq} can be expressed as

$$T_{\text{eq}} = \frac{C_1 T_s + C_2 T_{\text{env}}}{C_1 + C_2}. \quad (5.4)$$

Before the equilibrium is achieved we use

$$\dot{q}_t = \dot{q}_{\text{in}} - \dot{q}_{\text{out}}, \quad (5.5)$$

where \dot{q}_t is the heat absorbed by the thermometer. If c is the heat capacity of the thermometer, then Equation 5.5 can be re-written as

$$\dot{T} = \frac{C_1 + C_2}{c} (-T + T_{\text{eq}}). \quad (5.6)$$

Solving Equation 5.6 gives the temperature change over time

$$T = T_{\text{eq}} - (T_{\text{eq}} - T_0) \exp\left(-\frac{C_1 + C_2}{c}t\right). \quad (5.7)$$

From the experimental data, we fit T vs t to the $T = T_{\text{eq}} - (T_{\text{eq}} - T_{\text{env}}) \exp(-\tilde{\gamma}t)$. The experimentally obtained $\tilde{\gamma}$ is expected to correspond to $(C_1 + C_2)/c$. Substituting $C_1 = k_0\mathcal{A}/r_s$ we obtain

$$\tilde{\gamma} = \left(\frac{k_0\mathcal{A}}{c}\right) \frac{1}{r_s} + \frac{C_2}{c}. \quad (5.8)$$

We choose to study the $\tilde{\gamma}$ value because it represents the ‘‘heating rate’’ and provides information about the entire heating process, enabling us to better understand its dynamics and variations at different locations. In contrast, temperature only represents the final result of the heating process and does not provide information about its dynamics.

5.3.3 Source of heating

Figure 5.7a shows a schematic layout of the SAW device. Temperature measurements were conducted both inside and outside of the SAW beam path in the presence of the travelling SAW launched from IDT1. The rf power and frequency were set as 21 dBm and 48 MHz, respectively. The thermometer P0 in Figure 5.7a is the same one used in Figure 5.1a, situated within the SAW beam path and expected to experience the SAWs passing through. P1, P1', P2, P2', and P3, P3' are thermometers situated outside the SAW beam path where the SAW amplitude is negligible [130]. P1 and P1', P2 and P2', as well as P3 and P3' were equidistant from the SAW beam path, which were 650 μm , 1250 μm above IDTs, and 650 μm below IDTs, respectively. This arrangement allowed us to determine whether heating was from the SAW itself (acoustothermal heating) or from rf power dissipation (Joule heating). We consider

5 Separation of heating and strain effects

the two possible sources of heating mentioned above: acoustothermal heating effect and rf power dissipation. If the heating is predominantly caused by the acoustothermal effect, the highest $\tilde{\gamma}$ value would be expected within the beam path, while if it is due to rf power dissipation, the highest $\tilde{\gamma}$ should occur at the thermometer closest to the rf bond pad.

Figure 5.7b presents the heating rate $\tilde{\gamma}$ obtained at various locations in response to the travelling SAWs generated from IDT1. The heating rate at P0 is $0.130 \pm 0.010 \text{ s}^{-1}$, which is lower than the values measured at P1 ($0.148 \pm 0.005 \text{ s}^{-1}$) and P3 ($0.160 \pm 0.007 \text{ s}^{-1}$). This indicates that P1 and P3 are located closer to the heating source compared to P0. Furthermore, under the same conditions, the heating rate at P1' ($0.118 \pm 0.008 \text{ s}^{-1}$) and P3' ($0.115 \pm 0.008 \text{ s}^{-1}$) is lower than those measured at P1 and P3, respectively, suggesting that the heating source is situated close to IDT1 where the rf power is applied. The origin of this heating is therefore likely to be power dissipated at the IDT in the rf to SAW transduction process. Notably, we observe a good linear relationship when plotting the $\tilde{\gamma}$ values against the reciprocal of the distance between the bond pad (where the rf power is applied, red circle shown in Figure 5.7a) and the centre of the thermometer. Furthermore, the heating rates $\tilde{\gamma}$ are much higher at P1 and P3 than that at P0, where SAWs are excited. Based on these results, we conclude that the heating observed in our SAW-magnetic thin film system is predominantly due to rf power dissipation (introduced by Joule heating) rather than the acoustothermal heating effect introduced by the SAW itself.

Figure 5.7c presents a breakdown of the rf power flow in our device. When rf signals are applied to the IDTs, a portion of the power is reflected back to the source, while the rest is injected into the IDTs. The proportion of the rf power converted accordingly is influenced by several factors: (i) the reflection at the connection between the SMA cable and bond pads, (ii) the reflection at the bond pads to IDTs, and (iii) the reflection coefficient of the IDTs (S11 or S22), all of which are sensitive to the rf

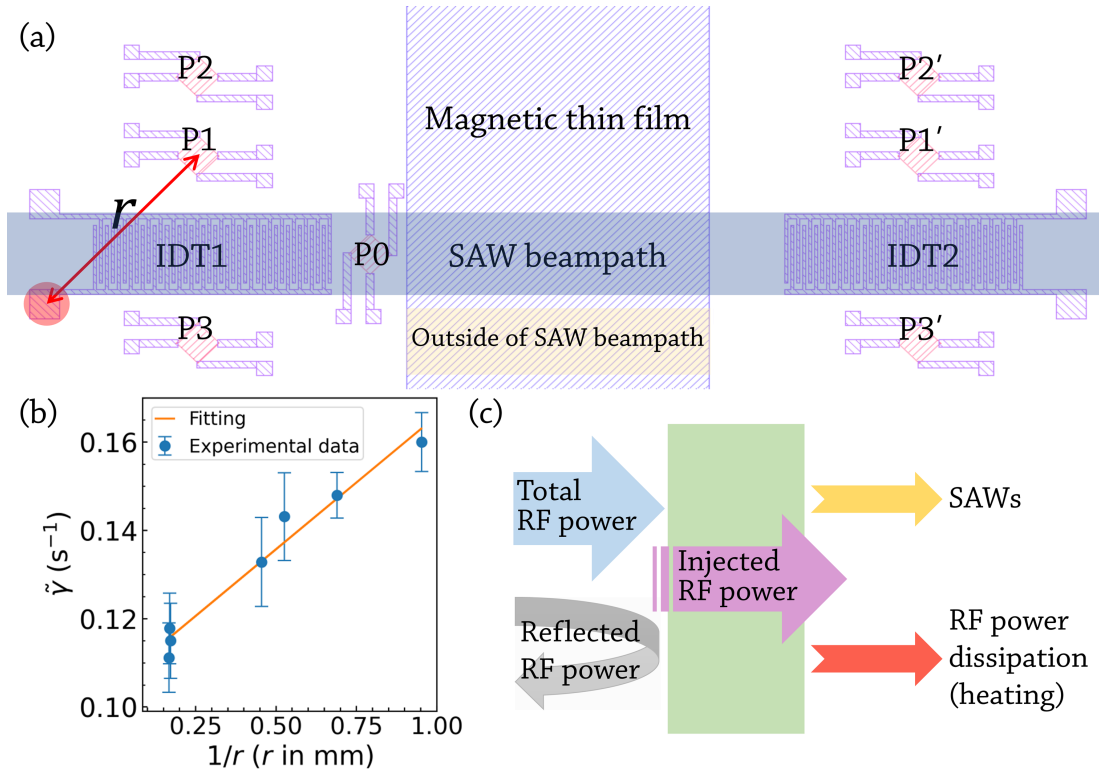


Figure 5.7: (a) Schematic layout of the SAW device showing seven thermometer positions: P0, located within the SAW beam path, and P1 (P1'), P2 (P2'), and P3 (P3') located outside of the SAW beam path, at different distances from IDT1 (IDT2). DW velocity is also measured outside of the SAW beam path (labelled as "Outside of SAW beam path") to confirm the magnetoelastic coupling effect on DW motion. (b) Plot of the $\tilde{\gamma}$ against $1/r$ in the presence of a travelling SAW launched from IDT1, with a frequency of 48 MHz and power of 21 dBm. r is defined as the distance from the rf bond pad (red circle) to the centre of the thermometer. The solid line represents the linear fitting of $\tilde{\gamma}$ against $1/r$. (c) Diagram of the rf power breakdown.

5 Separation of heating and strain effects

frequency. Among these factors, the greatest reflection occurs from (iii) given that no impedance matching was used. We calculate the injected power by subtracting the reflected rf power from the total rf power. A portion of the injected power is converted into surface acoustic waves, which is dependent on the electromechanical coefficient of the LiNbO_3 , while the remaining injected power is dissipated in the form of heating. Therefore, the S-parameters and other reflections influence both the rf heating and SAW amplitude, with a higher heating effect corresponds to a higher SAW amplitude.

5.3.4 Heating and strain effects on domain wall velocity

We now examine the relationship between temperature and DW velocity. Figure 5.8a shows the obtained DW velocity within the SAW beam path plotted against the applied magnetic field. The DW velocity was initially measured at room temperature ($\sim 19^\circ\text{C}$). As the field increases from 47 to 65 Oe, the DW velocity was found to increase from 3 ± 2 to 33 ± 3 $\mu\text{m/s}$. As depicted in Figure 5.8b, a plot of $\ln v$ against $H^{-1/4}$ shows a linear dependence using Equation 2.25. This indicates that the DW motion is in the creep regime, where thermal energy enables DWs to overcome the pinning barriers. The DW creep motion can be enhanced by increasing the temperature. We study the temperature dependence of the DW velocity by heating our device by 10, 20, and 30 K using a Peltier device. As shown in Figure 5.8a, DW motion is significantly enhanced as the temperature increases. For instance, under a field of 65 Oe, the DW velocity increases from 33 ± 3 $\mu\text{m/s}$ at room temperature to 650 ± 30 $\mu\text{m/s}$ when the temperature is increased by 30 K. According to creep law (Equation 2.25), the DW motion still remains in the creep regime as the $\ln v$ shows a linear dependence on $H^{-1/4}$ (see Figure 5.8b).

DW velocity was measured in the presence of SAWs at the same position within the SAW beam path. The frequency and power of both standing and travelling

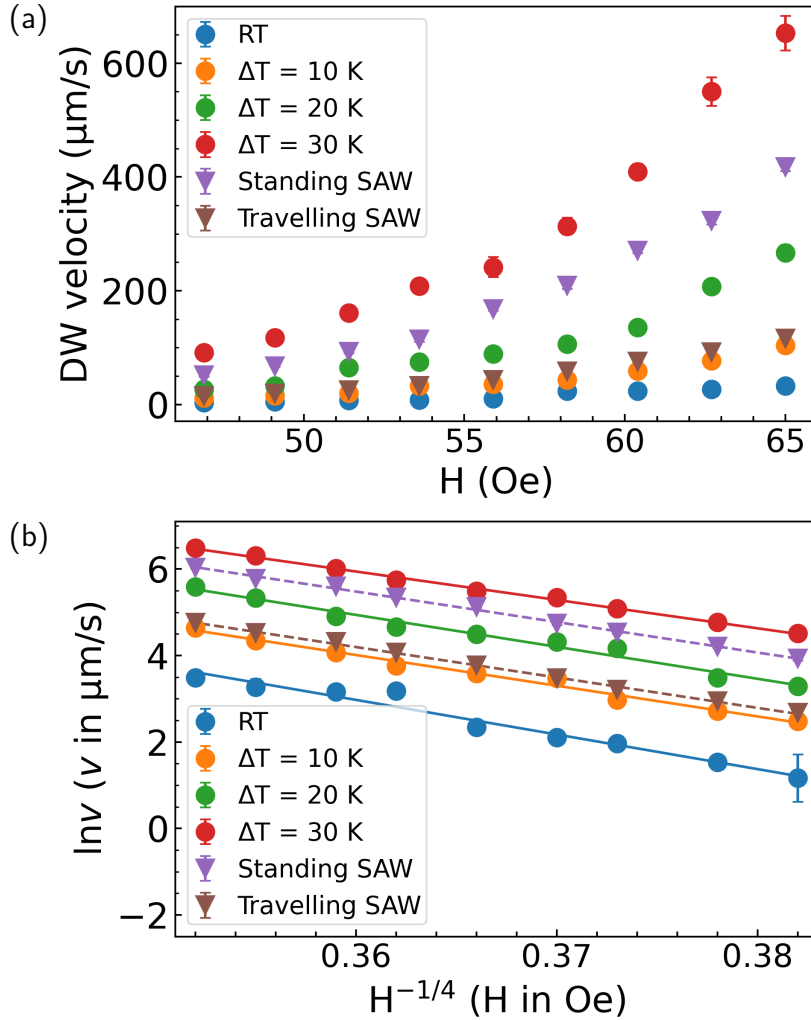


Figure 5.8: (a) DW velocity in the Ta/Pt/Co/Ta thin film as a function of the applied field (H). (b) Natural logarithm of DW velocity (v) as a function of $H^{-1/4}$. DW velocity is measured at different temperatures from room temperature (RT) up to $\Delta T = 30$ K without SAWs (circles) and in the presence of standing SAWs and travelling SAWs at centre frequency of 48 MHz and rf power of 21 dBm without additional heating (triangles). The solid and dashed lines are linear fitting of the DW velocity experimental data at different temperatures and in the presence of the SAWs, respectively.

5 Separation of heating and strain effects

SAWs were set at 48 MHz and 21 dBm, respectively. DW motion was found to be enhanced in the presence of both types of SAWs (see Figure 5.8a). With application of travelling SAWs, the DW velocity is $116 \pm 3 \mu\text{m/s}$ at 65 Oe, representing a ~ 2.5 -fold increase compared to the measurement at room temperature. However, an even greater enhancement of DW motion can be observed in the presence of standing SAWs, with a velocity of $418 \pm 8 \mu\text{m/s}$, which is a ~ 11.7 -fold increase from the room temperature measurement. DW motion still remains within the creep regime in the presence of both travelling and standing SAWs over the measured field range (see Figure 5.8b). The Kerr microscope images of the DW profile under different experimental conditions are presented in Figure 5.9. The DWs are nucleated at the left-hand side (as indicated as DW initial position in Figure 5.9a). The DWs move towards the right-hand side (as indicated as DW final position in Figure 5.9a) driven by the magnetic field with/without SAWs. The DW exhibits a mostly smooth profile when subjected to a magnetic field of 65 Oe, as shown in Figure 5.9a. Increasing the temperature by 10 K (Figure 5.9b) or introducing standing SAWs (Figure 5.9c) and travelling SAWs (Figure 5.9d) does not cause any significant changes in the DW profile.

The enhancement of DW motion observed in the presence of SAWs is likely caused by a combination of both the magnetoelastic coupling effect and the heating effect induced by rf power dissipation. The thermometer experiences a temperature increase of ~ 10 K at 48 MHz (as shown in Table 5.1). In Figure 5.8a, the DW velocity curve with a 10 K temperature increase is similar to the travelling SAW-assisted DW velocity curve. However, the DW motion enhancement observed with standing SAWs is much greater than that achieved by increasing the temperature by 10 K alone. These results suggest that heating plays a major role in promoting DW motion in the presence of travelling SAWs, while the magnetoelastic coupling effect is the primary factor for significant DW motion with the application of standing SAWs.

5.3 Results and discussion

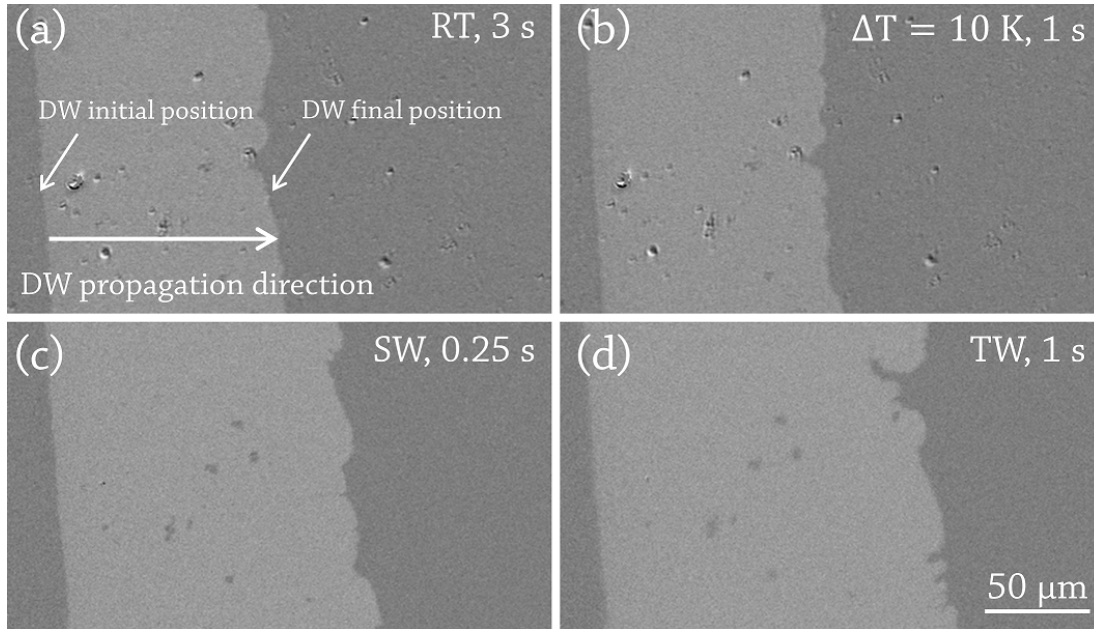


Figure 5.9: DW profile in the Ta/Pt/Co/Ta thin film under different experimental conditions imaged using a Kerr microscope. (a) Magnetic field applied at room temperature for 3 s, (b) Magnetic field applied with a temperature increase of 10 K for 1 s, (c) Standing SAWs with magnetic field applied for 0.25 s, and (d) Travelling SAWs with magnetic field applied for 1 s. The magnetic field strength used is 65 Oe, and the frequency and power of the SAWs are 48 MHz and 21 dBm, respectively. The arrow in (a) indicates the direction of the DW propagation.

Our study highlights the significance of heating in SAW-thin film systems, particularly with higher power SAWs. We perform DW velocity measurements at a location 100 μm away from the SAW beam path (referred to as “Outside of SAW beam path” in Figure 5.7a). This location was chosen because it still experiences some heating effect, albeit to a lesser degree, yet the SAW amplitude was negligible in that area [121, 130]. With an applied magnetic field of 65 Oe, the DW velocity increased from $33 \pm 2 \mu\text{m/s}$ at room temperature to $75 \pm 3 \mu\text{m/s}$ and $78 \pm 4 \mu\text{m/s}$ in the presence of

5 Separation of heating and strain effects

standing and travelling SAWs, respectively. This DW velocity increase outside of the SAW beam path confirms the role of Joule heating in enhancing DW motion.

Furthermore, strain can modify the magnetic anisotropy of thin films through the magnetoelastic coupling effect [44, 53, 56, 131]. The resulting changes in magnetic anisotropy create a dynamic energy landscape that reduces the energy requirement for DW motion. Specifically, the dynamic strain waves associated with the SAWs cause the magnetic anisotropy to periodically change, enhancing the possibility of DW depinning from pinning sites and facilitating faster DW motion. However, the distinct impacts of standing versus travelling SAWs on DW velocity remain to be fully understood and require further investigation. Notably, observations from samples with varying magnetic layer thicknesses (not included in this thesis) have revealed a divergence in DW velocity when subjected to standing and travelling SAWs with different frequencies. This phenomenon suggests a complex underlying mechanism and indicates that considerable investigative effort is required to elucidate these dynamics.

5.4 Summary

In this chapter, we explored the impact of both heating and SAWs in a SAW-magnetic film system, measuring the impact of both heating and SAWs on DW velocity. Heating of approximately 10 K was observed within the SAW beam path when rf power was applied. DW velocity was measured at various temperatures both with and without SAWs. The DW velocity increased from 33 ± 3 to 650 ± 30 $\mu\text{m/s}$ as the temperature rose from 19°C to 49°C at 65 Oe. The DW velocity enhancement by travelling SAWs (116 ± 3 $\mu\text{m/s}$) was found to be slightly higher than that obtained a 10-K temperature increase (104 ± 8 $\mu\text{m/s}$), suggesting that heating played a major role in promoting DW motion. On the other hand, DW motion was significantly enhanced in the presence of standing SAWs (418 ± 8 $\mu\text{m/s}$) due to the dominant effect of mag-

5.4 Summary

netoelastic coupling. Our study underscores the importance of considering heating in SAW devices, especially those using high rf power, and presents a straightforward way of measuring heating in SAW devices and interpreting such effects.

5 Separation of heating and strain effects

CHAPTER 6

SAW effect on domain wall dynamics

6.1 Introduction

SAWs are capable of introducing dynamic strain waves into magnetic thin films [7]. Through the magnetoelastic coupling effect, these dynamic strain waves generate a dynamic energy landscape, thereby triggering magnetisation precession [8–10], facilitating magnetisation switching [11, 12], and enhancing the DW motion [13–18]. The utilisation of SAWs has demonstrated significant promise for achieving energy-efficient control of DW motion. However, a comprehensive understanding of the detailed mechanisms and effects underlying the interaction between SAWs and DWs is currently lacking. Moreover, the influence of defects and disorders in thin films on SAW-assisted DW motion remains largely unexplored. Thus, there is a knowledge gap regarding the systematic investigation of the impact of SAW frequency on DW dynamics in films with varying levels of disorders. Addressing this gap is crucial for advancing our understanding of SAW-assisted DW motion and unlocking its full potential for energy-efficient DW control.

In this chapter, we investigate the influence of SAW frequency (50, 100, and 200 MHz) on DW motion within thin films with different levels of anisotropy disorder (1% and 3%) at low fields (up to 1 mT) using micromagnetic simulations. This chapter also delves into the DW depinning process under different conditions, with a particular focus on VBLs. By conducting these investigations, we aim to gain insights into the intricate dynamics of SAW-assisted DW motion and its interaction with disorders, ultimately contributing to the development of energy-efficient DW control techniques. Results obtained in this chapter were accepted for publication as “*Surface acoustic wave effect on magnetic domain wall dynamics*”, *Physical Review B*, 108, 104420 (2023) [132].

6.2 Model and computational details

6.2.1 Proposed device and simulation configuration

Figure 6.1a depicts a schematic diagram of the proposed device that can be implemented by depositing a Pt/Co/Pt micro-wire with PMA onto a 128° Y-cut LiNbO₃. At both ends of the magnetic thin film, a pair of IDTs are patterned. By adjusting the width and pitch of the IDT electrodes, SAWs with various frequencies can be generated. Figure 6.1b shows the simulated system employed in this study. The simulations in this work were performed using Mumax3, a GPU-accelerated micromagnetic simulation program [112]. Mumax3 integrates numerically the LLG equation (Equation 2.3). A Bloch DW separating left and right domains was initialised at a distance of one-fourth from the left edge. The system then relaxed to equilibrium before an external magnetic field (\mathbf{H}_{ext}) pointing “in” was applied favouring the DW motion towards the right. The material parameters used in the simulations were chosen to match those of the Pt/Co/Pt thin films as referenced in the literature [65]: saturation magnetisation $M_s = 6 \times 10^5$ A/m, exchange constant $A_{\text{exch}} = 1.0 \times 10^{-11}$ J/m, anisotropy constant $K_u = 8 \times 10^5$ J/m³, and Gilbert damping constant $\alpha = 0.01$. A low Gilbert damping parameter was selected in the simulations to enhance the DW motion, thereby decreasing the required computational time to observe significant DW displacement. The grid size and cell size of the simulation were set at $256 \times 512 \times 1$ nm³ and $2.4 \times 2.4 \times 1.0$ nm³, respectively, which resulted in a computational region of $614.4 \times 1228.8 \times 1$ nm³. Simulations were intentionally conducted at 0 K to distinctly elucidate the influences induced by SAWs in the absence of thermal activity. Temperature is a crucial factor in thermally-assisted DW motion within the creep regime; nonetheless, incorporating temperature into the simulation adds a layer of complexity that can obscure the specific effects of SAWs. To clarify the impact of temperature, a comparative analysis of simulations with and without thermal influ-

6 SAW effect on domain wall dynamics

ence is presented towards the end of the chapter. This approach allows for a focused examination of the SAW effects while also acknowledging the role of temperature in experimental conditions.

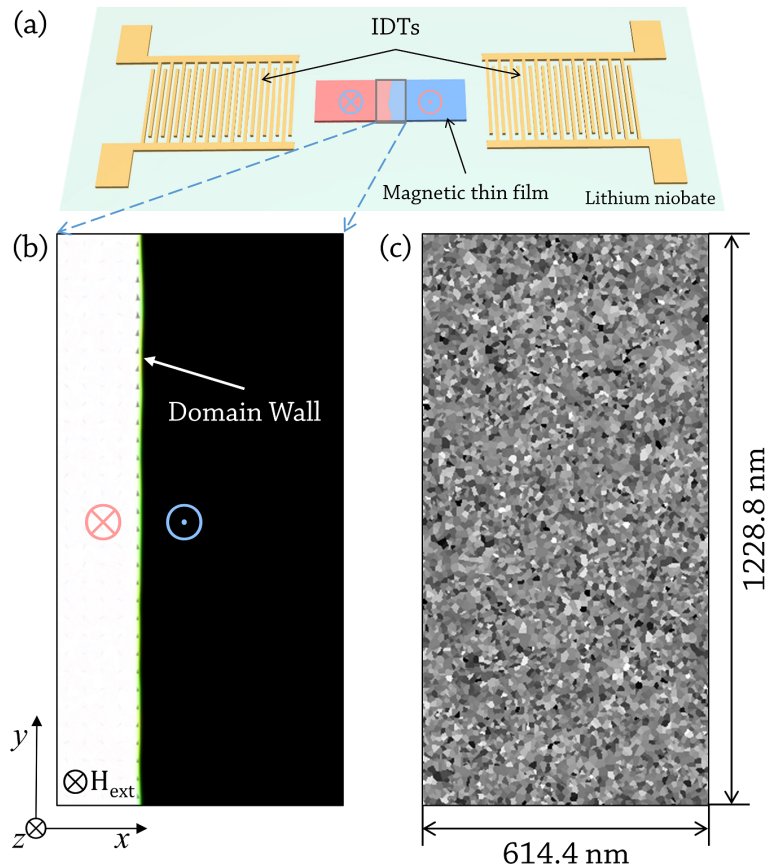


Figure 6.1: (a) Schematic diagram of the proposed device (not to scale) consisting of a magnetic micro-wire with PMA deposited onto a LiNbO_3 substrate and a pair of IDTs used to launch SAWs. (b) Initial magnetisation of the micro-wire with a Bloch DW separating left and right domains. The external magnetic field favors the expansion of the left domain, and the travelling SAWs propagate from left to the right along the x -axis. (c) A typical grain distribution where the grey level is proportional to the value of K_u for each grain. Figure (b) and (c) have the same dimensions.

6.2.2 Incorporating disorder and SAW in simulations

To introduce disorder in our simulations, we utilised the built-in function of Mumax3, which defines grain-like regions using Voronoi tessellation [133]. A typical grain distribution with an average diameter $d_{\text{grain}} = 10$ nm, consistent with experimental observation, is shown in Fig 6.1c [87, 134]. We assigned anisotropy constants (K_u) to each grain, randomly distributed according to a normal distribution centered around their nominal value of 8×10^5 J/m³. The standard deviation (σ) was utilised to control the level of disorder. Specifically, we consider two typical values of σ : 1% and 3% used in simulations [87, 135, 136]. The reason for selecting lower anisotropy disorder values than those observed experimentally is related to the computational timescales; simulating larger anisotropy disorder would necessitate a significantly long computational time to observe DW depinning. A higher σ indicates a greater variation in the anisotropy constants within the thin film, resulting in a higher pinning energy and enhanced pinning effects. By manipulating the σ value, we can effectively modulate the degree of disorder and its impact on the magnetic behavior of the system during simulations.

The magnetoelastic energy density in the system can be described by Equation 2.17. It should be noted that the film is considered acoustically thin, meaning that it is sufficiently thin and rigid for the chosen SAW frequency [80]. As a result, only the in-plane strain component (ϵ_{xx}) needs to be taken into account [13, 19, 65]. In our simulations, we set magnetoelastic coupling coefficient B_1 to be 1.5×10^7 J/m³, and $B_2 = 0$. Travelling SAWs (ϵ_{xx}) were implemented using Equation 3.4. The amplitude of the SAW was set as 0.006, a value selected for its alignment with parameters achievable in experimental settings. The velocity of SAWs propagating in LiNbO₃ is reported as ~ 4000 m/s [103].

6.2.3 Determination of domain wall velocity

The velocity of the DW, denoted as v_{DW} , was determined by the change in the average normalised magnetisation along the z -axis ($\Delta\langle m_z \rangle$) and can be expressed as

$$v_{\text{DW}} = \frac{L_x \Delta\langle m_z \rangle}{2\Delta t_s}, \quad (6.1)$$

where $L_x = 614.4$ nm represents the length of the computational region, and Δt_s is the simulation time. To investigate the effect of SAW frequency on DW dynamics, we set the frequencies of the SAWs as either 50, 100, and 200 MHz. The dynamics of the DW was simulated for 100 ns. This timescale accommodates five complete cycles of SAWs at the lowest frequency employed in these simulations (50 MHz). This simulation time was optimised so that allows SAWs to promote DW motion (as evidenced in Figure 6.4). For each value of the applied field the magnetisation was set to initial magnetisation. To account for the variation in depinning energy among different samples, we generated 10 stochastic realisations for each frequency and disorder level, using the same material parameters but different grain distributions. The data points presented in the results are the ensemble averages of these 10 stochastic realisations, along with corresponding error bars, which indicate the ensemble spread of the 10 simulations.

6.3 Results and discussion

6.3.1 Enhanced domain wall velocity

Figure 6.2 shows the DW velocity as a function of the external magnetic field. For the thin film with 1% anisotropy disorder, DW velocity gradually increases with external magnetic field (see Figure 6.2a), which can be attributed to the relatively low level of anisotropy disorder. Following this, the DW velocity experiences a rapid increase

6.3 Results and discussion

as the field strength rises from 1 to 3 mT. Eventually, a plateau is reached where the DW velocity depends very little on the external magnetic field. The emergence of the plateau in thin film with disorder has been investigated in previous studies [87, 137, 138]. For thin films with 3% anisotropy disorder, the DW velocity is almost zero until a higher depinning field of 3 mT is applied. It enters a plateau at approximately 7 mT (as depicted in Figure 6.2b).

This chapter primarily focuses on the motion of magnetic DWs under low magnetic fields (up to 1 mT). At weak applied fields, particularly around the depinning field, the probability of the DW escaping from pinning sites is contingent upon the local energy potential associated with those sites. The shape of this energy potential is influenced by material defects, with a specific emphasis on anisotropy disorder in this work. Notably, the pinning energy exhibits significant variation across different samples. To account for this variation, we performed simulations using 10 stochastic samples, resulting in a broad ensemble spread. In the thin film with 1% anisotropy disorder, and with no SAWs applied, the DW velocity steadily increases from 0.04 ± 0.05 m/s to 0.3 ± 0.4 m/s as the magnetic field rises from 0 to 1 mT (see Figure 6.3a). However, the presence of SAWs substantially enhances the DW motion across all studied frequencies. For instance, compared to the case without SAWs, the DW velocity is amplified by a factor of 2.7, reaching 1.1 ± 0.3 m/s with an applied field of 1 mT and 50 MHz SAWs. It is worth noting that the DW velocity gradually decreases with increasing SAW frequency. For example, in the presence of 200 MHz SAWs, the overall trend of the DW velocity curve lies below that observed with 50 MHz SAWs. To further illustrate this effect, we performed simulations with 800 MHz SAWs, and the results show that the DW velocity is significantly slower compared to the velocities observed with SAW frequencies ranging from 50 to 200 MHz.

In the case of the thin film with 3% anisotropy disorder (see Figure 6.3b), the DW velocity within the studied field range is notably slower compared to the thin film

6 SAW effect on domain wall dynamics

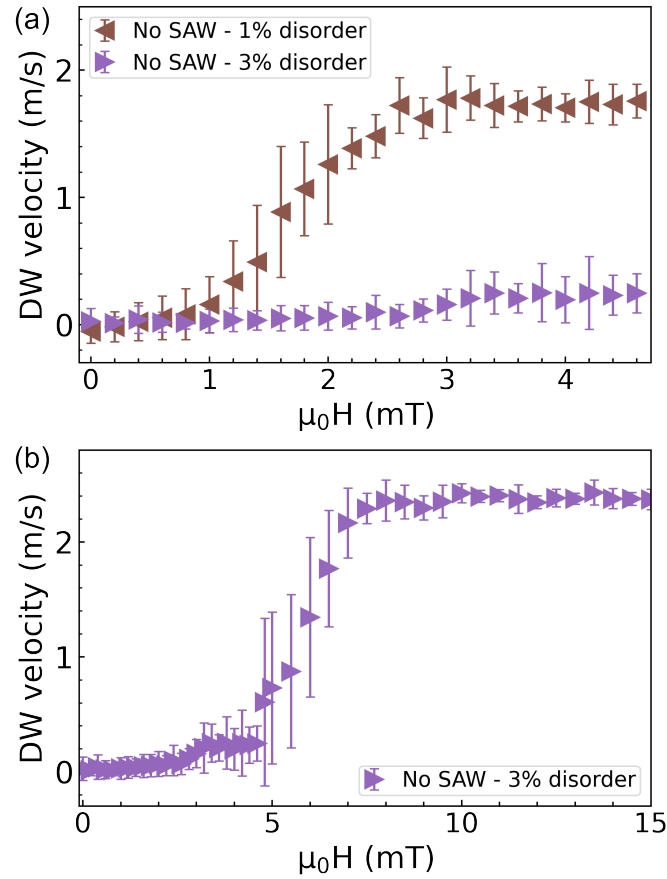


Figure 6.2: (a) DW velocity as a function of the applied external magnetic field from 0 to 4.6 mT without SAWs in thin film with 1% and 3% anisotropy disorder. (b) shows the DW velocity (y -axis, m/s) of the thin film with 3% anisotropy disorder against the applied field (x -axis, mT) from 0 to 15 mT. Error bars represent the ensemble spread of 10 simulations.

with 1% anisotropy disorder. This difference can be attributed to the higher pinning energy associated with the increased disorder level [21, 87]. Within the applied field range of 0–1 mT, the DW velocity shows minimal change due to the depinning field being at 3 mT (as shown in Figure 6.2a). However, the introduction of SAWs leads to a significant enhancement in the DW velocity, particularly with the presence of 200

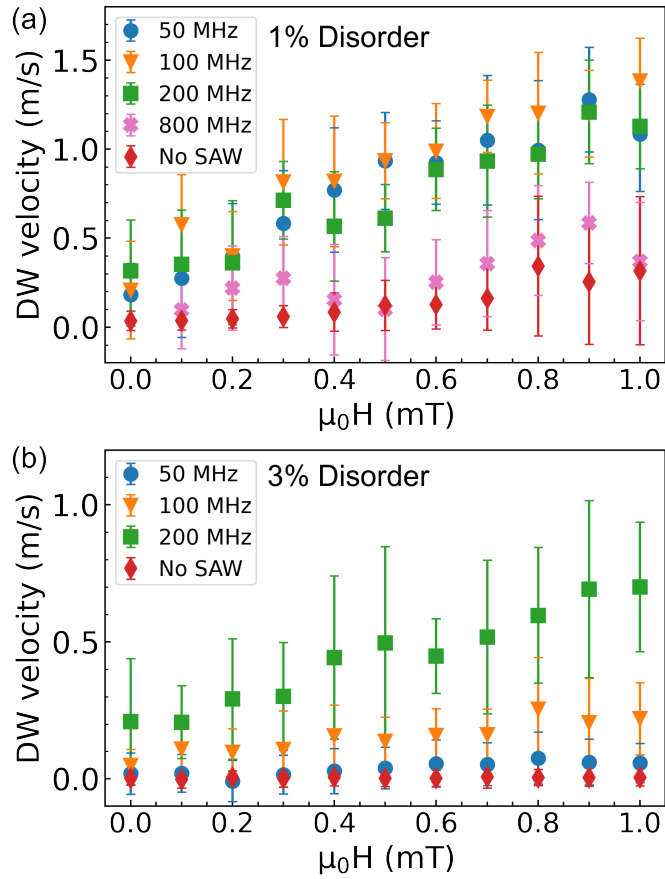


Figure 6.3: DW velocity as a function of the applied external magnetic field from 0 to 1 mT without SAWs and in the presence of SAWs with frequencies of 50, 100, and 200 MHz in thin film with (a) 1% and (b) 3% anisotropy disorder. Error bars represent the ensemble spread of 10 simulations.

MHz SAWs. Comparing the DW velocity with 1 mT alone to the DW velocity in the presence of 200 MHz SAWs, an increase from 0.004 ± 0.03 m/s to 0.7 ± 0.2 m/s is observed. Interestingly, the DW velocity increases with SAW frequency in the thin film with 3% anisotropy disorder, which is contrary to the observations made in the thin film with 1% anisotropy disorder.

6 SAW effect on domain wall dynamics

6.3.2 Domain wall depinning

To explore the influence of SAW frequency on the dynamics of DWs in thin films with varying levels of disorder, we examined the DW motion as a function of simulation time, as shown in Figure 6.4. For each value of applied field, simulation was conducted for a duration of 100 ns, followed by resetting the initial magnetisation before the start of the subsequent simulation. We begin by discussing the thin film with 1% anisotropy disorder in the absence of SAWs. From Figure 6.4a, it is evident that the depinning field of the DW is approximately 0.4 mT in the absence of SAWs. Below this field, no noticeable DW motion is observed. In Figure 6.4b, a more detailed view of DW motion at 0.5 mT is presented. Initially, in the presence of only the magnetic field, the DW moves towards the right for approximately the first 20 ns, followed by a pinning event that persists until the end of the simulation. As the field strength increases, the DW advances more until the DW is pinned at a position for which the depinning field is larger than the applied field. For instance, at external magnetic fields of 0.6, 0.7, and 0.8 mT, the pinning occurs after approximately 30, 35, and 50 ns, respectively.

We further explore the impact of SAWs on DW motion within the same thin film. Even at 0 mT applied field, a significant displacement of the DW is observed when SAWs with frequencies of 50, 100, and 200 MHz are applied. This observation suggests that the introduced SAWs effectively facilitate DW depinning from pinning sites. Moreover, regardless of the SAW frequency, the DW exhibits continuous motion at a consistent velocity, as indicated by the dashed line overlaying the DW motion curve in Figure 6.4b. The pinning events observed in the absence of SAWs are absent when SAWs are applied, as depicted in Figure 6.4a. Instead, steeper slopes in the DW displacement over time are observed with increasing external magnetic field, indicative of higher DW velocities, as illustrated in Figure 6.3a.

Next, we examine the behavior of the DW in the thin film with 3% anisotropy disorder.

6.3 Results and discussion

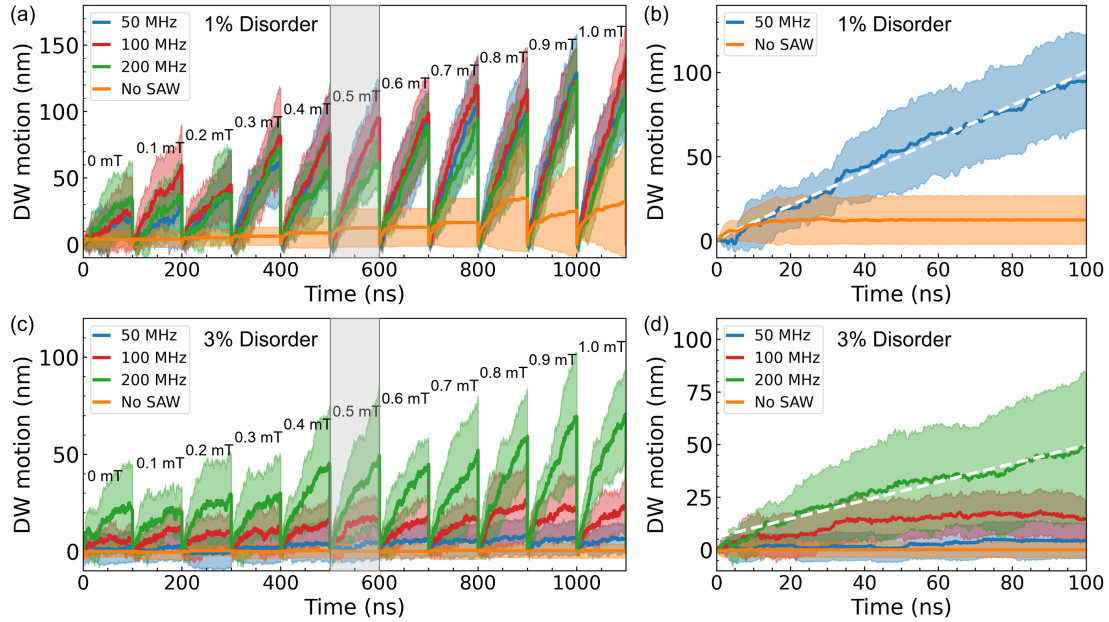


Figure 6.4: Time evolution of DW motion in thin films with (a) 1% and (c) 3% anisotropy disorder. DW motion at each applied field was performed for 100 ns, followed by returning to the initial magnetisation for the next simulation. Shaded areas represents the ensemble spread of 10 simulations. The applied field for each simulations is labeled on the Figure (b) and (d) are zoomed-in views of the enclosed areas in (a) and (c), respectively. The dash lines in (b) and (d) are the linear fits of the corresponding curves. SAWs are able to promote the DW motion within the simulation timescale.

Figure 6.4c illustrates that when only the magnetic field is applied, the pinning events are significantly more prominent compared to the thin film with 1% anisotropy disorder under the same conditions. In fact, the DW remains pinned even with a field strength of 1 mT, indicating a higher depinning field in thin films with increased anisotropy disorder. The DW motion exhibits distinct characteristics depending on the frequency of the applied SAWs. As shown in Figure 6.4c, compared to the case without SAWs,

6 SAW effect on domain wall dynamics

the overall trend of the DW motion is enhanced in the presence of SAWs within the studied frequency range. However, the frequency of the SAW significantly influences the DW motion. Figure 6.4d illustrates the DW displacement in the thin film with 3% anisotropy disorder at 0.5 mT with and without SAWs. Without SAWs, the DW hardly moves. In contrast, the presence of 50 MHz SAWs leads to an observable DW motion with a few pinning events. For example, the DW becomes pinned during the initial 10 ns, followed by motion for a short period until the next pinning event at 20 ns. With an increase in SAW frequency to 100 MHz, more significant DW motion is observed, accompanied by additional pinning events. Notably, when the SAW frequency reaches 200 MHz, continuous DW motion with minimal pinning effects occurs (as indicated by the dashed line in Figure 6.4d). In fact, even at 0 mT, 200 MHz SAWs facilitate the DW depinning process, while 50 MHz SAWs exhibit limited effects on DW motion, even at 1 mT. These observations suggest that SAWs with higher frequencies exert a stronger influence on DW motion in thin films with higher levels of anisotropy disorder. It is worth noting that the DW velocity, even in the presence of SAWs, is slower compared to the thin film with lower anisotropy disorder. This is attributed to the higher energy required to depin the DW in thin films with increased anisotropy disorder. Note that within the first five complete cycles (100 ns for 50 MHz, 50 ns for 100 MHz, and 20 ns for 200 MHz), DW depins from the pinning sites and shows a continuous motion in the presence of the SAWs with 100 and 200 MHz. This observation confirms that SAWs with five complete cycles offer sufficient opportunities for depinning, thereby validating the chosen simulation duration.

6.3.3 Formation of vertical Bloch lines

To gain insight into the DW depinning process, we examine the magnetisation configuration under the influence of the magnetic field alone and in the presence of SAWs. At 10 ns into the simulation, the magnetisation configuration is captured and presen-

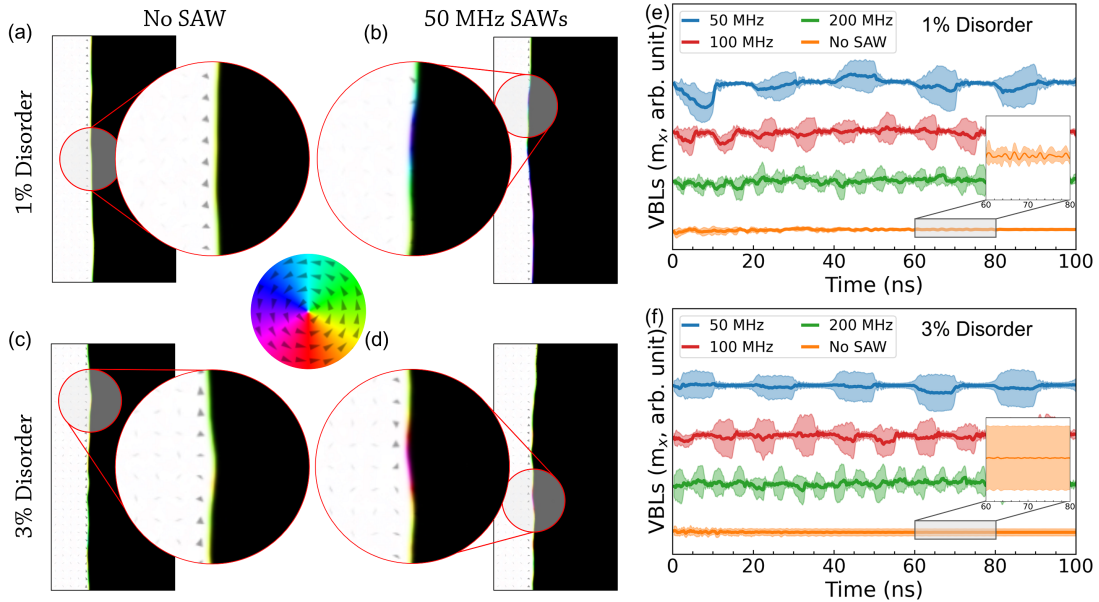


Figure 6.5: Snapshots of the magnetisation configuration under an applied field of 0.5 mT at 10 ns in thin films with (a) 1% disorder without SAW, (b) 1% disorder with 50 MHz SAWs, (c) 3% disorder without SAW, and (d) 3% disorder with SAWs. Inset graphs in (a)–(d) represent the enlarged magnetisation configuration of the corresponding enclosed area. The colour code for the in-plane magnetisation component is shown by a colour wheel. The number of VBLs against the simulation time in thin film with (e) 1% and (f) 3% anisotropy disorder under an applied field of 0.5 mT without SAWs and in the presence of SAWs with frequencies of 50, 100, and 200 MHz. Inset graphs in (e) and (f) are zoomed-in view of VBLs number against simulation time (60–80 ns) without SAWs (two graphs share the same scale). Shaded areas indicate the ensemble spread of 10 simulations. The number of VBLs (y -axis) is shifted for clarity of changes.

6 SAW effect on domain wall dynamics

ted in Figure 6.5a–d. In the thin film with 1% anisotropy disorder and without SAWs at 0.5 mT, the DW moves steadily and coherently while maintaining its structure. A smooth DW with no significant curvature is observed, depicted as a light green line separating the left and right domains in Figure 6.5a. However, in the presence of SAWs, the DW exhibits curvatures and Bloch segments with opposite orientation (up/down) separated by VBLs as shown in Figure 6.5b. The different coloured sections indicate the introduction of additional spin configurations in the wall structure induced by the SAWs [87, 89, 90].

In our simulations, the DW exhibits a Bloch wall structure, where the magnetisation is primarily oriented in the “up” or “down” direction (along the y -axis). The VBLs in our system, on the other hand, are oriented in the “left” or “right” direction (along the x -axis). Thus, the additional spin structures introduced by the VBLs can be represented by the magnetisation component along the x -axis (m_x). It is important to note that the “number of VBLs” in this study is not an absolute quantity; rather, we utilised m_x as a representation of the presence and density of VBLs within the system. The number of VBLs is plotted against simulation time in Figure 6.5e and f. In the thin film with 1% anisotropy disorder and the application of the magnetic field alone, the number of VBLs shows minimal change, indicating rare occurrence of spin rotations (inset graph in Figure 6.5e). However, when SAWs are applied, the number of VBLs exhibits periodic fluctuations, as shown in Figure 6.5e. The period of these fluctuations corresponds to the frequencies of the applied SAWs. For instance, SAWs with frequencies of 50, 100, and 200 MHz exhibit periodicities of approximately 20, 10, and 5 ns, respectively. The periodic variation in the number of VBLs with the SAW frequency arises from the magnetoelastic coupling effect. When SAWs are applied, strain is introduced to the magnetic thin film, resulting in the emergence of an effective magnetic field. This effective magnetic field plays a crucial role in both the nucleation and annihilation of VBLs, as well as influencing the motion of the DW

and the VBLs within the DW, contributing to their dynamics.

In the magnetisation configuration of the thin film with 3% anisotropy disorder at 0.5 mT, the DW exhibits greater curvatures (see Figure 6.5c) and a larger number of VBLs (see Figure 6.5f) compared to the thin film with 1% anisotropy disorder under the same conditions. The inset graphs in Figure 6.5e and f (same scale) provide a closer look at the number of VBLs when only the magnetic field is applied within the range of 60 to 80 ns. The ensemble spread of VBLs in the thin film with 3% anisotropy disorder is approximately 2.5 times wider than that in the thin film with 1% anisotropy disorder, indicating a greater occurrence of spin rotations within the DW in the thin film with 3% anisotropy disorder. This can be attributed to the fact that the magnetic field alone is strong enough to induce DW motion and maintain DW structure in the thin film with 1% anisotropy disorder, thereby avoiding the significant formation of VBLs. However, in the thin film with 3% anisotropy disorder, the magnetic field is insufficient to enable the DW to overcome the local energy potential [90]. Consequently, the magnetic field introduces spin rotations within the DW, contributing to the broader ensemble spread of VBLs. Similar to the DW in the thin film with 1% anisotropy disorder, the number of VBLs in the thin film with 3% anisotropy disorder also undergoes periodic changes with the SAW frequency. The fluctuation behavior of VBLs in relation to the SAW frequencies is observed consistently across thin films and various applied fields.

The introduction of SAWs induces spin rotation in the DW, resulting in a smoothing of the energy landscape within the thin film. This phenomenon leads to enhanced DW motion. It is instructive to compare the effect of SAWs with the effect of thermal fluctuations on DW motion. To do this, we separately examined the effects of SAWs and temperature on DW motion [138, 139]. Figure 6.6a displays the time evolution of the DW at both 0 K and 300 K in a thin film with 3% anisotropy disorder. In the absence of SAWs, the presence of thermal fluctuations at 300 K significantly enhances

6 SAW effect on domain wall dynamics

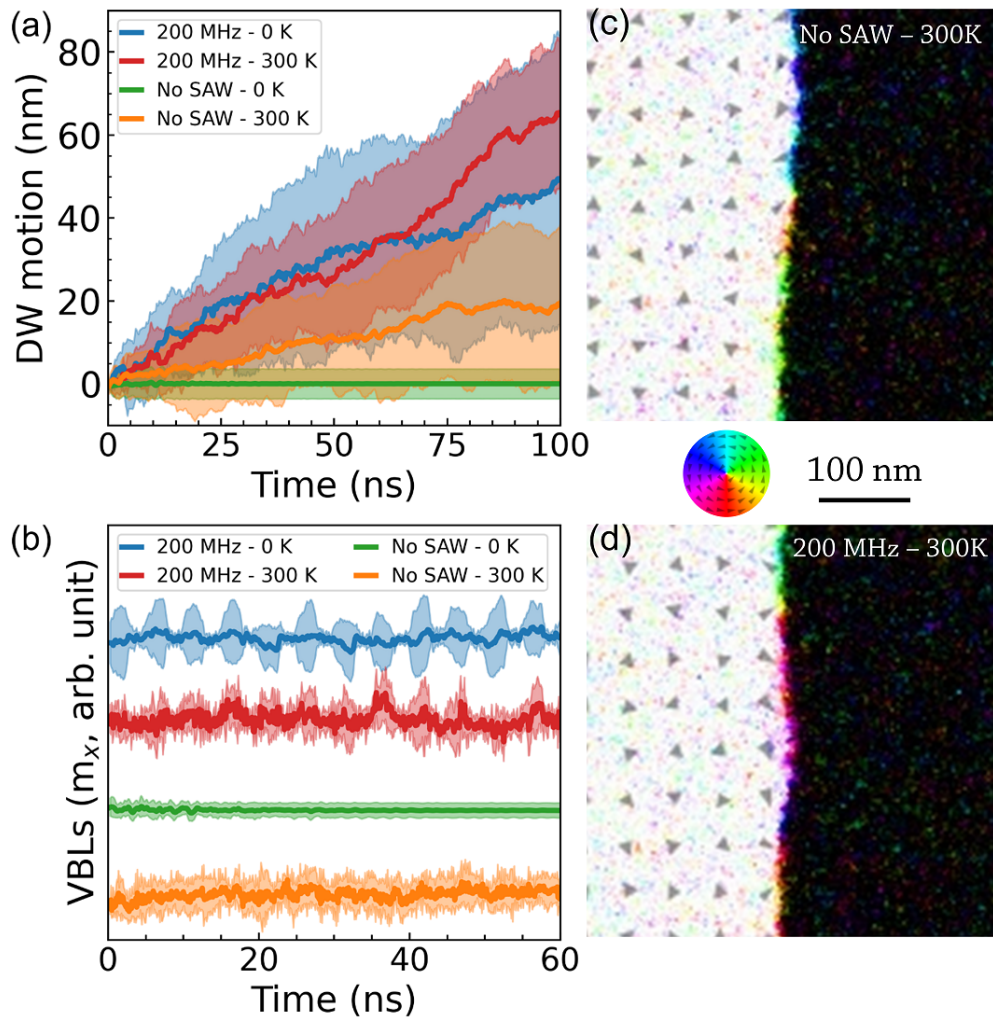


Figure 6.6: (a) DW motion and (b) VBLs plotted against simulation time both without SAWs and with 200 MHz SAWs at 0 and 300 K. Snapshots of the magnetisation configuration at 300 K at 10 ns (c) without SAWs and (d) with 200 MHz SAWs. The simulations are conducted in the thin film with 3% disorder under an applied field of 0.6 mT. The colour code for the in-plane magnetisation component is shown by a colour wheel. Shaded areas indicate the ensemble spread of 10 simulations. The number of VBLs (y -axis) is shifted for clarity of changes.

6.3 Results and discussion

DW motion compared to the motion observed at 0 K. This enhancement is also evident through the presence of multiple VBLs at 300 K, as depicted in Figure 6.6c, and the variation in the number of VBLs over time, illustrated in Figure 6.6b. The number of VBLs is notably higher than in simulations conducted at 0 K without SAWs, although the changes in the number of VBLs occur randomly over time. In the presence of 200 MHz SAWs at 300 K, the DW also contains multiple VBLs, as shown in Figure 6.6d. However, in this case, the changes in the number of VBLs over time have a periodicity that aligns with the SAW frequency. Moreover, there is an additional level of randomness introduced by thermal fluctuations when compared to the scenario with 200 MHz SAWs at 0 K, as depicted in Figure 6.6c. The introduction of SAWs in magnetic thin films creates an effective field with the same periodicity as the SAW frequency. This effective field induces spin rotation, leading to the formation of VBLs within the DW. The spin rotation caused by SAWs enhances the possibility of DW depinning by smoothing the energy landscape of the thin films, similar to the effect of thermal fluctuation [138]. It is important to note that the spin rotation induced by SAWs exhibits the same frequency as the SAW, in contrast to the randomly distributed nature of thermal fluctuation. This coherent spin rotation induced by SAWs introduces a more controlled and synchronised influence on the DW dynamics, offering potential advantages for precise manipulation and control of DW motion in magnetic thin films.

The SAW-induced effective field and spin rotation, are critical in modulating the local energy landscape. Fig. 6.7a shows a schematic of a DW containing a VBL with a curvature separating the left and right domain. Note that only external magnetic field (\mathbf{H}_{ext}) and effective fields generated by pinning potential (\mathbf{H}_{pin}) and SAWs (\mathbf{H}_{me}) are demonstrated in the sketch. When only external magnetic field applied is applied and no SAW, the magnetic moment mainly experiences two torques generated by external magnetic field and local effective pinning field, respectively. In the simulation,

6 SAW effect on domain wall dynamics

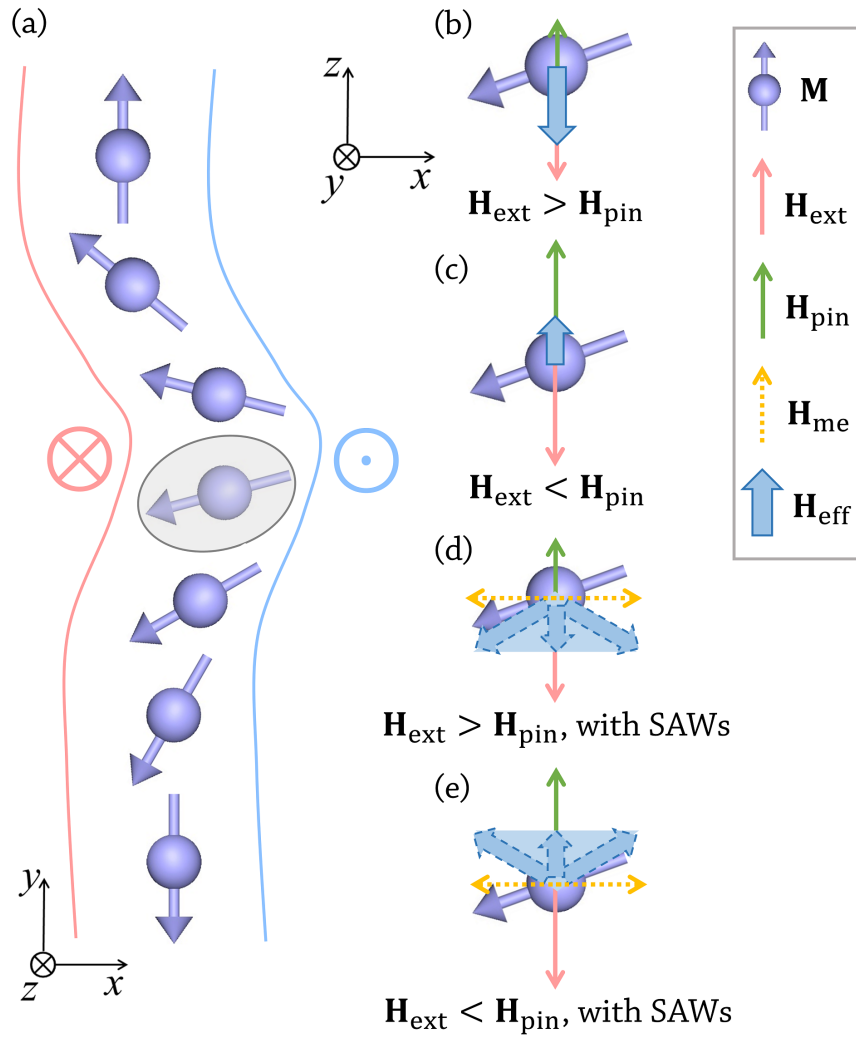


Figure 6.7: (a) The left and right domains are pointing “in” and “out” of the paper, respectively, separated by a DW with VBLs. The circled spin is used to analyse the effective fields under different conditions in (b)–(e). (b) $H_{ext} > H_{pin}$ without SAW. (c) $H_{ext} < H_{pin}$ without SAW. (d) $H_{ext} > H_{pin}$ with SAWs. (e) $H_{ext} < H_{pin}$ with SAWs.

the pinning is introduced by the magnetic anisotropy in out-of-plane direction (K_u). Therefore, only pinning in the z -axis is taken into consideration. When \mathbf{H}_{ext} is larger than \mathbf{H}_{pin} (as shown in Fig. 6.7b), the magnetic moment aligns to the net effective field resulting in the DW motion towards the right. However, when \mathbf{H}_{ext} is smaller than \mathbf{H}_{pin} (as shown in Fig. 6.7c), the DW is pinned at the local pinning site since the net effective field is smaller than the local effective pinning field. Owing to the magnetoelastic coupling effect, the dynamic strain induced by SAWs generates a dynamic effective field (as shown in Fig. 6.7d and e). This effective field exerts an extra dynamic torque on the magnetic moment within the DW (in our simulation, only in-plane strain is taken into consideration). The SAW-induced dynamic effective field can promote diverse spin configurations within the DW (as evidenced by the formation of VBLs). Under certain configurations together with other effective fields (such as exchange interaction), the DW can overcome these local energy barriers. Hence, SAWs not only generate an effective field for DW motion but also induce spin rotations and VBLs, facilitating the most conducive spin configurations for DW depinning.

The SAW-induced spin rotation has two possible distinct effects on DW motion: (i) The spin rotation increases the likelihood of DW depinning from pinning sites, thereby promoting DW motion. (ii) The presence of the SAWs drives the DW motion into a non-linear regime, where the spin rotation leads to enhanced energy dissipation at the DW due to magnetic damping. These two effects have contrasting consequences on DW motion. On one hand, they can increase the DW velocity by enhancing the probability of depinning. On the other hand, the energy dissipation can limit the energy available to enhance DW motion. Higher SAW frequencies correspond to higher spin rotation frequencies, which, in turn, lead to increased energy dissipation at the DW. In the thin film with 3% disorder, the effect (i) is more significant, resulting in enhanced DW velocity and depinning with increasing SAW frequency. In contrast,

6 SAW effect on domain wall dynamics

the thin film with 1% disorder experiences a greater impact from effect (ii), leading to a smaller DW velocity in the presence of SAWs with higher frequencies. At low magnetic fields, material defects or grain boundaries act as potential wells, serving as pinning sites for the motion of the DW [21, 22, 87]. SAWs in our thin films introduce energy fluctuations with the same frequency as the SAWs, which promote the depinning of the DW from these pinning sites [133, 139, 140]. The implication of effect (ii) is a hypothesis inferred from our simulation data; however, it necessitates additional examination to confirm its validity.

6.4 Summary

In summary, we investigated the impact of SAW frequency (50, 100, and 200 MHz) on the DW motion in thin films with different levels of anisotropy disorder through micromagnetic simulations. The results demonstrated that SAWs enhance DW velocity by promoting the depinning of DWs from pinning sites through SAW-induced spin rotation, which was consistently observed across all cases studied. The spin rotation not only increased the likelihood of DW depinning but also contributed to energy dissipation at the DW. In the thin film with 3% anisotropy disorder, the DW velocity increased with the SAW frequency, primarily due to the amplifying effect of spin rotation, which enhanced the probability of DW depinning. Conversely, in the thin film with 1% anisotropy disorder, the DW velocity decreased with increasing SAW frequency due to the significant SAW-induced spin rotation, leading to pronounced energy dissipation at the DWs as the primary factor influencing DW motion. These findings provide valuable insights into the intricate interplay between SAWs, spin rotation, and DW dynamics, highlighting the crucial role of anisotropy disorder in governing the response of DWs to SAWs.

CHAPTER 7

SAW effect on skyrmion dynamics

7.1 Introduction

Magnetic skyrmions, which are topologically protected particle-like magnetic structures, show significant potential in applications including in data storage and processing devices [100, 141]. Skyrmions in thin films can be manipulated by spin-polarised current via STT or SOT owing to the large SOC with heavy metals [142–146]. However, these methods require a high current density, which can cause Joule heating thereby wasting energy and affecting the stability of skyrmions. In addition, skyrmions typically show both longitudinal and transverse motion owing to the skyrmion Hall effect, which can cause the annihilation of skyrmions at device edges, thus complicating device realisations [100, 146, 147].

Typically, the stability of skyrmions in thin films with PMA is a result of the balance between the magnetic anisotropy and the interfacial DMI induced by the broken interfacial inversion symmetry [131, 148–150]. To avoid Joule heating, one can modify the anisotropy of thin films using strain to control magnetisation [53, 151–153]. For instance, Wang *et al.* created skyrmions in Pt/Co/Ta multilayer nano-dot systems using an electrical field-induced strain [154], while Ba *et al.* demonstrated the creation, reversible deformation, and annihilation of skyrmions in a Pt/Co/Ta multilayer thin film using strain by applying an electrical field to a PMN-PT substrate [44]. The dynamic strain induced by SAWs has also been suggested as an attractive approach to control thin film magnetisation [11–14, 17, 30, 70, 71, 155]. SAW control of skyrmions has a number of potential advantages. SAWs can be exerted by voltage instead of current making it attractive from the energy-efficiency perspective, while SAWs can propagate over distances of several millimetres with very little power loss. This allows one pair of electrodes to control multiple devices. Besides, pinning sites can be created by electrodes remotely, which potentially allows one to control skyrmions precisely without complex design.

Nepal *et al.* theoretically demonstrated the dynamics of skyrmion motion under the

influence of standing SAWs as reported in their study [19]. Their findings indicate that standing SAWs are capable of creating pinning sites for skyrmions, with the driving force being proportional to the strain gradient. In the initial section of this chapter, we replicate their investigation on the formation of pinning sites induced by standing SAWs. We then explore the influence of travelling SAWs and orthogonal SAWs – created by the transverse standing and longitudinal travelling SAWs – on skyrmion trajectories.

7.2 Model and computational details

Figure 7.1a shows the schematic diagram of the proposed device that can be implemented by preparing a Co/Pt PMA thin film (with dimensions of $1024 \times 256 \times 1$ nm³ employing repeated boundary conditions) onto a 128° Y-cut LiNbO₃ substrate surrounded by two pairs of IDTs (labelled as IDT1 to IDT4). As shown in Figure 7.1b, the origin of the thin film geometry is located at its centre, with x and y correspond to the longitudinal and transverse directions of the thin film, respectively. The electrode spacing of the first (IDT1 and IDT2) and second (IDT3 and IDT4) pair of IDTs was set as 128 nm and 16 nm, respectively, producing SAWs with wavelength λ_1 (see Figure 7.1c) and λ_2 (see Figure 7.1d) of 512 nm and 64 nm, respectively.

SAWs with different propagation modes can be achieved by applying rf signals to one or more IDTs: travelling SAWs propagating in x direction can be generated by applying rf signals to IDT1; standing SAWs can be formed by applying rf signals to IDT1 and IDT2 simultaneously; while orthogonal SAWs consisting of horizontal travelling SAWs and transverse standing SAWs, can be formed by applying rf signals to IDT1, IDT3 and IDT4 at the same time. Néel skyrmions, which are common type of skyrmions found in thin films with PMA, were initialised and relaxed at different positions in the thin film with PMA in order to study the SAW effect on their motion

7 SAW effect on skyrmion dynamics

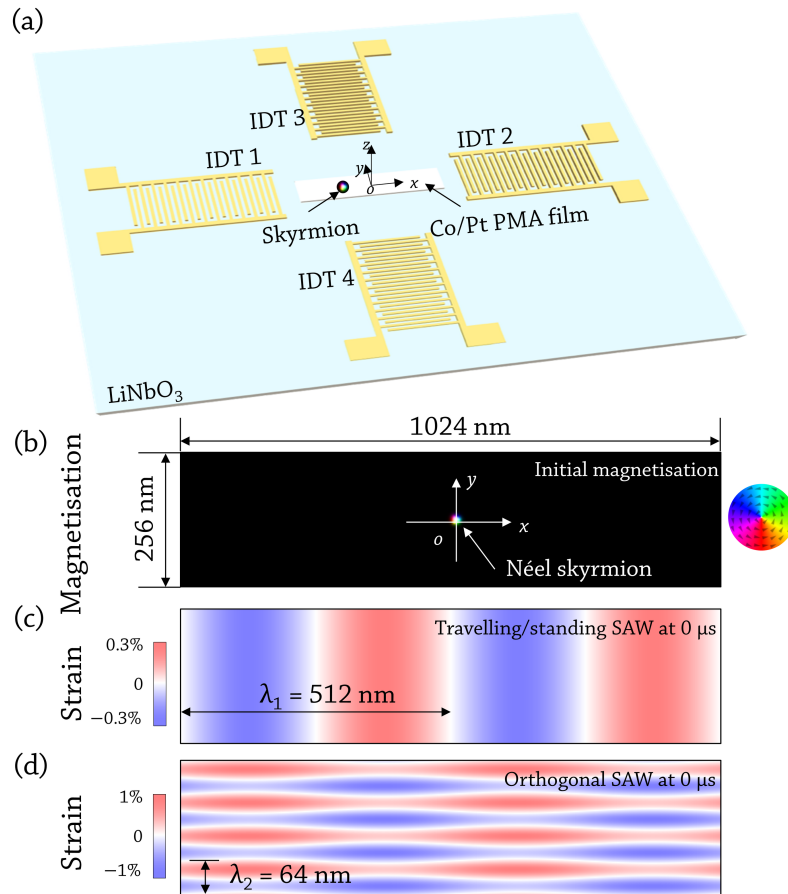


Figure 7.1: (a) Diagram of the proposed device. A Néel skyrmion is initialised in a PMA thin film grown onto a LiNbO₃ substrate. The thin film is surrounded by two pairs of IDTs (IDT1 to IDT4) used to generate SAWs in different modalities. (b) An example of the initial magnetisation. A Néel skyrmion is initialised and relaxed in the thin film. (c) Strain spatial profile of travelling SAWs and standing SAWs at 0 μs. (d) Spatial strain profile of orthogonal SAWs (longitudinal travelling SAWs and transverse standing SAWs) at 0 μs. The colour code for the in-plane magnetisation component is shown by a colour wheel.

(Figure 7.1b). The strain amplitude of standing SAWs and travelling SAWs was set as 0.3%. As for orthogonal SAWs, amplitudes of the longitudinal travelling SAWs and transverse standing SAWs were 0.3% and 0.7%, respectively. Figure 7.1c and d show the spatial strain profile of travelling SAWs, standing SAWs and orthogonal SAW at 0 μ s, respectively.

Micromagnetic simulations were performed using Mumax3 [112, 156, 157], based on the LLG equation (Equation 2.3). The magnetoelastic energy density can be expressed as Equation 2.17. The material parameters are set corresponding to Co/Pt thin film as follows [117, 158]: saturation magnetisation $M_s = 5.8 \times 10^5$ A/m, exchange constant $A_{\text{exch}} = 1.5 \times 10^{-11}$ J/m, anisotropy constant $K_u = 8 \times 10^5$ J/m³, interfacial DMI strength $D = 3 \times 10^{-3}$ J/m², magnetoelastic coupling coefficient $B_1 = 2 \times 10^7$ J/m³. The Gilbert damping constant of Co/Pt multilayer is reported in the range of 0.02–0.1 [159, 160]. To resolve high frequency magnetisation dynamics and to enhance the skyrmion motion, α value of 0.01 was chosen [65, 150]. The standing SAWs and travelling SAWs were implemented using Equation 3.3 and Equation 3.4, respectively.

7.3 Results and discussions

7.3.1 Impact of standing SAWs on skyrmion motion

We firstly studied the skyrmion motion driven by standing SAWs, and in particular the effect of nodes and anti-nodes of standing SAWs on skyrmion motion. The dynamic strain waves form a strain gradient, which periodically changes between nodes and anti-nodes. Owing to the magnetoelastic coupling effect, the strain gradient provides a driving force for skyrmion motion in the x direction. However, this strain gradient vanishes at the anti-nodes of standing SAWs. The induced strain gradient pushes the skyrmion moving towards the anti-nodes, with pinning therefore occurring at the anti-nodes. This behaviour is shown in Figure 7.2a. Skyrmions were initialised at

7 SAW effect on skyrmion dynamics

different x positions along the thin film (relative to the origin). We observed skyrmions moving towards the nearest anti-nodes from their initial position. However, skyrmions were pinned without any motion in both x and y directions if they were initialised at anti-nodes. Figure 7.2d and e show examples of skyrmion motion from initial positions (10 nm and -10 nm in x direction) to final positions at 8 μ s. We also observed skyrmion Hall-like motion in the y direction since skyrmions are rotationally symmetric magnetisation textures (Figure 7.2b).

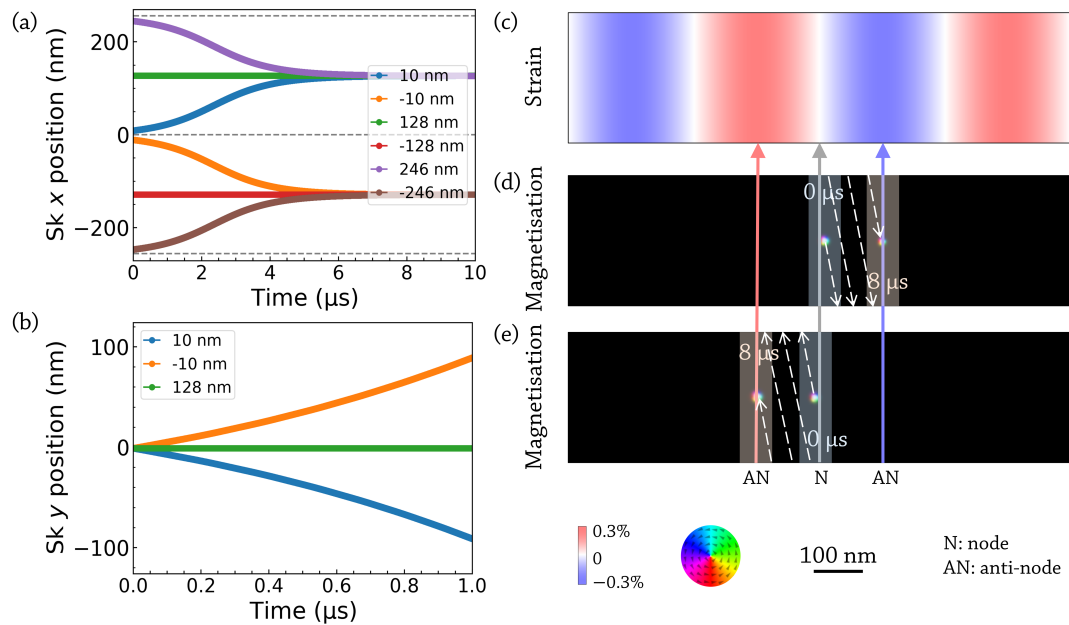


Figure 7.2: Translation of skyrmion in (a) x and (b) y directions driven by standing SAWs. Numbers in the legend indicate initial x positions of skyrmions relative to the origin. (c) Spatial strain profile of standing SAWs at 0 μ s. Examples of the skyrmion initial and final positions driven by standing SAWs: (d) skyrmion initialised at -10 nm and (e) 10 nm along x direction relative to the origin. “N” and “AN” denote the node and anti-node, respectively. The colour code for the in-plane magnetisation component is shown by a colour wheel.

7.3.2 Impact of travelling SAWs on skyrmion motion

Secondly, we studied the skyrmion motion driven by travelling SAWs. Figure 7.3a shows the translation of skyrmions in the x direction driven by travelling SAWs. Unlike the skyrmion motion driven by standing SAWs, regardless of initial positions of skyrmions (10 nm, 128 nm, and 246 nm along the x direction), skyrmions move continuously in the x direction at a speed of 2.40 cm/s without any pinning with the application of travelling SAWs (Figure 7.3a). This is because skyrmions experience nodes and anti-nodes at all positions with the application of travelling SAWs, which provide a dynamic but continuous strain gradient (driving force). Skyrmions also exhibit Hall-like motion in the y direction (see the insert graph in Figure 7.3a). Figure 7.3b show an example of skyrmion position changes with time driven by travelling SAWs. The velocity at which skyrmions are driven by travelling SAWs is substantially less than the speed of the SAWs themselves, which is around 4000 m/s. This implies that multiple wave periods are required to induce skyrmion motion.

7.3.3 Impact of orthogonal SAWs on skyrmion motion

We then demonstrate the precise transport of a single skyrmion using orthogonal SAWs, which are formed by combining longitudinal travelling SAWs and transverse standing SAWs. With this configuration, we are able to move skyrmions continuously in the x direction using travelling SAWs and also to create pinning “channels” using the anti-nodes of the standing SAWs along the y direction to suppress the skyrmion transverse motion. In this simulation, the wavelengths and strain amplitudes of travelling SAWs and standing SAWs were set as 512 nm and 0.3%, and 64 nm and 0.7%, respectively (see Figure 7.1d). Figure 7.4a shows the translation of a skyrmion. Skyrmion moves continuously in the x direction with a very limited motion of ~ 1 nm in the y direction at the beginning, when the skyrmion tries to move

7 SAW effect on skyrmion dynamics

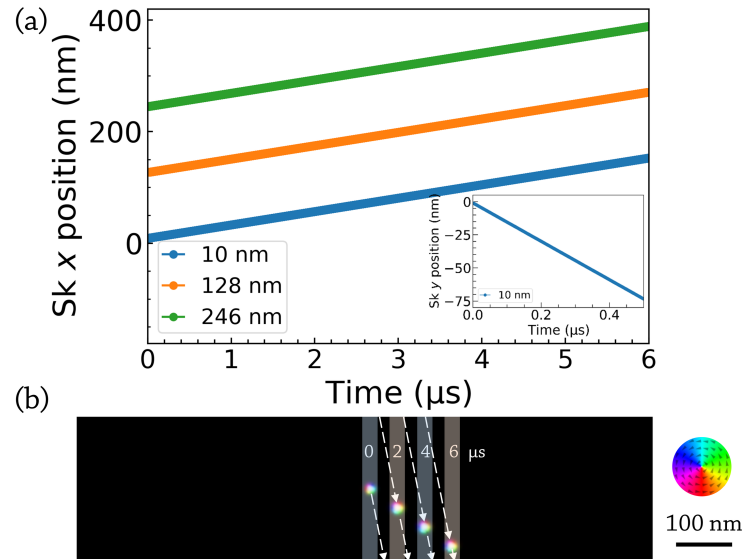


Figure 7.3: (a) Translation of skyrmion in the x direction driven by travelling SAWs. Numbers in the legend indicate the initial x positions of skyrmions relative to the origin. The insert graph shows the skyrmion motion in the y direction during the first $0.5 \mu\text{s}$. (b) Snapshots of skyrmion motion from 0 to $6.0 \mu\text{s}$. The arrows indicate the skyrmion moving direction. The colour code for the in-plane magnetisation component is shown by a colour wheel.

from its initial position towards the pinning channel that standing SAWs create. Note that the skyrmion velocity significantly increases to 38.64 cm/s compared to that of travelling SAW-induced skyrmion motion (2.40 cm/s). This is because the standing SAWs induced force contributes to the longitudinal motion [19].

To understand the influence of the amplitude of standing and travelling SAWs on skyrmion velocity, we simulated skyrmion motion driven by orthogonal SAWs with varying configurations. The amplitude of the standing SAW was maintained at 0.7% , while the amplitude of the travelling SAW was varied from 0.1% to 0.55% . It was observed that the skyrmion is pinned in the transverse direction when the travelling SAW amplitude is at most 0.45% . The skyrmion velocity significantly increases from

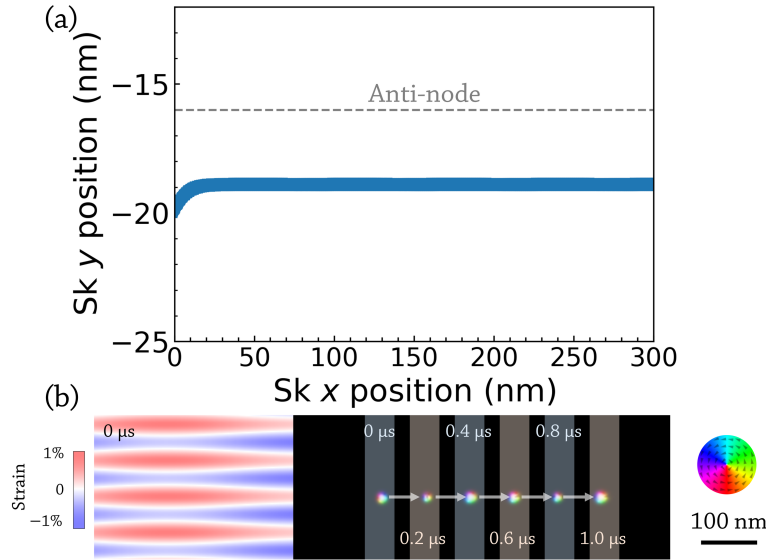


Figure 7.4: (a) Translation of skyrmion in x and y directions driven by orthogonal SAWs. (b) Left-hand side of the figure shows the spatial strain profile of orthogonal SAWs at $0 \mu\text{s}$. Right-hand side of the figure shows the snapshots of the skyrmion motion from 0 to $1.0 \mu\text{s}$. The arrows indicate the direction of the skyrmion moving direction, which is in line with the anti-node of standing SAWs in orthogonal SAWs. The colour code for the in-plane magnetisation component is shown by a colour wheel.

0.01 m/s to 0.86 m/s as the travelling SAW amplitude rises from 0.1% to 0.45% (see Figure 7.5c). Furthermore, we set the travelling SAW amplitude to 0.3% and altered the standing SAW amplitude from 0.3% to 1.2% . The transverse motion of the skyrmion is effectively restrained when the standing SAW amplitude exceeds 0.5% (see Figure 7.5d). A slight decrease in skyrmion velocity is observed with an increase in standing SAW amplitude (see Figure 7.5e). In other words, the strain amplitude of the standing SAW must be greater than that of the travelling SAWs to provide sufficient pinning energy that confines the skyrmion motion in the x direction. Skyrmion motion trajectory can be attributed to the balance of forces acting on the skyrmion (as depicted in Figure 7.5). In the following analysis, we will use $-x$, $+x$,

7 SAW effect on skyrmion dynamics

$-y$, and $+y$ to denote the directions as left, right, down, and up relative to the origin (centre of the simulation region), respectively. The travelling SAW generates a force F_T that moves the skyrmion longitudinally in the same direction of the travelling SAW ($+x$). At the same time, the travelling SAW also induces a Magnus force F_{T-Mag} perpendicular to the F_T ($-y$) due to the skyrmion Hall effect. Similarly, the standing SAW exerts a driving force F_S along the $+y$ axis and a Magnus force F_{S-Mag} in $-x$ axis, orthogonal to each other. Therefore, skyrmion velocity decreases with increasing amplitude of the standing SAW, as shown in Figure 7.5e. There is also dissipative force F_{Dis} at the $-x$ direction due to damping. The net force of the above mentioned forces determines the motion of the skyrmion. To suppress the skyrmion motion in the transverse direction, F_S needs to be equal to the F_{T-Mag} .

7.3.4 Multichannel skyrmion racetrack

Finally, we proposed a multi-channel skyrmion racetrack obtained using orthogonal SAWs. In this simulation, we use the same orthogonal SAW property as above (i.e. the wavelengths and strain amplitudes of standing SAWs and travelling SAWs, which together form orthogonal SAWs, are 512 nm and 0.3%, and 64 nm and 0.7%, respectively) but with a larger space comprising $2048 \times 1024 \times 1$ nm³. We initialised four skyrmions (Sk1 to Sk4 in Figure 7.6) randomly along transverse direction but with the same longitudinal position. As shown in Figure 7.6, skyrmions are transported different distances during the first 0.3 μ s. This is owing to the fact that standing SAWs push skyrmions towards their nearest anti-nodes. This means that standing SAWs provide a driving force with the same/opposite direction as/to travelling SAWs depending their positions relative to the anti-nodes (see Figure 7.2a). From 0.3 to 2.1 μ s, the velocity of all skyrmions remains the same. This is because the driving force is the same for all skyrmions after they arrive the pinning channel. With this design, one can create multiple channels to transport skyrmions without skyrmion interaction

7.3 Results and discussions

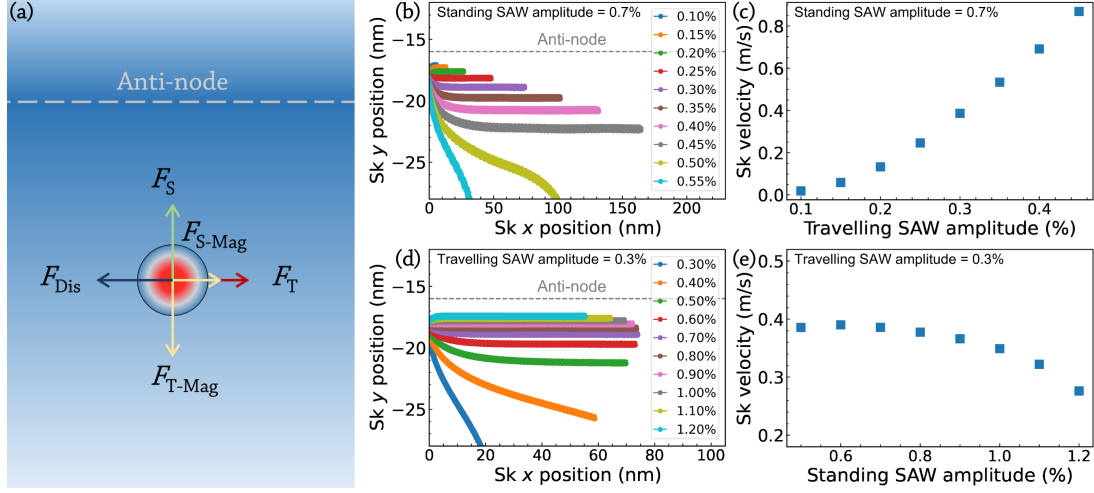


Figure 7.5: (a) Illustration of forces acting on a skyrmion induced by orthogonal SAWs. The forces include the driving force (F_T), Magnus force (F_{T-Mag}) from the travelling SAW, as well as the driving force (F_S), Magnus force (F_{S-Mag}) from the standing SAW, and dissipative force (F_{Dis}) due to damping. (b) Skyrmion trajectories under a fixed standing SAW amplitude of 0.7%, with varying travelling SAW amplitudes from 0.1% to 0.55%. (c) Corresponding skyrmion velocities for varying travelling SAW amplitudes. (d) Skyrmion trajectories under a fixed travelling SAW amplitude of 0.3%, with varying standing SAW amplitudes from 0.3% to 1.2%. (e) Corresponding skyrmion velocities for varying standing SAW amplitudes.

to increase the transporting data density. The width and density of the channel can be determined by the wavelength of standing SAWs that forms orthogonal SAWs.

The results presented above provide a proof-of-concept for purely SAW-driven skyrmion motion. However, several questions remain to be explored. Notably, some material parameters employed in this study exceed those achievable in experimental settings. Additionally, the SAW parameters, including wavelength and amplitude, that facilitate skyrmion motion require adjustment to align with experimentally viable scales for practical device realisation. Furthermore, the simulations were conducted under

7 SAW effect on skyrmion dynamics

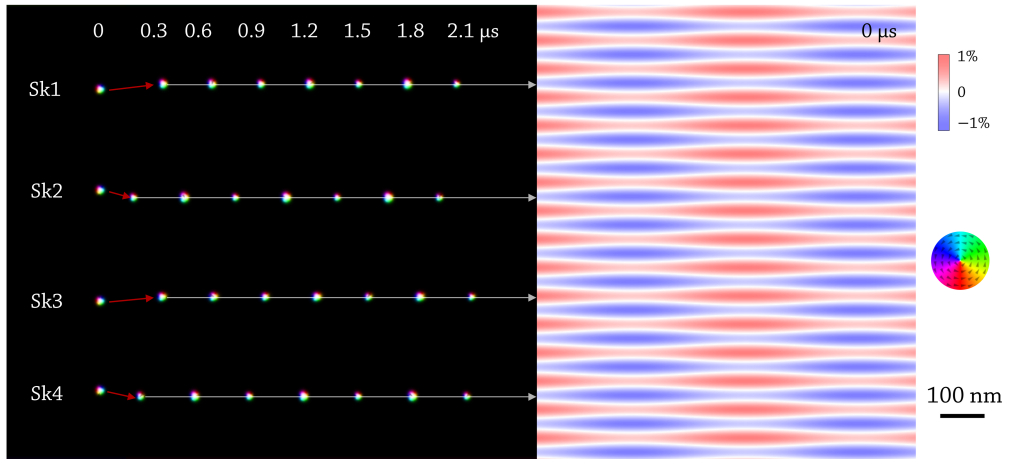


Figure 7.6: Skyrmion trajectories in a multichannel racetrack with orthogonal SAWs. The left side displays the motion of four skyrmions (Sk1 to Sk4) in a multichannel racetrack, influenced by orthogonal SAWs. The skyrmions are initially positioned randomly along the y -axis but at an identical x -coordinate. The time elapsed is denoted above the graph in μs , and the arrows indicate the direction of skyrmion motion, aligning with the anti-nodes of the standing SAW. On the right side, the spatial strain profile is shown at time $0 \mu\text{s}$, and the color wheel represents the color code for the in-plane magnetisation component.

ideal conditions, devoid of temperature fluctuations and disorder, raising the need to investigate how skyrmions respond to these external variables.

7.4 Summary

To summarise, we demonstrated the skyrmion motion by SAWs with different modalities. Skyrmions were moved by standing SAWs and travelling SAWs in both longit-

7.4 Summary

udinal and transverse directions due to the SAW-induced strain gradient. Standing SAWs created pinning sites at their anti-nodes, whereas travelling SAWs provided a constant driving force to move skyrmions continuously. By combining longitudinal travelling SAWs and transverse standing SAWs, we demonstrated the precise transport of skyrmions in the longitudinal direction without transverse motion by orthogonal SAWs. These results suggest the possibility of multi-channel skyrmion racetrack memory/logic devices using SAWs.

7 SAW effect on skyrmion dynamics

CHAPTER 8

Conclusions and outlook

8 Conclusions and outlook

Magnetic spin structures, such as domain wall (DW) and skyrmion, in thin films with perpendicular magnetic anisotropy (PMA) hold significant promise for technological advancements in spintronics, particularly in applications like magnetic racetrack memory and logic devices. The utilisation of surface acoustic waves (SAWs) presents a novel and energy-efficient approach to control magnetic spin structures through the magnetoelastic coupling effect. This thesis offers a comprehensive investigation of the interactions between SAWs and magnetic thin films with PMA, employing both experimental and micromagnetic techniques. The primary objective is to gain an in-depth understanding of the effects of SAWs on magnetisation dynamics, with a specific focus on magnetic spin structures like DWs and skyrmions.

8.1 Conclusions

Chapter 4 provided insights into the effect of the standing SAWs on the coercivity, magnetisation switching, and domain patterns in Ta/Pt/Co/Ir/Ta thin films with PMA. The results indicated that the coercivity of the thin film decreased by up to 21% in the presence of the standing SAWs at 93 MHz with a power of 22.5 dBm. The magnetisation reversal speed also significantly increased by a factor of 11. Due to the difference in strain distribution, standing SAWs locally lowered the domain nucleation field at the anti-nodes of the standing SAW. Domains tended to nucleate and propagate from anti-nodes to nodes of the standing SAW, resulting in striped domain patterns with spacing identical to the half-wavelength of the standing SAW. Chapter 5 delved into the impact of both heating and SAWs on DW motion in a Ta/Pt/Co/Ta thin film with PMA. A heating of approximately 10 K was observed within the SAW beam path when rf power was applied, as measured *in situ* using an on-chip Pt thermometer. DW velocity was assessed at various temperatures both with and without SAWs. The increase in DW velocity caused by travelling SAWs

was slightly more pronounced than that resulting from a 10-K temperature increase, suggesting that heating was the primary factor promoting DW motion. However, DW motion was substantially enhanced in the presence of standing SAWs due to the dominant effect of magnetoelastic coupling. This chapter emphasised the importance of considering heating in SAW devices, particularly with high rf power, and presented a straightforward method for measuring heating in SAW devices.

Chapter 6 studied the impact of SAW frequency on DW motion in thin films with varying levels of anisotropy disorder using micromagnetic simulations. The results showed that SAWs boosted DW velocity by facilitating the depinning of DWs from pinning sites through SAW-induced spin rotation. This not only increased the likelihood of DW depinning but also contributed to energy dissipation at the DW. In the thin film with 3% anisotropy disorder, DW velocity rose with increasing SAW frequency due to the amplified effect of spin rotation. In contrast, in the thin film with 1% anisotropy disorder, DW velocity decreased with rising SAW frequency because of pronounced SAW-induced spin rotation. This chapter shed light on the intricate relationship between SAWs, spin rotation, and DW dynamics, emphasising the important role of anisotropy disorder in determining the DW response to SAWs.

Chapter 7 illustrated the proof-of-concept of the motion of skyrmions in thin films with PMA driven by different modes of SAWs using micromagnetic simulations. Skyrmions were moved by both standing and travelling SAWs in longitudinal and transverse directions due to the introduced strain gradient. Standing SAWs formed pinning sites at their anti-nodes, while travelling SAWs provided a consistent force that moved skyrmions continuously. By integrating longitudinal travelling SAWs with transverse standing SAWs, the study showcased the precise transport of skyrmions longitudinally without transverse motion using orthogonal SAWs. This chapter pointed towards the potential of multi-channel skyrmion racetrack memory/logic devices driven by SAWs. In conclusion, these chapters have contributed to a deeper understanding of the

8 Conclusions and outlook

interactions between SAWs and magnetic thin films with PMA. This thesis not only offered valuable theoretical and experimental insights but also proposed potential energy-efficient methods for controlling magnetic spin structures. By elucidating the complex mechanisms through which SAWs impact magnetisation dynamics, this research has paved the way for future studies and technological advancements in the energy-efficient manipulation of magnetic structures using SAWs.

8.2 Outlook

The findings of this thesis illuminate the potential for utilising SAWs as an innovative tool for manipulating magnetic structures in an energy-efficient manner. However, the limited time frame of this research inevitably leaves some questions unanswered and challenges unaddressed. The following paths for future work and development could continue to build upon and extend the findings of this study:

Further exploration of magnetisation dynamics introduced by SAWs

The interactions between SAWs and magnetic spin structures, such as DWs and skyrmions, are very complicated and need additional theoretical and experimental investigation. For example, extending the work in Chapter 6 may involve the preparation and examination of thin films with varying levels of anisotropy disorder and the fabrications of IDTs with different geometrical configurations. These explorations could yield deeper insights into the effects of SAW frequencies on DW dynamics, thus enriching the understanding of magnetisation control mechanisms.

Addressing heating challenges

The heating effects caused by rf power dissipation can significantly influence the magnetic properties of thin films. Addressing these challenges necessitates a focus on

innovative device design that can mitigate or better manage the thermal impact.

Development of novel devices

The ability to precisely control skyrmion motion, as demonstrated in Chapter 7, opens exciting possibilities for the development of multi-channel skyrmion racetrack memory/logic devices utilising SAWs. As a continuation of the work presented, future research efforts could be directed towards the development of skyrmions with low depinning energy and experimental validation of skyrmion motion using SAWs. Such advancements could mark a significant step towards practical applications, bridging the gap between theoretical exploration and technological innovation.

8 Conclusions and outlook

REFERENCES

- [1] Igor Žutić, Jaroslav Fabian, and S Das Sarma. Spintronics: Fundamentals and applications. *Reviews of Modern Physics*, 76(2):323, 2004. [2](#)
- [2] Albert Fert. Nobel lecture: Origin, development, and future of spintronics. *Reviews of Modern Physics*, 80(4):1517, 2008.
- [3] Samuel D Bader and SSP Parkin. Spintronics. *Annual Review of Condensed Matter Physics*, 1(1):71–88, 2010. [2](#)
- [4] Stuart SP Parkin, Masamitsu Hayashi, and Luc Thomas. Magnetic domain-wall racetrack memory. *Science*, 320(5873):190–194, 2008. [2](#), [68](#)
- [5] Albert Fert, Nicolas Reyren, and Vincent Cros. Magnetic skyrmions: Advances in physics and potential applications. *Nature Reviews Materials*, 2(7):1–15, 2017. [2](#), [27](#), [34](#)
- [6] B Dieny and M Chshiev. Perpendicular magnetic anisotropy at transition metal/oxide interfaces and applications. *Reviews of Modern Physics*, 89(2):025008, 2017. [2](#), [68](#)
- [7] Wei-Gang Yang and Holger Schmidt. Acoustic control of magnetism toward energy-efficient applications. *Applied Physics Reviews*, 8(2):021304, 2021. [2](#), [8](#), [110](#)

REFERENCES

- [8] Laura Thevenard, J-Y Duquesne, Emmanuel Peronne, Hans Jürgen Von Bardeleben, H Jaffres, S Ruttala, Jean-Marie George, Aristide Lemaître, and Catherine Gourdon. Irreversible magnetization switching using surface acoustic waves. *Physical Review B*, 87(14):144402, 2013. [2](#), [10](#), [86](#), [110](#)
- [9] Laura Thevenard, Ibrahima Sock Camara, S Majrab, Mathieu Bernard, Pauline Rovillain, A Lemaître, Catherine Gourdon, and J-Y Duquesne. Precessional magnetization switching by a surface acoustic wave. *Physical Review B*, 93(13):134430, 2016. [10](#)
- [10] IS Camara, J-Y Duquesne, A Lemaître, C Gourdon, and L Thevenard. Field-free magnetization switching by an acoustic wave. *Physical Review Applied*, 11(1):014045, 2019. [2](#), [86](#), [110](#)
- [11] Jintao Shuai, Mannan Ali, Luis Lopez-Diaz, John E Cunningham, and Thomas A Moore. Local anisotropy control of Pt/Co/Ir thin film with perpendicular magnetic anisotropy by surface acoustic waves. *Applied Physics Letters*, 120(25):252402, 2022. [2](#), [69](#), [86](#), [110](#), [130](#)
- [12] Weiyang Li, Benjamin Buford, Albrecht Jander, and Pallavi Dhagat. Acoustically assisted magnetic recording: A new paradigm in magnetic data storage. *IEEE Transactions on Magnetics*, 50(3):37–40, 2014. [2](#), [8](#), [86](#), [110](#)
- [13] J Dean, MT Bryan, JD Cooper, A Virbule, JE Cunningham, and TJ Hayward. A sound idea: Manipulating domain walls in magnetic nanowires using surface acoustic waves. *Applied Physics Letters*, 107(14):142405, 2015. [2](#), [9](#), [10](#), [75](#), [110](#), [113](#)
- [14] Westin Edrington, Uday Singh, Maya Abo Dominguez, James Rehwaldt Alexander, Rabindra Nepal, and Shireen Adenwalla. SAW assisted domain wall

REFERENCES

- motion in Co/Pt multilayers. *Applied Physics Letters*, 112(5):052402, 2018. [9](#), [10](#), [86](#), [130](#)
- [15] Evgeny Vilkov, Oleg Byshevski-Konopko, Pavel Stremoukhov, Ansar Safin, Mikhail Logunov, Dmitry Kalyabin, Sergey Nikitov, and Andrei Kirilyuk. Magnetic domain wall motion driven by an acoustic wave. *Ultrasonics*, 119:106588, 2022. [10](#)
- [16] Yurui Wei, Xiaolei Li, Runliang Gao, Huiliang Wu, Xiangqian Wang, Zhaozhuo Zeng, Jianbo Wang, and Qingfang Liu. Surface acoustic wave assisted domain wall motion in [Co/Pd]₂/Pd(t)/Py multilayers. *Journal of Magnetism and Magnetic Materials*, 502:166546, 2020.
- [17] Y Cao, XN Bian, Z Yan, L Xi, N Lei, L Qiao, MS Si, JW Cao, DZ Yang, and DS Xue. Surface acoustic wave-assisted spin-orbit torque switching of the Pt/Co/Ta heterostructure. *Applied Physics Letters*, 119(1):012401, 2021. [10](#), [86](#), [130](#)
- [18] Jintao Shuai, Robbie G Hunt, Thomas A Moore, and John E Cunningham. Separation of heating and magnetoelastic coupling effects in surface-acoustic-wave-enhanced creep of magnetic domain walls. *Physical Review Applied*, 20(1):014002, 2023. [87](#), [110](#)
- [19] Rabindra Nepal, Utkan GÜngördü, and Alexey A Kovalev. Magnetic skyrmion bubble motion driven by surface acoustic waves. *Applied Physics Letters*, 112(11):112404, 2018. [2](#), [10](#), [75](#), [113](#), [131](#), [136](#)
- [20] Alex Hubert and Rudolf Schäfer. *Magnetic domains: The analysis of magnetic microstructures*. Springer Science & Business Media, 2008. [2](#), [29](#), [48](#)
- [21] Pascal Chauve, Thierry Giamarchi, and Pierre Le Doussal. Creep and depinning in disordered media. *Physical Review B*, 62(10):6241, 2000. [2](#), [116](#), [128](#)

REFERENCES

- [22] PJ Metaxas, JP Jamet, A Mougín, M Cormier, J Ferré, Vincent Baltz, B Rodmacq, B Dieny, and RL Stamps. Creep and flow regimes of magnetic domain-wall motion in ultrathin Pt/Co/Pt films with perpendicular anisotropy. *Physical Review Letters*, 99(21):217208, 2007. 3, 32, 128
- [23] Geoffrey SD Beach, Corneliu Nistor, Carl Knutson, Maxim Tsoi, and James L Erskine. Dynamics of field-driven domain-wall propagation in ferromagnetic nanowires. *Nature Materials*, 4(10):741–744, 2005. 3
- [24] Z Li and S Zhang. Domain-wall dynamics driven by adiabatic spin-transfer torques. *Physical Review B*, 70(2):024417, 2004. 3
- [25] Z Li and S Zhang. Domain-wall dynamics and spin-wave excitations with spin-transfer torques. *Physical Review Letters*, 92(20):207203, 2004. 3
- [26] Daniel C Ralph and Mark D Stiles. Spin transfer torques. *Journal of Magnetism and Magnetic Materials*, 320(7):1190–1216, 2008. 3
- [27] Durgesh Kumar, Tianli Jin, Rachid Sbiaa, Mathias Kläui, Subhankar Bedanta, Shunsuke Fukami, Dafine Ravelosona, See-Hun Yang, Xiaoxi Liu, and SN Piramanayagam. Domain wall memory: Physics, materials, and devices. *Physics Reports*, 958:1–35, 2022. 4
- [28] P Chureemart, RFL Evans, and RW Chantrell. Dynamics of domain wall driven by spin-transfer torque. *Physical Review B*, 83(18):184416, 2011.
- [29] A Thiaville, Y Nakatani, J Miltat, and N Vernier. Domain wall motion by spin-polarized current: A micromagnetic study. *Journal of Applied Physics*, 95(11):7049–7051, 2004. 4
- [30] Kwang-Su Ryu, Luc Thomas, See-Hun Yang, and Stuart Parkin. Chiral spin

REFERENCES

- torque at magnetic domain walls. *Nature Nanotechnology*, 8(7):527–533, 2013. [5](#), [68](#), [130](#)
- [31] Yucai Li, Kevin William Edmonds, Xionghua Liu, Houzhi Zheng, and Kaiyou Wang. Manipulation of magnetization by spin–orbit torque. *Advanced Quantum Technologies*, 2(1-2):1800052, 2019. [5](#)
- [32] Kevin Garello, Can Onur Avci, Ioan Mihai Miron, Manuel Baumgartner, Abhijit Ghosh, Stéphane Auffret, Olivier Boulle, Gilles Gaudin, and Pietro Gambardella. Ultrafast magnetization switching by spin–orbit torques. *Applied Physics Letters*, 105(21), 2014.
- [33] CK Safeer, Emilie Jué, Alexandre Lopez, Liliana Buda-Prejbeanu, Stéphane Auffret, Stefania Pizzini, Olivier Boulle, Ioan Mihai Miron, and Gilles Gaudin. Spin–orbit torque magnetization switching controlled by geometry. *Nature Nanotechnology*, 11(2):143–146, 2016. [5](#)
- [34] Neil Murray, Wei-Bang Liao, Ting-Chien Wang, Liang-Juan Chang, Li-Zai Tsai, Tsung-Yu Tsai, Shang-Fan Lee, and Chi-Feng Pai. Field-free spin–orbit torque switching through domain wall motion. *Physical Review B*, 100(10):104441, 2019. [5](#)
- [35] Takayuki Shiino, Se-Hyeok Oh, Paul M Haney, Seo-Won Lee, Gyungchoon Go, Byong-Guk Park, and Kyung-Jin Lee. Antiferromagnetic domain wall motion driven by spin–orbit torques. *Physical Review Letters*, 117(8):087203, 2016.
- [36] Debanjan Bhowmik, Mark E Nowakowski, Long You, OukJae Lee, David Keating, Mark Wong, Jeffrey Bokor, and Sayeef Salahuddin. Deterministic domain wall motion orthogonal to current flow due to spin orbit torque. *Scientific Reports*, 5(1):11823, 2015.

REFERENCES

- [37] Christopher EA Barker, Simone Finizio, Eloi Haltz, Sina Mayr, Philippa M Shepley, Thomas A Moore, Gavin Burnell, Jörg Raabe, and Christopher H Marrows. Domain wall motion at low current density in a synthetic antiferromagnet nanowire. *Journal of Physics D: Applied Physics*, 56(42):425002, 2023. 5
- [38] Jeongchun Ryu, Soogil Lee, Kyung-Jin Lee, and Byong-Guk Park. Current-induced spin-orbit torques for spintronic applications. *Advanced Materials*, 32(35):1907148, 2020. 5, 6
- [39] Kuntal Roy, Supriyo Bandyopadhyay, and Jayasimha Atulasimha. Hybrid spintronics and straintronics: A magnetic technology for ultra low energy computing and signal processing. *Applied Physics Letters*, 99(6), 2011. 5, 6
- [40] Ioan Mihai Miron, Thomas Moore, Helga Szabolcs, Liliana Daniela Buda-Prejbeanu, Stéphane Auffret, Bernard Rodmacq, Stefania Pizzini, Jan Vogel, Marlio Bonfim, Alain Schuhl, et al. Fast current-induced domain-wall motion controlled by the Rashba effect. *Nature Materials*, 10(6):419–423, 2011. 6, 68
- [41] A Yamaguchi, S Nasu, H Tanigawa, T Ono, K Miyake, Ko Mibu, and T Shinjo. Effect of joule heating in current-driven domain wall motion. *Applied Physics Letters*, 86(1):012511, 2005. 68
- [42] T A Moore, IM Miron, G Gaudin, G Serret, S Auffret, B Rodmacq, A Schuhl, Stefania Pizzini, Jan Vogel, and M Bonfim. High domain wall velocities induced by current in ultrathin Pt/Co/AIO_x wires with perpendicular magnetic anisotropy. *Applied Physics Letters*, 93(26), 2008. 6
- [43] Kuntal Roy, Supriyo Bandyopadhyay, and Jayasimha Atulasimha. Switching dynamics of a magnetostrictive single-domain nanomagnet subjected to stress. *Physical Review B*, 83(22):224412, 2011. 6

REFERENCES

- [44] You Ba, Shihao Zhuang, Yike Zhang, Yutong Wang, Yang Gao, Hengan Zhou, Mingfeng Chen, Weideng Sun, Quan Liu, Guozhi Chai, et al. Electric-field control of skyrmions in multiferroic heterostructure via magnetoelectric coupling. *Nature Communications*, 12(1):1–10, 2021. [6](#), [7](#), [8](#), [106](#), [130](#)
- [45] Philippa Mary Shepley. *Effect of piezoelectric strain on the magnetic properties of Pt/Co thin films*. PhD thesis, University of Leeds, 2015. [29](#), [45](#)
- [46] G. Masciocchi, M. Fattouhi, E. Spetzler, M.-A. Syskaki, R. Lehndorff, E. Martinez, J. McCord, L. Lopez-Diaz, A. Kehlberger, and M. Kläui. Generation of imprinted strain gradients for spintronics. *Applied Physics Letters*, 123(2):022404, 07 2023.
- [47] Mouad Fattouhi, Felipe Garcia-Sanchez, Rocio Yanes, Victor Raposo, Eduardo Martinez, and Luis Lopez-Diaz. Absence of Walker breakdown in the dynamics of chiral Néel domain walls driven by in-plane strain gradients. *Physical Review Applied*, 18(4):044023, 2022. [6](#)
- [48] Giovanni Masciocchi, Mouad Fattouhi, Andreas Kehlberger, Luis Lopez-Diaz, Maria-Andromachi Syskaki, and Mathias Kläui. Strain-controlled domain wall injection into nanowires for sensor applications. *Journal of Applied Physics*, 130(18), 2021. [6](#)
- [49] Giovanni Masciocchi, Johannes Wilhelmus van Der Jagt, M-A Syskaki, Alessio Lamperti, Niklas Wolff, Andriy Lotnyk, Jürgen Langer, Lorenz Kienle, Gerhard Jakob, Benjamin Borie, et al. Control of magnetoelastic coupling in Ni/Fe multilayers using He⁺ ion irradiation. *Applied Physics Letters*, 121(18), 2022. [6](#)
- [50] Robbie G Hunt, Kévin JA Franke, Philippa M Shepley, and Thomas A Moore.

REFERENCES

- Strain-coupled domains in BaTiO₃(111)-CoFeB heterostructures. *Physical Review B*, 107(1):014409, 2023. [7](#)
- [51] R. G. Hunt, K. J. A. Franke, P. S. Keatley, P. M. Shepley, M. Rogers, and T. A. Moore. Temperature dependence of magnetic anisotropy and domain wall tuning in BaTiO₃(111)/CoFeB multiferroics. *APL Materials*, 11(7):071112, 07 2023.
- [52] Ming Liu, Ogheneyunume Obi, Jing Lou, Yajie Chen, Zhuhua Cai, Stephen Stoute, Mary Espanol, Magnum Lew, Xiaodan Situ, Kate S Ziemer, et al. Giant electric field tuning of magnetic properties in multiferroic ferrite/ferroelectric heterostructures. *Advanced Functional Materials*, 19(11):1826–1831, 2009.
- [53] PM Shepley, AW Rushforth, M Wang, G Burnell, and TA Moore. Modification of perpendicular magnetic anisotropy and domain wall velocity in Pt/Co/Pt by voltage-induced strain. *Scientific Reports*, 5(1):1–5, 2015. [7](#), [75](#), [77](#), [106](#), [130](#)
- [54] E De Ranieri, PE Roy, D Fang, EK Vehstedt, AC Irvine, D Heiss, A Casiraghi, RP Campion, BL Gallagher, T Jungwirth, et al. Piezoelectric control of the mobility of a domain wall driven by adiabatic and non-adiabatic torques. *Nature Materials*, 12(9):808–814, 2013. [7](#)
- [55] Daniel B Gopman, Cindi L Dennis, PJ Chen, Yury L Lunin, Peter Finkel, Margo Staruch, and Robert D Shull. Strain-assisted magnetization reversal in Co/Ni multilayers with perpendicular magnetic anisotropy. *Scientific Reports*, 6(1):1–8, 2016. [7](#)
- [56] Chun Feng, Fei Meng, Yadong Wang, Jiawei Jiang, Nasir Mehmood, Yi Cao, Xiaowei Lv, Feng Yang, Lei Wang, Yongkang Zhao, et al. Field-free manipulation of skyrmion creation and annihilation by tunable strain engineering. *Advanced Functional Materials*, 31(14):2008715, 2021. [8](#), [106](#)

REFERENCES

- [57] Ronald M Hays and Clinton S Hartmann. Surface-acoustic-wave devices for communications. *Proceedings of the IEEE*, 64(5):652–671, 1976. 8
- [58] Trung Dung Luong and Nam Trung Nguyen. Surface acoustic wave driven microfluidics - A review. *Micro and Nanosystems*, 2(3):217–225, 2010. 8
- [59] Serge Ismael Zida, Yue-Der Lin, and Yit Lung Khung. Current trends on surface acoustic wave biosensors. *Advanced Materials Technologies*, 6(6):2001018, 2021. 8
- [60] Bo Liu, Xiao Chen, Hualin Cai, Mohammad Mohammad Ali, Xiangguang Tian, Luqi Tao, Yi Yang, and Tianling Ren. Surface acoustic wave devices for sensor applications. *Journal of Semiconductors*, 37(2):021001, 2016.
- [61] Adnan Mujahid and Franz L Dickert. Surface acoustic wave (SAW) for chemical sensing applications of recognition layers. *Sensors*, 17(12):2716, 2017. 8
- [62] Robert Weigel, David P Morgan, John M Owens, Arthur Ballato, Kenneth M Lakin, Ken-Ya Hashimoto, and Clemens CW Ruppel. Microwave acoustic materials, devices, and applications. *IEEE Transactions on Microwave Theory and Techniques*, 50(3):738–749, 2002. 8
- [63] S Davis, A Baruth, and Shireen Adenwalla. Magnetization dynamics triggered by surface acoustic waves. *Applied Physics Letters*, 97(23), 2010. 8
- [64] Weiyang Li, Benjamin Buford, Albrecht Jander, and Pallavi Dhagat. Writing magnetic patterns with surface acoustic waves. *Journal of Applied Physics*, 115(17), 2014. 8, 9, 68
- [65] Tomoyuki Yokouchi, Satoshi Sugimoto, Bivas Rana, Shinichiro Seki, Naoki Ogawa, Shinya Kasai, and Yoshichika Otani. Creation of magnetic skyrmions

REFERENCES

- by surface acoustic waves. *Nature Nanotechnology*, 15(5):361–366, 2020. [10](#), [74](#), [75](#), [111](#), [113](#), [133](#)
- [66] Ruyi Chen, Chong Chen, Lei Han, Peisen Liu, Rongxuan Su, Wenxuan Zhu, Yongjian Zhou, Feng Pan, and Cheng Song. Ordered creation and motion of skyrmions with surface acoustic wave. *Nature Communications*, 14(1):4427, 2023. [10](#)
- [67] Lukas Dreher, Mathias Weiler, Matthias Pernpeintner, Hans Huebl, Rudolf Gross, Martin S Brandt, and Sebastian TB Gönnerwein. Surface acoustic wave driven ferromagnetic resonance in nickel thin films: Theory and experiment. *Physical Review B*, 86(13):134415, 2012. [9](#)
- [68] Mathias Weiler, Lukas Dreher, Christian Heeg, Hans Huebl, Rudolf Gross, Martin S Brandt, and Sebastian TB Gönnerwein. Elastically driven ferromagnetic resonance in nickel thin films. *Physical Review Letters*, 106(11):117601, 2011. [9](#)
- [69] Laura Thevenard, Catherine Gourdon, Jean-Yves Prieur, Hans Jürgen Von Bardeleben, Serge Vincent, Loic Becerra, Ludovic Largeau, and J-Y Duquesne. Surface-acoustic-wave-driven ferromagnetic resonance in (Ga,Mn)(As,P) epilayers. *Physical Review B*, 90(9):094401, 2014. [10](#)
- [70] Laura Thevenard, Ibrahima Sock Camara, J-Y Prieur, Pauline Rovillain, Aristide Lemaître, Catherine Gourdon, and J-Y Duquesne. Strong reduction of the coercivity by a surface acoustic wave in an out-of-plane magnetized epilayer. *Physical Review B*, 93(14):140405, 2016. [10](#), [130](#)
- [71] Anil Adhikari and Shireen Adenwalla. Surface acoustic waves increase magnetic domain wall velocity. *AIP Advances*, 11(1):015234, 2021. [10](#), [86](#), [130](#)

REFERENCES

- [72] A Adhikari, ER Gilroy, TJ Hayward, and S Adenwalla. Surface acoustic wave assisted depinning of magnetic domain walls. *Journal of Physics: Condensed Matter*, 33(31):31LT01, 2021. [10](#)
- [73] Chao Chen, Dahai Wei, Liang Sun, and Na Lei. Suppression of skyrmion Hall effect via standing surface acoustic waves in hybrid ferroelectric/ferromagnetic heterostructures. *Journal of Applied Physics*, 133(20), 2023. [11](#)
- [74] Yu Miyazaki, Tomoyuki Yokouchi, and Yuki Shiomi. Trapping and manipulating skyrmions in two-dimensional films by surface acoustic waves. *Scientific Reports*, 13(1):1922, 2023. [11](#)
- [75] John MD Coey. *Magnetism and magnetic materials*. Cambridge University Press, 2010. [18](#), [24](#)
- [76] Stephen Blundell. *Magnetism in condensed matter*. OUP Oxford, 2001. [22](#)
- [77] MT Johnson, PJH Bloemen, FJA Den Broeder, and JJ De Vries. Magnetic anisotropy in metallic multilayers. *Reports on Progress in Physics*, 59(11):1409, 1996.
- [78] Sōshin Chikazumi. *Physics of ferromagnetism*. 94. Oxford University Press, 1997.
- [79] DS Ballantine Jr, Robert M White, Stephen J Martin, Antonio J Ricco, ET Zellers, GC Frye, and H Wohltjen. *Acoustic wave sensors: Theory, design and physico-chemical applications*. Elsevier, 1996. [37](#), [39](#), [60](#), [63](#)
- [80] Colin Campbell. *Surface acoustic wave devices and their signal processing applications*. Elsevier, 2012. [18](#), [35](#), [113](#)

REFERENCES

- [81] Norman L Schryer and Laurence R Walker. The motion of 180 domain walls in uniform dc magnetic fields. *Journal of Applied Physics*, 45(12):5406–5421, 1974. [31](#)
- [82] Vincent Jeudy, Alexandra Mougin, Sebastian Bustingorry, W Savero Torres, Jon Gorchon, Alejandro Benedykt Kolton, Aristide Lemaître, and J-P Jamet. Universal pinning energy barrier for driven domain walls in thin ferromagnetic films. *Physical Review Letters*, 117(5):057201, 2016. [32](#)
- [83] Jacques Ferré, Peter J Metaxas, Alexandra Mougin, Jean-Pierre Jamet, Jon Gorchon, and Vincent Jeudy. Universal magnetic domain wall dynamics in the presence of weak disorder. *Comptes Rendus Physique*, 14(8):651–666, 2013. [32](#)
- [84] Ezequiel E Ferrero, Sebastian Bustingorry, Alejandro B Kolton, and Alberto Rosso. Numerical approaches on driven elastic interfaces in random media. *Comptes Rendus Physique*, 14(8):641–650, 2013. [32](#)
- [85] C Burrowes, N Vernier, J-P Adam, L Herrera Diez, K Garcia, I Barisic, G Agnus, S Eimer, Joo-Von Kim, T Devolder, et al. Low depinning fields in Ta-CoFeB-MgO ultrathin films with perpendicular magnetic anisotropy. *Applied Physics Letters*, 103(18):182401, 2013. [32](#)
- [86] Alexandra Mougin, M Cormier, JP Adam, PJ Metaxas, and J Ferré. Domain wall mobility, stability and walker breakdown in magnetic nanowires. *Europhysics Letters*, 78(5):57007, 2007.
- [87] Michele Voto, Luis Lopez-Diaz, and Luis Torres. Effects of grain size and disorder on domain wall propagation in CoFeB thin films. *Journal of Physics D: Applied Physics*, 49(18):185001, 2016. [32](#), [33](#), [113](#), [115](#), [116](#), [122](#), [128](#)

REFERENCES

- [88] Touko Herranen and Lasse Laurson. Domain walls within domain walls in wide ferromagnetic strips. *Physical Review B*, 92(10):100405, 2015. [32](#)
- [89] Keisuke Yamada and Yoshinobu Nakatani. Excitation of magnetic domain wall velocity in (Co/Ni) nanowires induced by blocking the motion of vertical Bloch lines. *Applied Physics Express*, 8(9):093004, 2015. [32](#), [122](#)
- [90] Yoko Yoshimura, Kab-Jin Kim, Takuya Taniguchi, Takayuki Tono, Kohei Ueda, Ryo Hiramatsu, Takahiro Moriyama, Keisuke Yamada, Yoshinobu Nakatani, and Teruo Ono. Soliton-like magnetic domain wall motion induced by the interfacial Dzyaloshinskii–Moriya interaction. *Nature Physics*, 12(2):157–161, 2016. [32](#), [122](#), [123](#)
- [91] MR Lian and FB Humphrey. Observation of vertical Bloch line propagation. *Journal of Applied Physics*, 57(8):4065–4067, 1985. [32](#)
- [92] Touko Herranen and Lasse Laurson. Bloch-line dynamics within moving domain walls in 3D ferromagnets. *Physical Review B*, 96(14):144422, 2017. [32](#)
- [93] István Kézsmárki, Sándor Bordács, Peter Milde, Erik Neuber, Lukas M Eng, Jonathan Stuart White, Henrik M Rønnow, CD Dewhurst, M Mochizuki, K Yanai, et al. Néel-type skyrmion lattice with confined orientation in the polar magnetic semiconductor GaV_4S_8 . *Nature Materials*, 14(11):1116–1122, 2015. [33](#)
- [94] Olivier Boulle, Jan Vogel, Hongxin Yang, Stefania Pizzini, Dayane de Souza Chaves, Andrea Locatelli, Tefvik Onur Menteş, Alessandro Sala, Lili-ana D Buda-Prejbeanu, Olivier Klein, et al. Room-temperature chiral magnetic skyrmions in ultrathin magnetic nanostructures. *Nature Nanotechnology*, 11(5):449–454, 2016. [33](#)

REFERENCES

- [95] Sebastian Mühlbauer, Benedikt Binz, F Jonietz, Christian Pfleiderer, Achim Rosch, Anja Neubauer, Robert Georgii, and Peter Böni. Skyrmion lattice in a chiral magnet. *Science*, 323(5916):915–919, 2009. [33](#)
- [96] XZ Yu, Yoshinori Onose, Naoya Kanazawa, Joung Hwan Park, JH Han, Yoshio Matsui, Naoto Nagaosa, and Yoshinori Tokura. Real-space observation of a two-dimensional skyrmion crystal. *Nature*, 465(7300):901–904, 2010. [33](#)
- [97] Giovanni Finocchio, Felix Büttner, Riccardo Tomasello, Mario Carpentieri, and Mathias Kläui. Magnetic skyrmions: From fundamental to applications. *Journal of Physics D: Applied Physics*, 49(42):423001, 2016. [34](#)
- [98] Michaela Kuepferling, Arianna Casiraghi, Gabriel Soares, Gianfranco Durin, Felipe Garcia-Sanchez, Liu Chen, Christian H Back, Christopher H Marrows, Silvia Tacchi, and Giovanni Carlotti. Measuring interfacial Dzyaloshinskii–Moriya interaction in ultrathin magnetic films. *Reviews of Modern Physics*, 95(1):015003, 2023. [34](#)
- [99] Ajaya K Nayak, Vivek Kumar, Tianping Ma, Peter Werner, Eckhard Pippel, Roshnee Sahoo, Françoise Damay, Ulrich K Röbber, Claudia Felser, and Stuart SP Parkin. Magnetic antiskyrmions above room temperature in tetragonal heusler materials. *Nature*, 548(7669):561–566, 2017. [34](#)
- [100] Naoto Nagaosa and Yoshinori Tokura. Topological properties and dynamics of magnetic skyrmions. *Nature Nanotechnology*, 8(12):899–911, 2013. [34](#), [130](#)
- [101] Richard O’Rorke. *The spatial control of particles in microfluidic systems using surface acoustic waves*. PhD thesis, University of Leeds, 2010. [35](#), [43](#)
- [102] Wikimedia Commons. File:perovskite.svg – Wikimedia Commons, the free media repository, 2022. [Online; accessed 19-July-2023]. [35](#)

REFERENCES

- [103] J Paskauskas, R Rimeika, and D Ciplys. Velocity and attenuation of surface acoustic waves in proton-exchanged 128 degrees-rotated Y-cut LiNbO₃. *Journal of Physics D: Applied Physics*, 28(7):1419, 1995. [43](#), [71](#), [75](#), [113](#)
- [104] S Swann. Magnetron sputtering. *Physics in Technology*, 19(2):67, 1988. [44](#)
- [105] Wuge H Briscoe, Meng Chen, Iain E Dunlop, Jacob Klein, Jeffrey Penfold, and Robert MJ Jacobs. Applying grazing incidence X-ray reflectometry (XRR) to characterising nanofilms on mica. *Journal of Colloid and Interface Science*, 306(2):459–463, 2007. [47](#)
- [106] Lyman G Parratt. Surface studies of solids by total reflection of X-rays. *Physical Review*, 95(2):359, 1954. [47](#)
- [107] Matts Björck and Gabriella Andersson. GenX: An extensible X-ray reflectivity refinement program utilizing differential evolution. *Journal of Applied Crystallography*, 40(6):1174–1178, 2007. [48](#)
- [108] IV Soldatov and Rudolf Schäfer. Selective sensitivity in Kerr microscopy. *Review of Scientific Instruments*, 88(7):073701, 2017. [48](#), [50](#)
- [109] Klayout. Available at: <https://www.klayout.org>. [54](#)
- [110] Almas Bashir, Tahir Iqbal Awan, Aqsa Tehseen, Muhammad Bilal Tahir, and Mohsin Ijaz. Interfaces and surfaces. *Chemistry of Nanomaterials*, pages 51–87, 2020. [57](#), [58](#)
- [111] Spartak Gevorgian, LJ Peter Linner, and Erik L Kollberg. Cad models for shielded multilayered CPW. *IEEE Transactions on Microwave Theory and Techniques*, 43(4):772–779, 1995. [59](#)

REFERENCES

- [112] Arne Vansteenkiste, Jonathan Leliaert, Mykola Dvornik, Mathias Helsen, Felipe Garcia-Sanchez, and Bartel Van Waeyenberge. The design and verification of Mumax3. *AIP Advances*, 4(10):107133, 2014. [61](#), [74](#), [81](#), [111](#), [133](#)
- [113] Frederic Vanderveken, Jeroen Mulkers, Jonathan Leliaert, Bartel Van Waeyenberg, Bart Sorée, Odysseas Zografos, Florin Ciubotaru, and Christoph Adelman. Finite difference magnetoelastic simulator. *Open Research Europe*, 1, 2021. [63](#)
- [114] Stephen J Martin, Gregory C Frye, and Stephen D Senturia. Dynamics and response of polymer-coated surface acoustic wave devices: Effect of viscoelastic properties and film resonance. *Analytical Chemistry*, 66(14):2201–2219, 1994. [63](#)
- [115] Soon-Wook Jung, Woojin Kim, Taek-Dong Lee, Kyung-Jin Lee, and Hyun-Woo Lee. Current-induced domain wall motion in a nanowire with perpendicular magnetic anisotropy. *Applied Physics Letters*, 92(20):202508, 2008. [68](#)
- [116] Satoru Emori, Uwe Bauer, Sung-Min Ahn, Eduardo Martinez, and Geoffrey SD Beach. Current-driven dynamics of chiral ferromagnetic domain walls. *Nature Materials*, 12(7):611–616, 2013. [68](#)
- [117] Th Gutjahr-Löser, D Sander, and J Kirschner. Magnetoelastic coupling in Co thin films on W(001). *Journal of Magnetism and Magnetic Materials*, 220(1):1–7, 2000. [74](#), [133](#)
- [118] Tomohiro Nozaki, Makoto Konoto, Takayuki Nozaki, Hitoshi Kubota, Akio Fukushima, and Shinji Yuasa. Control of the magnetic domain of Pt/Co/Ru/MgO multilayer: Effect of Co thickness and Ru insertion. *AIP Advances*, 10(3):035130, 2020. [75](#)

REFERENCES

- [119] Tengfei Zheng, Chaohui Wang, Qiao Hu, and Shoupeng Wei. The role of electric field in microfluidic heating induced by standing surface acoustic waves. *Applied Physics Letters*, 112(23):233702, 2018. [86](#), [96](#)
- [120] Pawel Utko, Poul Erik Lindelof, and Kurt Gloos. Heating in single-electron pumps driven by surface acoustic waves. *Applied Physics Letters*, 88(20):202113, 2006. [86](#)
- [121] Junlong Han, Fan Yang, Hong Hu, Qingyun Huang, Yulin Lei, and MingYu Li. Thermal control design and packaging for surface acoustic wave devices in acoustofluidics. *IEEE Transactions on Ultrasonics, Ferroelectrics, and Frequency Control*, 69(1):386–398, 2021. [96](#), [105](#)
- [122] Richie J Shilton, Virgilio Mattoli, Marco Travaglati, Matteo Agostini, Andrea Desii, Fabio Beltram, and Marco Cecchini. Rapid and controllable digital microfluidic heating by surface acoustic waves. *Advanced Functional Materials*, 25(37):5895–5901, 2015. [86](#)
- [123] Byung Hang Ha, Kang Soo Lee, Ghulam Destgeer, Jinsoo Park, Jin Seung Choung, Jin Ho Jung, Jennifer Hyunjong Shin, and Hyung Jin Sung. Acoustothermal heating of polydimethylsiloxane microfluidic system. *Scientific Reports*, 5(1):1–8, 2015.
- [124] Jun Kondoh, Norifumi Shimizu, Yoshikazu Matsui, Mitsunori Sugimoto, and Showko Shiokawa. Development of temperature-control system for liquid droplet using surface acoustic wave devices. *Sensors and Actuators A: Physical*, 149(2):292–297, 2009.
- [125] Pradipta Kr Das, Arthur D Snider, and Venkat R Bhethanabotla. Acoustothermal heating in surface acoustic wave driven microchannel flow. *Physics of Fluids*, 31(10):106106, 2019.

REFERENCES

- [126] Jinsoo Park, Byung Hang Ha, Ghulam Destgeer, Jin Ho Jung, and Hyung Jin Sung. An acoustothermal heater for paper microfluidics towards point-of-care glucose detection. *Physics Procedia*, 70:46–49, 2015.
- [127] Ketav Kulkarni, James Friend, Leslie Yeo, and Patrick Perlmutter. Surface acoustic waves as an energy source for drop scale synthetic chemistry. *Lab on a Chip*, 9(6):754–755, 2009.
- [128] Yong Wang, Qian Zhang, Ran Tao, Dongyang Chen, Jin Xie, Hamdi Torun, Linzi E Dodd, Jingting Luo, Chen Fu, Jethro Vernon, et al. A rapid and controllable acoustothermal microheater using thin film surface acoustic waves. *Sensors and Actuators A: Physical*, 318:112508, 2021. [86](#)
- [129] Robert Weser, Zhichao Deng, Vijay V Kondalkar, Alexandre N Darinskii, Christian Cierpka, Hagen Schmidt, and Jörg König. Three-dimensional heating and patterning dynamics of particles in microscale acoustic tweezers. *Lab on a Chip*, 22(15):2886–2901, 2022. [86](#)
- [130] A Winkler, S Harazim, DJ Collins, R Brünig, H Schmidt, and SB Menzel. Compact SAW aerosol generator. *Biomedical Microdevices*, 19(1):1–10, 2017. [99](#), [105](#)
- [131] Dhritiman Bhattacharya, Seyed Armin Razavi, Hao Wu, Bingqian Dai, Kang L Wang, and Jayasimha Atulasimha. Creation and annihilation of non-volatile fixed magnetic skyrmions using voltage control of magnetic anisotropy. *Nature Electronics*, 3(9):539–545, 2020. [106](#), [130](#)
- [132] Jintao Shuai, Luis Lopez-Diaz, John E Cunningham, and Thomas A Moore. Surface acoustic wave effect on magnetic domain wall dynamics. *Physical Review B*, 108(10):104420, 2023. [110](#)

REFERENCES

- [133] Jonathan Leliaert, Ben Van de Wiele, Arne Vansteenkiste, Lasse Laurson, Gianfranco Durin, Luc Dupré, and Bartel Van Waeyenberge. Current-driven domain wall mobility in polycrystalline permalloy nanowires: A numerical study. *Journal of Applied Physics*, 115(23):233903, 2014. [113](#), [128](#)
- [134] Jonathan Leliaert, Ben Van de Wiele, Arne Vansteenkiste, Lasse Laurson, Gianfranco Durin, Luc Dupré, and Bartel Van Waeyenberge. Influence of material defects on current-driven vortex domain wall mobility. *Physical Review B*, 89(6):064419, 2014. [113](#)
- [135] Piotr Kuszewski, Ibrahima S Camara, Nicolas Biarrotte, Loic Becerra, Jürgen von Bardeleben, W Savero Torres, A Lemaître, Catherine Gourdon, JY Duquesne, and Laura Thevenard. Resonant magneto-acoustic switching: Influence of Rayleigh wave frequency and wavevector. *Journal of Physics: Condensed Matter*, 30(24):244003, 2018. [113](#)
- [136] Joo-Von Kim and Myoung-Woo Yoo. Current-driven skyrmion dynamics in disordered films. *Applied Physics Letters*, 110(13):132404, 2017. [113](#)
- [137] Yoshinobu Nakatani, André Thiaville, and Jacques Miltat. Faster magnetic walls in rough wires. *Nature Materials*, 2(8):521–523, 2003. [115](#)
- [138] E Martinez, L Lopez-Diaz, L Torres, C Tristan, and O Alejos. Thermal effects in domain wall motion: Micromagnetic simulations and analytical model. *Physical Review B*, 75(17):174409, 2007. [115](#), [123](#), [125](#)
- [139] Jonathan Leliaert, Ben Van de Wiele, Jasper Vandermeulen, Annelies Coene, Arne Vansteenkiste, Lasse Laurson, Gianfranco Durin, Bartel Van Waeyenberge, and Luc Dupré. Thermal effects on transverse domain wall dynamics in magnetic nanowires. *Applied Physics Letters*, 106(20):202401, 2015. [123](#), [128](#)

REFERENCES

- [140] Jisu Ryu, Sug-Bong Choe, and Hyun-Woo Lee. Magnetic domain-wall motion in a nanowire: Depinning and creep. *Physical Review B*, 84:075469, Aug 2011. [128](#)
- [141] Albert Fert, Vincent Cros, and Joao Sampaio. Skyrmions on the track. *Nature Nanotechnology*, 8(3):152–156, 2013. [130](#)
- [142] Jacob Torrejon, Junyeon Kim, Jaivardhan Sinha, Seiji Mitani, Masamitsu Hayashi, Michihiko Yamanouchi, and Hideo Ohno. Interface control of the magnetic chirality in CoFeB/MgO heterostructures with heavy-metal underlayers. *Nature Communications*, 5(1):1–8, 2014. [130](#)
- [143] Kai Litzius, Jonathan Leliaert, Pedram Bassirian, Davi Rodrigues, Sascha Kromin, Ivan Lemesh, Jakub Zazvorka, Kyu-Joon Lee, Jeroen Mulkers, Nico Kerber, et al. The role of temperature and drive current in skyrmion dynamics. *Nature Electronics*, 3(1):30–36, 2020.
- [144] Seonghoon Woo, Kai Litzius, Benjamin Krüger, Mi-Young Im, Lucas Caretta, Kornel Richter, Maxwell Mann, Andrea Krone, Robert M Reeve, Markus Weigand, et al. Observation of room-temperature magnetic skyrmions and their current-driven dynamics in ultrathin metallic ferromagnets. *Nature Materials*, 15(5):501–506, 2016.
- [145] Lucas Caretta, Maxwell Mann, Felix Büttner, Kohei Ueda, Bastian Pfau, Christian M Günther, Piet Helsing, Alexandra Churikova, Christopher Klose, Michael Schneider, et al. Fast current-driven domain walls and small skyrmions in a compensated ferrimagnet. *Nature Nanotechnology*, 13(12):1154–1160, 2018.
- [146] Seonghoon Woo, Kyung Mee Song, Xichao Zhang, Yan Zhou, Motohiko Ezawa, Xiaoxi Liu, S Finizio, J Raabe, Nyun Jong Lee, Sang-Il Kim, et al. Current-

REFERENCES

- driven dynamics and inhibition of the skyrmion Hall effect of ferrimagnetic skyrmions in GdFeCo films. *Nature Communications*, 9(1):1–8, 2018. [130](#)
- [147] Roméo Juge, Soong-Geun Je, Dayane de Souza Chaves, Liliana D Buda-Prejbeanu, José Peña-Garcia, Jayshankar Nath, Ioan Mihai Miron, Kumari Gaurav Rana, Lucia Aballe, Michael Foerster, et al. Current-driven skyrmion dynamics and drive-dependent skyrmion Hall effect in an ultrathin film. *Physical Review Applied*, 12(4):044007, 2019. [130](#)
- [148] Igor Dzyaloshinsky. A thermodynamic theory of weak ferromagnetism of antiferromagnetics. *Journal of Physics and Chemistry of Solids*, 4(4):241–255, 1958. [130](#)
- [149] Tôru Moriya. Anisotropic superexchange interaction and weak ferromagnetism. *Physical Review*, 120(1):91, 1960.
- [150] Christopher EA Barker, Eloi Haltz, Thomas Moore, Christopher H Marrows, et al. Breathing modes of skyrmion strings in a synthetic antiferromagnet multilayer. *Journal of Applied Physics*, 133(11), 2023. [130](#), [133](#)
- [151] Fumihiko Matsukura, Yoshinori Tokura, and Hideo Ohno. Control of magnetism by electric fields. *Nature Nanotechnology*, 10(3):209–220, 2015. [130](#)
- [152] Greta Radaelli, Daniela Petti, E Plekhanov, I Fina, P Torelli, BR Salles, Matteo Cantoni, Christian Rinaldi, D Gutiérrez, G Panaccione, et al. Electric control of magnetism at the Fe/BaTiO₃ interface. *Nature Communications*, 5(1):1–9, 2014.
- [153] Yasuhiro Shirahata, Ryota Shiina, Diego López González, Kévin JA Franke, Eiji Wada, Mitsuru Itoh, Nikolay A Pertsev, Sebastiaan van Dijken, and Tomoyasu Taniyama. Electric-field switching of perpendicularly magnetized multilayers. *NPG Asia Materials*, 7(7):e198–e198, 2015. [130](#)

REFERENCES

- [154] Yadong Wang, Lei Wang, Jing Xia, Zhengxun Lai, Guo Tian, Xichao Zhang, Zhipeng Hou, Xingsen Gao, Wenbo Mi, Chun Feng, et al. Electric-field-driven non-volatile multi-state switching of individual skyrmions in a multiferroic heterostructure. *Nature Communications*, 11(1):1–8, 2020. [130](#)
- [155] Jintao Shuai, Luis Lopez-Diaz, John E Cunningham, and Thomas A Moore. Precise transport of skyrmions by surface acoustic waves. *arXiv preprint arXiv:2305.16006*, 2023. [130](#)
- [156] Lukas Exl, Simon Bance, Franz Reichel, Thomas Schrefl, Hans Peter Stimming, and Norbert J. Mauser. LaBonte’s method revisited: An effective steepest descent method for micromagnetic energy minimization. *Journal of Applied Physics*, 115(17):17D118, 2014. [133](#)
- [157] Jeroen Mulkers, Bartel Van Waeyenberge, and Milorad V. Milošević. Effects of spatially-engineered Dzyaloshinskii–Moriya interaction in ferromagnetic films. *Physical Review B*, 95(14):144401, 2017. [133](#)
- [158] João Sampaio, Vincent Cros, Stanislas Rohart, André Thiaville, and Albert Fert. Nucleation, stability and current-induced motion of isolated magnetic skyrmions in nanostructures. *Nature Nanotechnology*, 8(11):839–844, 2013. [133](#)
- [159] N Fujita, N Inaba, F Kirino, S Igarashi, K Koike, and H Kato. Damping constant of Co/Pt multilayer thin-film media. *Journal of magnetism and magnetic materials*, 320(22):3019–3022, 2008. [133](#)
- [160] Anjan Barman, Suqin Wang, Olav Hellwig, Andreas Berger, Eric E Fullerton, and Holger Schmidt. Ultrafast magnetization dynamics in high perpendicular anisotropy [Co/Pt]_n multilayers. *Journal of applied physics*, 101(9), 2007. [133](#)

